1-1-2013

Acoustic Emission Source Characterization of Fatigue Crack Extension in Steel Bridge Material

MD MOZAHID HOSSAIN
University of South Carolina - Columbia

Recommended Citation

HOSSAIN, M. M.(2013). *Acoustic Emission Source Characterization of Fatigue Crack Extension in Steel Bridge Material.* (Doctoral dissertation). Retrieved from https://scholarcommons.sc.edu/etd/2433

ACOUSTIC EMISSION SOURCE CHARACTERIZATION OF FATIGUE CRACK EXTENSION IN STEEL BRIDGE MATERIAL

By

Mozahid Hossain

Bachelor of Science
Bangladesh University of Engineering and Technology, 2007

Master of Science
North Dakota State University, 2010

Submitted in Partial Fulfillment of the Requirements

For the Degree of Doctor of Philosophy in

Civil Engineering

College of Engineering and Computing

University of South Carolina

2013

Accepted by:

Paul H. Ziehl, Major Professor

Juan M. Caicedo, Committee Member

Fabio Matta, Committee Member

Lingyu (Lucy) Yu, Committee Member

Lacy Ford, Vice Provost and Dean of Graduate Studies

DEDICATION

To my parents for their love and encouragement throughout my life

ACKNOWLEDGMENTS

I wish to express my gratitude and appreciation to my advisor, Professor Paul Ziehl, for his guidance, friendship and support throughout this research. His optimistic way of thinking was always a source of motivation for me. It has been an honor working under his supervision. I also thank my wife, Saima Satter, for the support and happiness she provided. I would like to thank my committee members, Professors Juan Caicedo, Fabio Matta, and Lucy Yu, for their valuable advice and comments on the work in this dissertation. Special thanks to Jahangir Alam and Mujadid Mirza for all encouragement and friendship received during this period. I would like to mention my friends who helped me with my work and made my life in Columbia enjoyable. To Dr. Adrian Pollock for technical help, sharing experiences and enjoyable conversation. To my sister and brother for their encouragement and wonderful help, especially during the last moments. And to my parents for their endless love and support throughout my studies in the US. Without them, I would not have made it this far.

ABSTRACT

The probability of Acoustic Emission (AE) detection associated with fatigue crack extension in steel bridge components is a difficult problem due to the complexity of the AE sources. AE is a very promising technique for structural health monitoring and automated micro-crack detection as it is generated by the material itself, unlike other nondestructive testing techniques (for example impact echo and ultrasonics), which require external input sources. Characterizing the source of AE is an ongoing challenge because AE sensors are not only sensitive to the AE signals but also to mechanical noise and reflections. It is therefore difficult to interpret the actual AE signals related to microcrack extension. Assessing the probability of detection is also influenced by the medium of wave propagation, threshold settings, sensitivity and frequency range of the sensors, and source–to–sensor distance. This dissertation addresses AE detection associated with fatigue crack extension in steel bridge elements and the associated probability of detection as a function of the stress intensity range. AE events associated with fatigue crack extension are assessed using moment tensor and b-value analysis. AE events are also synchronized with the strain field at the crack tip through the use of Digital Imaging Correlation (DIC). For simplicity, the Poisson and Weibull distributions are employed to calculate the probability of AE detection associated with fatigue crack extension at different levels of fatigue crack growth.

PREFACE

This dissertation is submitted for the degree of Doctor of Philosophy at the University of South Carolina, Columbia, South Carolina, United States of America. The research described herein was conducted under the supervision of Professor Paul H. Ziehl in the Department of Civil and Environmental Engineering, University of South Carolina, between August 2010 and April 2013.

This work is to the best of my knowledge original, except where acknowledgements and references are made to previous work. Neither this, nor any substantially similar dissertation has been or is being submitted for any other degree, diploma or other qualification at any other university. Portions of this work may be presented in journal articles and conference proceedings.

TABLE OF CONTENTS

LIST OF TABLES

LIST OF FIGURES

LIST OF ABBREVIATIONS

AE	Acoustic Emission
ASNT	American Society of Non-destructive Testing
NDT	Non-Destructive Testing
POD	Probability of Detection
ASTM	American Society for Testing and Materials
FHWA	Federal Highway Administration
SCDOT	South Carolina Department of Transportation

CHAPTER 1

INTRODUCTION

Acoustic emission (AE) is a term that is used to describe stress waves produced by the sudden internal stress redistribution of materials caused by the changes in the internal structure (ASNT 2005, Scruby 1987). Possible causes of these changes are crack initiation and growth, crack opening and closure, dislocation movement, twinning, and phase transformation in monolithic materials such as steel (ASNT 2005). Each damage mechanism is associated with varying types and levels of deformation that release energy in the form of stress waves whenever a dynamic micro-structural change occurs (Scruby 1987). Micro-damage events generate AE signals according to the characteristics of the source (ASNT 2005, Scruby 1987, Pollock 1981). Most acoustic emission is damage-related; thus, the detection and monitoring emissions is often used to predict material failure. The difference between the AE technique and other nondestructive evaluation (NDE) methods is that AE detects activity caused by distress within the material as it occurs, while other NDE methods attempt to interrogate the nature of flaws or the internal structure of the materials themselves. Furthermore, AE is very easily implemented as it only requires the attachment of small sensors to the surface of the structure and the AE system used to continuously monitor the progression of damage due to loading or other external sources.

1.1 Need for Nondestructive Evaluation / Structural health monitoring

Highway bridges are key components of a healthy and productive transportation infrastructure. According to Parmar and Sharp (2009), there is an increasing demand for ensuring the integrity and performance of our nation's bridges. A variety of factors may lead to their degradation. Cracks and flaws in steel bridge components may have originated during the fabrication process and grown due to fatigue, corrosion, or both. The main cause of deterioration of highway bridge components is a complex combination of factors that include both load and environment. Such factors damage bridges through processes such as crack initiation and growth and plastic/elastic deformations. Bridges require timely inspection and evaluation of structural health. Unpredictability of degradation introduces a degree of uncertainty in the decision making process regarding the frequency of inspection and planning for repair and replacement of the affected structural parts. Since there is a physical limitation on access to various components, any visit for inspection becomes expensive even if the task is to inspect only a single structural element. The consequences of a bridge failure due to uncertainty in predicting degradation could be disastrous to the motorist and deleterious to the nation's economy.

In recent years, there have been several highly publicized incidents that involved the catastrophic failure of transportation systems. The first of these involved the interstate highway bridge I-35W over the Mississippi River in Minneapolis, Minnesota, which collapsed at 6:05 p.m. on August 1, 2007 (wikipedia.com) (Figure 1.1). The I-35W bridge was designed and constructed before metal fatigue cracking in bridges was a well-understood phenomenon. However, it is noted that this failure was not attributed to fatigue damage.

In the late 1970s, when a better understanding of metal fatigue cracking was

Figure 1.1. Interstate highway bridge I-35W, Minneapolis, Minnesota, collapsed at 6:05 p.m. on August 1, 2007(wikipedia.com).

established within the industry, steel bridges such as the I-35W bridge were recognized as being “non-load-path-redundant”—that is, if certain main truss members (termed “fracture-critical”) failed, the bridge would collapse. According to the Federal Highway Administration (FHWA) 2007 data, 19,273 are considered “non-load-path-redundant” among 600,000 bridges in the National Bridge Inventory. About 465 bridges within the inventory have a main span that is a steel deck truss. SCDOT has for a number of years been aware of potential fatigue cracking in the State's bridges (Figure 1.2). As with other State DOT's, SCDOT is particularly aware of potential issues with non-load-path-redundant bridges, where the failure of a tension member could lead to a catastrophic failure. Because of a general lack of understanding in the 1950s and 1960s of the effects of cyclical loading on steel bridges, many bridges built during that period had poor fatigue-resistant details. Since about 1975, Mn/DOT has conducted fatigue studies on seven State bridges, including the I-35W bridge, where inspections found evidence of fatigue cracking. The Lafayette bridge, built in 1968, carries U.S. Highway 52 over the Mississippi River in St. Paul, Minnesota. In 1975, inspectors found a crack in a primary girder that developed in a lateral gusset plate web gap and extended through the bottom flange and about 75 percent of the height of the web. In 2006, TKDA Consultants, Inc., of St. Paul, conducted a vulnerability assessment of the bridge with regard to fatigue cracking. The bridge is scheduled to be replaced in 2010. The Dresbach Bridge, built in 1967, carries Interstate 90 over the Mississippi River in the southeastern part of the State. The bridge is a fracture-critical two-girder system with floor beams and stringers. A 1975 inspection found two vertical fatigue cracks in the structure, one of which was 18 inches long. Additional cracks were found in 1987, 1993, 1996, and 1998. These two incidents are clear examples of the need for monitoring of structures with an emphasis on fatigue crack growth.

Figure 1.2. Fatigue crack at steel girder in Rock Hill, SC at Intersection I-77/SC901.

There are many more examples of the need for crack monitoring. A primary goal of non-destructive evaluation (NDE) is to locate and monitor defect growth so that preventive actions can be taken before the defects reach a critical size and failure occurs. Toward this end, many non-destructive test (NDT) methods have been employed, including x-ray, radiography, ultrasonic, magnetic resonance, dye penetrant and eddy current. A common trait of these techniques is that the energy to be used to detect the defects is propagated into the structure, and this energy must then interact with the defect. If the orientation or the size of the defect is such that the energy fails to interact with or be modulated by the defect, the defect will remain undetected. Additionally, the methods listed above are, at best, difficult to apply to a structure while it is in service. Therefore, flaw growth while the structure is under load is difficult to monitor. Acoustic emission has the ability to detect and locate flaw growth while the structure is in service.

Due to applied stress a, a defect begins to grow and releases energy in the form of a stress wave or stress pulse. To detect this stress wave a transducer is attached to the structure and the output from the transducer is captured. AE sensors are very sensitive to the a wide variety of sources, some of which are not associated with the defect of interest. It is essential to know the characteristics of the acoustic emission associated with the actual crack growth. This signal can then be used to determine the nature of the event and prognosis models employed to predict remaining service life.

1.2 RESEARCH SIGNIFICANCE

Assessing the probability of AE detection during fatigue crack growth in steel bridge components remains a difficult problem due to the complexity of AE sources. The probability of AE detection is related not only to AE generation during fatigue crack growth but also to several other factors including wave propagation characteristics of the material, frequency range of the sensors, the source–to–sensor distance.

Detecting AE associated with fatigue crack growth is critical in the development of AE as a primary structural health monitoring method. When a crack is subjected to cyclic loading, the crack tip travels a very short distance in each loading cycle, in the range of 1×10^{-4} mm/cycle (4×10^{-6} in./cycle) to 1×10^{-3} mm/cycle (4×10^{-5} in./cycle) (Hamstad and McColskey 1999, ASNT 2005). When a small crack extends, stress free surfaces are created and stress fields in the crack trip abruptly redistribute. Typically, at the lower crack growth rate, several thousand cycles are required to obtain one valid acoustic emission signal (ASNT 2005). At the higher crack growth rate, approximately one or two cycles are required for a valid event from A514 steel (Hamstad and McColskey 1999). Other steels require 18 to 130 cycles for a valid event.

Plastic deformation is the primary source of acoustic emission in metallic materials (ASNT 2005); however, these are rarely energetic events (Scruby 1987). When plastic deformation at the crack tip is prohibited, the crack can travel through grains by splitting atom bonds in lattice planes. This is called intra- or trans-granular cleavage. When the crack propagates along grain boundaries, it is referred to as inter-granular cleavage (ASNT 2005). Cleavage or similar highly emissive mechanisms produce very energetic acoustic emissions events (Scruby 1987, Pollock 2009, ASNT 2005) that are readily detected with commercial sensors.

The overall objective of the research program reported in this dissertation is to characterize the source of AE signals in steel bridge material. A secondary objective is to assess the probability of AE detection associated with fatigue crack extension. Mechanisms investigated include plastic deformation, inclusion debonding, crack extension, and cleavage fracture.

1.3 RESEARCH METHODOLOGY

This research is focused on assessing the probability of detection associated with fatigue crack extension in ASTM A572 Grade 50 structural steel with acoustic emission. Compact tension (CT) specimens were utilized. This type of specimen is representative of a single edge crack steel bridges. With this specimen geometry, relatively low load is sufficient for a high stress intensity (K) value For AE source characterization, waveform and moment tensor analysis requires the use of wideband sensors (WDI-AST). Six WDI-AST and two R15I-AST sensors were placed near the crack tip to record AE and thereby minimize attenuation effects.

Source characterization, signal discrimination, and noise reduction are challenging yet vital for successful AE applications. This research study is focused on source mechanisms and the associated acoustic emission signatures when the sensor are placed near the crack tip. Further study is recommended to investigate the effects of attenuation. The probability of detection associated with fatigue crack extension is evaluated as a function of stress intensity range (ΔK) as this is a function of all the variables for fatigue crack growth such as load, crack length, and geometry.

This dissertation includes eight chapters in addition to appendices that present the supplementary data and calculations. Chapters 4, 5 and 6 are organized as stand-alone papers. Hence, conclusions may be sometimes repeated at the end of these chapters.

A literature review of AE for structural health monitoring and fatigue crack growth are provided in Chapter 2. The material and instruments used for the study are described in Chapter 3.Chapter 4 describes the monitoring of AE during fatigue loading. The results obtained by SEM scanning are discussed in regard to confirmation of the failure mechanisms during fatigue crack growth. In Chapter 5, digital image correlation is described and utilized for the development of AE correlation plots during the fatigue loading. The probability of detection associated with the fatigue crack extension in steel bridge component through the use of AE data is the subject of Chapter 6. AE events are synchronized with the strain field at a head of the crack tip monitored through Digital Imaging Correlation (DIC) and thus the real AE events associated with the fatigue crack extension are screened and POD is calculated. A summary of findings, comments on practical implications, and recommendations and suggestions for future research are presented in Chapter 7.

CHAPTER 2

LITERATURE REVIEW

This chapter is divided into three parts: a) general background information on acoustic emission and nondestructive inspection of steel structures; b) theory of b-value analysis and source identification in steel; and c) general discussion on AE parameters.

2.1 BACKGROUND INFORMATION ON ACOUSTIC EMISSION

Acoustic emission is the generation and propagation of stress waves in materials due to deformation, initiation and growth of a crack, opening and closing of a crack, diffusion and movement of a dislocation, and twining (ASNT 2005). The sources of AE are predominantly damage-related; therefore careful AE monitoring can lead an investigator to the prediction of material failure. Over the past decades, various acoustic emission monitoring devices have been developed for nondestructive testing and evaluation of structures including the transportation infrastructure.

There are many non-destructive evaluation methods which can locate a crack, but not all such methods are capable of characterizing growing/active cracks that are most likely to result in structure failure. A scientifically sound, technically feasible, reasonably predictable and economically attractive bridge management program should be developed for efficient functioning of the bridge. Acoustic emission (AE) has the potential to eliminate much of the subjectivity of traditional methods of visual inspection and bridge condition determination. AE monitoring is capable of performing the critical tasks of detection, location and characterization of the flaws that are likely to cause serious impairment of the bridge structure and its ability to perform as designed. A key advantage of the AE method over other NDT approaches is its ability to respond only to active flaws making it a principal candidate for flaw characterization and real time health monitoring of highway bridges.

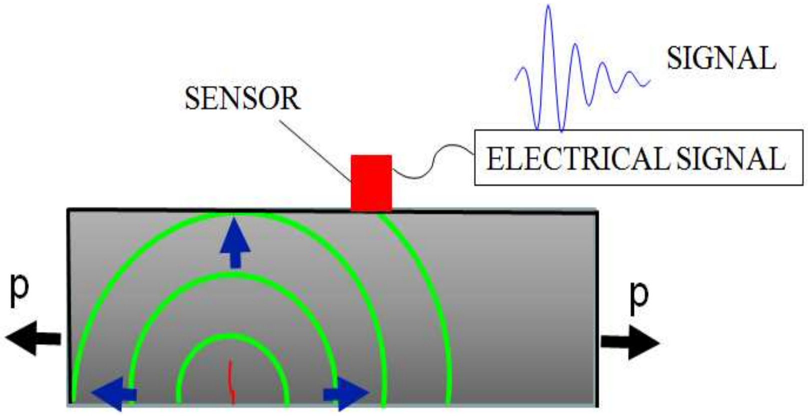

Figure 2.1. Schematic of acoustic emission process.

According to Parmar and Sharp (2009), Pollock and Smith (1971) were the first to apply AE monitoring for bridges, wherein they collected data during proof testing of a portable tank bridge for the British Ministry of Defense. They demonstrated that signals recorded in the field could be associated with test results on laboratory specimens. In 1972, Argonne National Laboratory proposed to monitor emissions from a bridge on I-80 in Illinois and Hopwood (1973) monitored emissions from the eye-bar members of a bridge. Although good transmission through eye-bar members of the bridge was observed the signal to noise ratio remained a serious difficulty. An extensive program funded by the Federal Highway Administration (FHWA) with Battelle Pacific Northwest in the late 1970s resulted in the development of a battery powered digital acoustic emission monitor

(Hutton and Skorpik 1975, 1978) that allowed periodic data recording and storage on erasable programmable read only memory chips for further processing and evaluation. This study was among the first to demonstrate the potential of AE frequency spectrum analysis for centralized signal processing. The noise to signal ratio, however, remained a concern during these studies.

The Kentucky Transportation Research Center, from 1980–1982, used a digital AE monitor to periodically monitor a bridge on I- 471 and reported effects of traffic and rainfall as sources of emission noise (Miller 1987). Dunegan Corporation, under contract from the West Virginia Department of Highways, examined the practical difficulties related to long term AE monitoring of bridges (Hartman 1983). The financial benefits of AE monitoring over the use of periodic ultrasonic, magnetic particle, or liquid penetrant inspections of known defects were discussed. United Technologies Research Center, under contract from FHWA, performed laboratory and field tests to characterize AE signals from flaws and various noise related sources (Miller et al. 1983). Both time and frequency domain representations of signals were investigated. Waveforms and source classification for filtering of noise and for discriminating between different damage related events, such as brittle fracture and fatigue, were demonstrated.

Prine and Hopwood (1985) considered an acoustic emission for service evaluations of bridge components. They pointed out that emission signals from bridges contained information on traffic volume and vehicle speed and weight, as well as on structural details and transducer characteristics.

In 1987, the University of Maryland monitored the Woodrow Wilson Bridge on the border of Maryland and Virginia for the Maryland Department of Transportation. They found that the predominant peak frequency of noise emissions is distinctly lower than crack related emissions. Suitable software filters, designed to exclude signals whose time domain parameters do not fall within the range of parameters of crack related emissions, can eliminate most noise signals (Vannoy et al. 1987). These studies were followed by laboratory tests on full size A588 bridge beams (Vannoy and Azmi 1991). AE parameters of cracks versus noise on rolled, welded, and cover plated beams were characterized in both the time and frequency domains. It was determined during these studies that corrosion has no effect on the time domain parameters of crack related emissions. A related study at the University of Maryland (Hariri, 1990) sought to develop a database of signal characteristics from different bridge steels and various material and loading conditions, as well as from different part geometries and thicknesses for bridge related applications.

FHWA has conducted a series of field tests on several bridges. Results of these tests have emphasized the need for source location and guard sensors for filtering irrelevant acoustic emission events (Carlyle 1993, Carlyle and Ely 1992, Carlyle and Leaird 1992). The effectiveness of AE was demonstrated for finding new cracks.

The Canadian National Railways sponsored AE monitoring of 36 railroad bridges over a period of three years (Gong et al. 1992). Using a known functional relationship between the emission count rate and the stress intensity factor range, this study was able to classify cracks into five levels of severity. Spatial discrimination and filtering using parameter windows determined from laboratory tests on bridge steels were used to minimize noise.

The effectiveness of combining AE and strain gage monitoring was demonstrated on three bridges in Wisconsin and California (Prine 1993). In a departure from the usual crack characterization function of AE monitoring, a bascule bridge was tested to determine the cause of loud impact noises that accompanied the lifting and lowering of the bridge. McBride et al. (1993) used continuous AE monitoring for enhanced fatigue crack detection. AE has also been used in detecting the onset of crack growth in rail steels (Bassim et al., 1994). Such data has been used in attempts to design theoretical models for fatigue damage mechanisms (Fang et al. 1995).

The work performed to date has provided a reasonable scientific base upon which to build an engineering application of AE as part of a steel bridge health monitoring and assessment technique. Nearly all of the work has sought to use AE to detect the initiation of damage, locate it, monitor its growth, and characterize the severity of damage.

In the work described above, little or no attempt has been made to understand the true source of the acoustic emission data in steel bridge materials. This information is critical for the development of models for the prognostics of steel bridges, which differs significantly in scope and difficulty from the more commonly addressed problem of real-time characterization of crack 'severity'. The purpose of this study is to enhance the understanding of the actual source mechanism of AE ***associated with the fatigue crack extension.*** A related goal is to assess the probability of detection ***of fatigue crack extension*** based on AE data. This work is limited to source characterization in ASTM

572 G50 steel which is widely used in the steel bridge construction industry. From an engineering point of view, this restriction is quite significant. The data storage, processing, and complexity of the AE system may be greatly reduced if the source mechanisms can be understood. Noise sources associated with the structure may be minimized, since the properties of the AE events associated with the fatigue crack extension will be known. This information will support decision making of the bridge owner, make it feasible to configure a system for constant surveillance, and also provide early warning of impending failure for critical bridge components.

2.2 NON-DESTRUCTIVE TESTING

Every structure or component in the real world contains imperfections. The imperfections in a structure may or may not be visible or harmful. Accordingly, nondestructive testing (NDT), or nondestructive inspection (NDI), or nondestructive evaluation (NDE) can be performed to ensure that structures can be safely operated for a certain period of time. In general, the role of NDT is to detect, locate, and evaluate the significance of flaws for in-service structures. NDT also plays a role of quality control in the manufacturing process. It is used to ensure that imperfections in every part of a structure are below an accepted tolerance prior to installation.

Benefits of NDT include life extension and cost savings. Preventive maintenance associated with inspections will reduce the cost of major repairs, such as repairing cracks. NDT for quality control provides more confidence in the design process, thus leading to a reduced factor of safety and construction cost.

NDT can be categorized into two groups: active and passive. Active NDT methods send energy into or onto the specimen. Flawed and unflawed specimens respond differently to this energy, which will be observed by a trained inspector. Examples of this method are ultrasonics, impact echo, radiography, and eddy current. The passive method observes acoustic or visual changes in a specimen under either a normal load condition or a proof cycle. A defect in the structure will reveal itself naturally. Passive methods include acoustic emission, visual inspection, dye-penetrant, and leak detection (Bray and Stanley1997).

The most common nondestructive testing methods are summarized below. Each method has strengths and weaknesses and they are complementary to each another.

Radiography:

Radiography (ASNT 2005) utilizes the penetration of X or gamma radiation to the specimens. The X-ray is radiated from a radioactive isotope, and is received by film on the other side of the specimen. The film will show the density of the radiation by the color of the gray tone. A crack or imperfection usually reduces the thickness of the material. This causes a higher density of radiation, and a darker mark on the film.

Magnetic Particle:

The magnetic particle method (ASNT 2005) induces a magnetic field in a ferro-magnetic specimen and dusts the surface with iron particles. If surface discontinuities are present, a distortion of iron particle arrangement will be seen due to the disturbance of the magnetic field.

Ultrasonics:

Ultrasonic testing (ASNT 2005) is performed by transmitting high frequency sound waves into a material. The waves can be detected by a receiver on the opposite side of the specimen or hit the back wall of the specimen and reflect back to a receiver on the same side as the transmitter. An imperfection within the thickness can also interrupt or reflect the signal. The time of flight is used to calculate the thickness of the part, or the depth of the imperfection.

Liquid Penetrant:

In this test (ASNT 2005), the specimen is coated by a visible or fluorescent dye solution. If there are surface cracks, the dye will penetrate and leave the marks on the surface. Fluorescent dyes give better sensitivity than the normal dye, but an ultraviolet lamp must be used.

Eddy Current:

The eddy current method (ASNT 2005) uses electrical current generated in a conductive material by inducing a magnetic field. The electrical current (eddy current) will be continuously monitored during the test. Imperfections on or near the surface of a specimen will cause a change in the magnetic field, thus changing the level of eddy current.

Leak Testing:

Leaking of a liquid from a tank or pressure vessel can be inspected by several methods. Examples include listening devices, pressure gauge measurements, liquid and gas penetrant techniques, and soap bubble testing (ASNT 2005).

Visual Examination:

Visual examination (ASNT 2005) is the oldest and the most widely used method of NDT. It can detect most of the serious defects on or near the surface of a structure. Visual examination may require tools to enhance the performance. These tools include a flashlight, knife, hand held magnifying glass, and hardness impressor.

Acoustic Emission:

Acoustic emission is defined as transient elastic waves within a material caused by the release of localized stress energy (ASTM E 1316). Hence, an event source is the phenomenon that releases energy into the material, which then propagates as an elastic wave. Acoustic emission can be detected in frequency ranges under 1 kHz, and have been reported at frequencies up to 100 MHz (ASNT 2005).

AE is related to an irreversible release of energy, and can be generated from sources not involving material failure including friction, cavitation, and impact (ASNT 2005). Events can also come quite rapidly when materials begin to fail, in which case AE activity rates are often studied as opposed to individual events (Scruby 1987). AE events that have been studied in this research among material failure processes include fatigue crack extension in steel bridge elements.

2.3 ACOUSTIC EMISSION FILTERING TECHNIQUES AND SOURCE LOCATION

In addition to internal acoustic emission sources, external noise (background noise) such as mechanical rubbing, wind, air hoses, and moving trucks can create elastic waves, which interfere with the genuine data. These background noises have to be prevented or filtered out before the AE data is analyzed.

The advantage of AE is that it is a global method rather than a local method meaning that the technique monitors a large area of the structure, rather than a small local area. As a result, the monitoring can be done within a short period of time and, is not labor intensive. However, the disadvantage of this technology is that the acoustic emission is dependent on the applied load. This means, some discontinuities may not generate detectable AE under a certain types or level of load.

Specific areas of AE research are discussed below:

Source Location: The ability to locate the position of discontinuities in a structure. This is beneficial particularly for large structures as it is time consuming to locate the area to be repaired.

Source Identification: The ability to determine the type of discontinuities within a structure. This is also referred to as “failure mechanism typing” or ‘signature analysis’. In most cases, AE from different failure modes exhibits a different waveform.

Probability of Detection (POD):

Several statistical forms including the Poisson distribution, Weibull distribution and Gumbel distribution might be applied for POD calculation (Pollock 2009). For simplicity Poisson distribution and Weibull distribution may be used for POD calculation in my study.

Weibull distribution:

The probability density function of a Weibull random variable is (Papoulis et al., 2001)

$$f(x;\lambda,k)=\begin{cases}\dfrac{k}{\lambda}\left(\dfrac{x}{\lambda}\right)e^{-(x/\lambda)^k} & x\geq 0\\ 0 & x<0\end{cases} \tag{2.1}$$

where $k > 0$ is the *shape parameter* and $\lambda > 0$ is the *scale parameter* of the distribution. If the quantity x is a "detectable AE events", the Weibull distribution gives a distribution for which the high emissive failure (brittle fracture) is proportional to a power of time. A value of $k > 1$ indicates that the failure rate increases with time. This happens if there is an "aging" process, or parts that are more likely to fail as time go on. The cumulative distribution function for the Weibull distribution is

$$F(x;k,\lambda)=\begin{cases}1-e^{-(x/\lambda)^k} & x\geq 0\\ 0 & x<0\end{cases} \tag{2.2}$$

Poisson distribution:

The amplitude distribution generated in the fatigue test leads directly to the expected number of events exceeding the detection threshold. Statistics can be used to determine the probability that at least one signal will exceed the threshold so that the produced acoustic emission will be detected. For simplicity, the Poisson distribution may be used to determine the expected number of AE events crossing the threshold x, the probability of getting none above the threshold is e^{-x}. Consequently, the probability of getting at least one above threshold is $(1 - e^{-x})$.

2.4 Amplitude Distribution

The amplitude is the most fundamental parameter for acoustic emission since the threshold amplitude is the parameter that the data acquisition system uses to decide whether or not an emission will be recorded (Pollock 1978, Hill 1995, Valentin 1985, Hill et al. 1996, and Hill et al. 1998). Amplitude distribution is a histogram of the number of hits (plotted on a log scale) at different amplitude levels. Figure 2.2 is an example of this plot. Amplitude distribution is sometimes called a “differential amplitude distribution”.

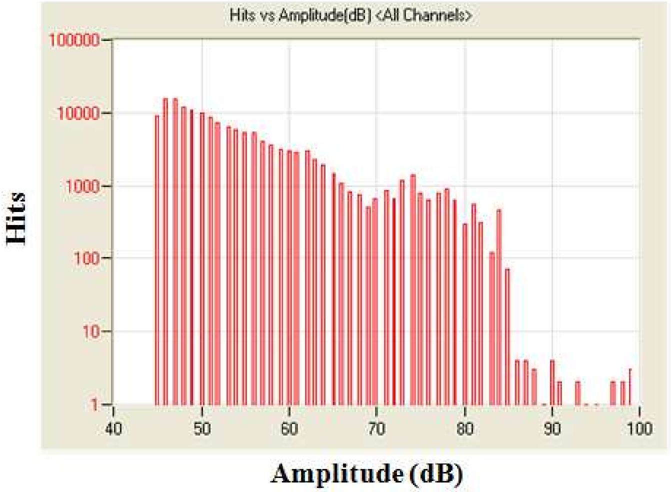

Figure 2.2. Cumulative amplitude distribution.

Several researchers have studied source identification by looking at humps in this plot. It was found that different humps represent different failure mechanism (Pollock 1978, Hill 1995, Valentin 1985).

2.5 CUMULATIVE AMPLITUDE DISTRIBUTION

It is known that the attenuation in a material decreases the amplitude of emission as the wave travels (Elmore and Heald 1969). Therefore, a sensor closer to the source will detect higher amplitude of an event than sensors further away. This means that away from the source, the amplitude parameter itself cannot be referred to as a certain type of failure mechanism. As a result, cumulative amplitude distribution and b-value have been developed and applied to AE source identification (Pollock 1981). Cumulative amplitude distribution was first developed for seismology applications, and was later adopted for AE technology. Cumulative amplitude distribution is a log plot of the histogram of the number of hits at specified amplitude or higher. The slope of the plot is referred to as the b-value and will be discussed in the next section.

2.6 THEORY OF B-VALUE

The AE data acquisition system normally records the amplitude in voltage (V) or decibel (dB) units. The relationship between these units is:

$$A = 20\log\left(\frac{V}{V_{ref}}\right) \tag{2.3}$$

where

$V_{ref} = 1\mu V$,

A = amplitude in decibels

V = amplitude in voltage units

For a given amplitude distribution function [$f(V)$], the number of hits for which the amplitude is equal to the value V. $F(V)$ is a cumulative amplitude distribution plot of the number of hits for which the amplitudes are equal to or higher than the value V. Then the two functions are related by the equation:

$$f(V) = -\frac{dF(V)}{dV} \tag{2.4}$$

$\Phi(V)$ is a normalized function representing the probability that an amplitude exceeds V, and V_0 is the smallest detected amplitude (typically threshold), which gives $\Phi(V_0) = 1$. The problem arises in developing a function $\Phi(V)$ that describes the nature of detectable failure. Pollock (1981), suggested use of the function:

$$\Phi(V) = \left(\frac{V}{V_0}\right)^{-b} \tag{2.5}$$

where;

b = parameter characteristic of the distribution function

$F(V)$ and $\Phi(V)$ are related by the equation:

$$F(V) = N_0 \Phi(V) \tag{2.6}$$

where

N_0 = total number of hits

therefore;

$$F(V) = N_0 \left(\frac{V}{V_0} \right)^{-b} \tag{2.7}$$

The advantage of this function is that if plotted on a log-log scale, the function will be seen as a straight line with the slope of "- b". This can be called a "power law".

$$\log \left(\frac{F(V)}{N_0} \right) = -b \log \left(\frac{V}{V_0} \right) \tag{2.8}$$

Now, if the amplitude in a decibel unit is replaced, the equation will be:

$$B = -b \frac{\log(10)}{20} \tag{2.9}$$

It is showed by Pollock (1981) that this b or B value is unique for each failure mechanism, and the log scale will remove the effect of wave attenuation. Therefore, the b or B value will not change with the distance between source to sensor, if all signals are attenuated equally (Pollock 1981).

2.7 AVERAGE AMPLITUDE BASED B-VALUE

In addition to the introduction of cumulative amplitude distributions and b-values described earlier, Pollock (1981) suggested "average amplitudes", which are described by the equation:

$$\overline{A} = A_0 + \frac{20}{b \ln 10} \tag{2.10}$$

where

$\overline{A}$ = average amplitude

A_0 = threshold amplitude

Pollock stated that the plot of the graph log $\overline{A}$ vs. time was a very promising way to analyze AE data. The advantages of this method are that it is easy to compute, can be performed in real time, and is easy to understand.

The b value can change during a test, which can be explained as the transition from one mechanism to another. Pollock (1981) stated that most of the b-value range is between 0.7-1.5, but it could be as low as 0.4 or as high as 4.0. The lower values are usually associated with discontinuous crack growth in high-strength brittle metals, whereas the high values can be from plastic zone growth prior to crack extension. In 1983, researchers conducted research on AE signatures from different defects (Scarpellini et al. 1983). The cumulative amplitude distribution showed a bi-linear slope, with b = 2 at lower amplitude and b =1 at higher amplitude. They suggested that there were two failure mechanisms in inclusion specimens.

2.8 COMMON PARAMETERS USED IN AE

To help visualize the AE data, an idealized waveform of a typical AE hit is shown in Figure 2.3. For convenience, a listing of AE Parameters is provided below:

Threshold (Voltage Threshold): “A voltage level on an electronic comparator such that signals with amplitudes larger than this level will be recognized. The voltage threshold may be user adjustable, fixed, or automatic floating” (ASTM E 1316). The threshold is set for eliminating electronic background noise, which normally has low amplitude.

Counts (AE counts): “The number of times the acoustic emission signal exceeds a preset threshold during any selected portion of a test” (ASTM E 1316).

Arrival time: Absolute time when a burst signal first crosses the detection threshold (ASTM E 1316).

Peak amplitude**:** “The peak voltage of the largest excursion attained by the signal waveform from an emission event” (ASTM E 1316). In other words, peak amplitude is the highest point of the signal. It is the absolute value on either positive or negative side of a waveform. The peak amplitude is usually reported in decibels (dB) due to the wide range of typical values in voltage unit. Voltage is converted to decibels using the following equation:

$$A = 20 \log\left(\frac{V}{V_{ref}}\right) \qquad (2.11)$$

where

A = Amplitude in decibels

V = Voltage of peak excursion

V_{ref} = Reference voltage, typically 1μV (Voltage generated by 1 mbar pressure of the face of sensor).

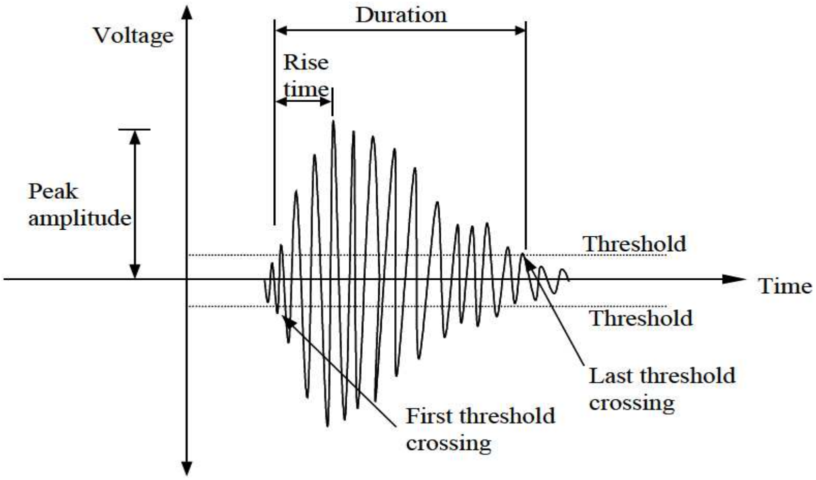

Figure 2.3. Schematic of acoustic emission parameters (Ativitavas 2002)

Duration (Hit Duration): “The time between AE signal start and AE signal end” (ASTM E 1316). It is the time from the first to the last threshold crossing and is typically displayed in microseconds.

Hit (Sensor Hit): **“**The detection and measurement of an AE signal on a channel” (ASTM E 1316).

Frequency: The number of cycles per second of the pressure variation in a wave (ASTM E 1316). Commonly, an AE wave consists of several frequency components.

Event (AE Event): “A local material change giving rise to acoustic emission” (ASTM E 1316).

Source (AE Source): “The position of one or more AE events” (CARP, 1999)

CHAPTER 3

MATERIALS AND INSTRUMENTATIONS

This chapter addresses the material specification of the compact tension specimen utilized for the AE monitoring fatigue test. In addition, AE equipment, including AE data acquisition systems and sensors, are described. This chapter also describes the testing facilities utilized in this research.

3.1 Compact Tension (CT) Specimen

Compact tension (CT) specimen is utilized for AE monitoring fatigue test made of ASTM A572 G50 steel widely used for steel bridge materials in steel construction industry.

Benefit of utilized CT specimen:

- It is small and does not require much material.
- Relatively low load is sufficient for a high k-value which can be very useful if the load capacity of MTS machine is limited.
- It is the representative of single edge crack in in-service steel bridges.

Disadvantages of CT specimen:

- Production of a CT specimen is not simple.

- CT specimen crack is also opened by a significant bending moment on the specimen. Cracks in real structures usually do not show a similar type of loading.

3.2 AE INSTRUMENTATIONS

Two AE data acquisition systems were used for this research. Physical Acoustic Corporation (PAC), Princeton, New Jersey, manufactured both of them. Details are given below:

The drawback of this system is that it has a 16 bit architecture, which can record any information only up to the maximum value of 65,535 or ($2^{16}-1$). This directly affects the recording performance of AE duration, which can be longer than 100,000 microseconds in some tests.

Eighteen channel MISTRAS system. The state-of-the-art MISTRAS system can acquire digital waveforms (Figure 3.1). The MISTRAS has adjustable settings (threshold, hit definition time, etc.) and is capable of very high data acquisition rates. Also, it has a very short rearm time. The MISTRAS includes an extensive suite of software programs that can be run on any Windows based computer.

The MISTRAS hardware parameters and a signal-processing filter were set as described below:

1. Test threshold = 45 dB; for 40 if the background noise is minimized.
2. Signal processing filter = 100-400 kHz
3. Peak definition time = 200 microseconds

4. Hit definition time = 400 microseconds

5. Hit lockout time = 40 microseconds

Figure 3.1. MISTRAS System.

Table 3.1. Hardware Set-up

Quantity	**Values**
Peak Definition Time (PDT)	200 µs
Hit Definition Time (HDT)	800 µs
Hit Lockout Time (HLT)	1000 µs
Maximum duration	1000 µs
Threshold	40 dB
Gain	23 dB
Sensor Preamplifier Gain (R15I)	40 dB
Sensor Preamplifier Gain (WDI)	40 dB
Sensor Band pass Filter (R15I)	80-200 kHz
Sensor Band pass Filter (WDI)	200-900 kHz
Event Timing	First Threshold Crossing (FTC)

3.3 AE SENSORS

The term transducer (piezoelectric transducer) is most often used for acoustic emission sensor as it converts time dependent displacement into an electrical signal. The active element of a piezoelectric transducer is a thin disk of piezoelectric material metalized on both faces for electrical contact, and mounted in a metal cylinder to provide electromagnetic interference shielding.

The piezoelectric ceramics commonly used in AE transducers are made of small crystals of titanates and zirconates which are mixed with other materials (most widely used commercial piezoelectric material is various phases of lead zirconate titanate PZT, i.e. PZT-4, PZT-5, PZT-5A, PZT-5H), molded to the desired shape, and fired in a kiln. The ceramic material is then made piezoelectric by poling, which is the process of heating the material above its Curie temperature while the material is in a strong electric field (PCA 2002). The first piezoelectric ceramics in general use was barium titanate, and that was followed during the 1960's by lead zirconate titanate compositions, which are now the most commonly employed ceramic for making transducers. New materials such as piezo-polymers and composites are also being used in some applications.

The thickness of the active element (PZT) is determined by the desired frequency of the transducer. A thin wafer element vibrates with a wavelength that is twice its thickness. Therefore, piezoelectric crystals are cut to a thickness that is half the desired radiated wavelength. The higher the frequency of the transducer, the thinner the active element. The primary reason that high frequency contact transducers are not produced is because the element is very thin and too fragile.

The R15I-AST and WDI-AST integral preamplifier sensors represent a significant advancement for the field of acoustic emission by enclosing a low-noise FET input 40 dB pre-amplifier inside a standard high sensitivity sensor (Table 3.2). These rugged, small size AE integral pre-amplifier/sensors eliminate the need for cumbersome pre-amplifiers by incorporating two functions into one, thereby reducing equipment costs and decreasing set-up time for field applications. R15I is general purpose sensor provides a good mix of high sensitivity and high low frequency rejection. These properties make it very useful for monitoring common structures such as pipelines, vessels, bridges, and storage tanks in petroleum, refineries, chemical plants, offshore platforms, as well as factory and process monitoring applications.

Wideband (WDI-AST) sensors are typically used in research applications and other applications where a high fidelity AE response is required. In research applications, wideband AE sensors are useful where frequency analysis of the AE signal is required and to help determine the predominant frequency band of AE sources for noise discrimination and selection of a suitable lower cost, general purpose AE sensor. In high fidelity applications, wideband sensors can detect various AE wave modes to provide more information about the AE source and distance of the AE event.

Table 3.2. Model Related Specifications (PCA 2002)

Specification	Sensor Model				
	R6I	R15I	R30I	R50I	WDI
Sensor drive capability (w/RG-58 AU cable)	≤ 3000 ft. (1000 m)	≤ 1000 ft. (300 m)	≤ 500 ft. (160 m)	≤ 300 ft. (100 m)	≤300 ft. (100 m)
Pre-amplification	40 dB	40 dB	40 dB	40 dB	40 dB
Peak sensitivity Ref V/m/s)/[Ref V/mbar]	120† [-26]*	109† [-24.5]* 109[-22]	98† [-24]*	86† [-28]*	87† [-28]* 96 [-25]
Operating frequency range (kHz)	40–100	70–200 80-200	125–450	300–550	100–1000 200-900
Resonant frequency (kHz)[1]	50† [90]*	125† [153]* 75[150]	225† [350]*	320† [500]*	125† [500]*

† Denotes response to plane waves (angle of incidence normal to face of sensor).

* Denotes response to surface waves (angle of incidence transverse or parallel to face of sensor).

The R15I-AST and WDI-AST sensors are shown in Figure 3.2.

Figure 3.2. AE sensors and 0.3 mm lead pencil.

3.4 USAGE OF COUPLANT

A couplant applied between surface of test object and sensitive face of an AE-sensor reduces the transmission losses of elastic wave energy entering the AE-sensor, effectively increasing the sensitivity of the sensor. A couplant should be selected under consideration of the environment (e.g. temperature, pressure, composition of atmosphere or liquid environment). Most important a couplant should be chemically compatible to the test object’s surface (e.g. not corroding). A couplant should be applied with the thinnest practical layer. No voids or entrapped air inclusions should be present. Thick layers of couplant or unevenness of it can reduce the sensitivity of an AE-sensor.

3.5 PREAMPLIFIER

The piezoelectric material in the AE sensor transforms the signal to a voltage. Since the magnitude of the voltage is very small, a preamplifier is required to amplify the voltage to a more suitable range. Usually, the preamplifier is mounted integral in R15I-AST and WDI-AST sensors.

3.6 AE DATA ACQUISITION

After the preamplifier, the AE signal is transmitted to the AE data acquisition system by a cable. The data acquisition system can filter (eliminate unwanted signals or frequencies), or amplify the signals. It will also record, and organize the AE data. Most of the time data acquisition software can instantly plot graphs and analyze the data, which is helpful for inspectors to understand what is happening during the test.

3.7 TESTING FACILITY

Most of the experiments were conducted in the Structural Engineering Laboratory at the University of South Carolina, Columbia Campus. The testing machines used in the program is-

Universal Testing Machine 810: The machine was manufactured by Satec Systems, Inc. (Figure 3.3). It has hydraulic wedge grip mechanism with 600 kips maximum capacity for tension loading.

Figure 3.3. MTS 810 machine.

CHAPTER 4

SOURCE CHARACTERIZATION OF ACOUSTIC EMISSION DURING FATIGUE CRACK PROPAGATION IN STEEL BRIDGE MATERIAL

The acoustic emission (AE) technique is widely used for structural health monitoring and assessment. Prognosis and assessment of fatigue crack growth in steel bridges depend on proper collection and interpretation of the AE signals. AE sensors are not only sensitive to cracks but also mechanical noise generated from grating. Therefore, extraction of the AE data associated with fatigue crack extension is key to successful implementation for structural health monitoring. Previous research has shown that plastic deformation at the crack tip is the primary source of acoustic emission in ductile materials such as steel, while other studies have reported that non-metallic inclusions in steel are the main source of acoustic emission. There is no clear consensus about the source mechanism of AE during fatigue crack growth in steel. The work described here is focused on characterization of AE sources based on b-value analysis and subsequent fractographic observations through scanning electronic microscope (SEM). Fractographic and b-value analysis show that both ductile and brittle failure mechanisms are present in fatigue crack propagation. Brittle mechanisms produce highly energetic AE events and ductile mechanisms produce relatively less energetic AE events.

4.1 INTRODUCTION

Acoustic emission (AE) is defined as the elastic waves produced by the sudden redistribution of the stress field near the crack tip by localized damage in the material (ASNT 2005). Plastic deformation, crack initiation, and crack extension are possible causes of this damage (ASNT 2005, Hossain et al. 2012, Hossain et al. 2013). Damaging phenomena can be broadly classified as ductile or brittle fracture mechanisms. Extensive experimental studies (Lin et al. 1987, McMahon and Cohen 1965, Thompson and Knott 1993, ASNT 2005, Garrison and Moody 1987, Hossain et al. 2012, Hossain et al. 2013, Ohira and Pao 1986, Ruggieri 2004) of macro and micro-fracture mechanisms have resulted in an understanding of two distinct failure processes. The first is broadly referred to as ductile and is characterized by relatively high energy, a high level of macro-plasticity, and a dull appearance of the fracture surface. Fracture processes that require much less energy, produce bright, light-reactive fracture surfaces, and are accompanied by little or no plasticity are commonly referred to as brittle. Ductile fracture mechanisms are associated with plastic deformation, disbonding inclusions, microvoid nucleation at the second phase particles or at inclusions as illustrated in Figure 4.1 (ASNT 2005, Garrison and Moody 1987, Hossain et al. 2012, Hossain et al. 2013, Ohira and Pao 1986, Ruggieri 2004), and microvoid coalescence. Several studies have shown that micro-voids are formed ahead of the fracture surfaces in steel (Beachem 1963, Bluhm 1966, Gurland and Plateau 1963, Liu 1968, Puttick 1959, Rogers 1960, Tipper 1949). Intense deformations enlarge the micro-voids, and nucleate further micro-voids at precipitate interfaces (in the ligaments between the voids) (ASNT 2005, Hossain et al. 2013, Puttick 1959, Tipper 1949). Further load cycles cause shearing of the ligaments between microvoids, thus leading to macro-scopic crack growth. Earlier studies demonstrated the key role of micro-voids during crack propagation associated with ductile fracture in steel (Puttick 1959, Tipper 1949). The most likely mechanism is the fracture of inclusions or their de-cohesions from the matrix as the plastic zone passes through them (ASNT 2005). Upon increased plastic deformation, this internal crack progresses until sufficient loss of cross-sectional area leads to final failure of the specimen by a plastic collapse mechanism of the remaining ligament. Therefore ductile fracture in steels is the fracture by the growth of holes (McClintock 1968).

Ductile fracture by internal necking of cavities (Thomason 1968), is caused by the large growth and coalescence of microscopic voids (Rice 1969) and is via the nucleation and growth of voids (Gurson 1977). Hence ductile fracture by void growth and coalescence involves three stages: microvoid nucleation, void growth, and void coalescence (Bates 1984, Gladman 1997, Thomason 1990, Thomason 1998).

Voids might nucleate at cleaved particles (Cox 1974, Gladman 1971) or by de-cohesion of the interfaces of the second phase particles (MnS, carbide etc.). Smaller particles require higher applied stresses for de-cohesion than larger ones (Argon and Im 1975, Argon et al. 1975, Beachem 1975). Bates (1984) showed that carbides play a critical role in brittle fracture mechanisms. Stress tri-axiality has a dramatic effect on void growth type and therefore on strain to fracture (Bridgman 1952) which causes some volumetric growth (Gladman 1997, Thomason 1998) and therefore significantly lowers the strain to rupture. Void coalescence is a process involving a localized internal necking of the intervoid material (Thomason 1981). The final stages of this process are associated with failure of the sub-micron intervoid ligament by shearing along crystallographic planes or by micro-cleavage (Cox 1974, Rogers 1960).

Previous studies have shown that a dislocation pile-up at an obstacle, such as a grain carbide interface, can cleave a grain boundary carbide and thus initiate a micro-crack (Lin et al. 1987, McMahon and Cohen 1965, Thompson and Knott 1993), which is associated with brittle fracture mechanisms. Some degree of plastic deformation in a ferrite grain is necessary to fracture a neighboring carbide (Lin et al. 1987). The number of cracked carbides increases with increasing applied strain (ASNT 2005). Indeed the number and intensity of dislocation pile-ups increases with plastic straining and hence the stresses required to generate a micro-crack decrease (Gurland 1972).

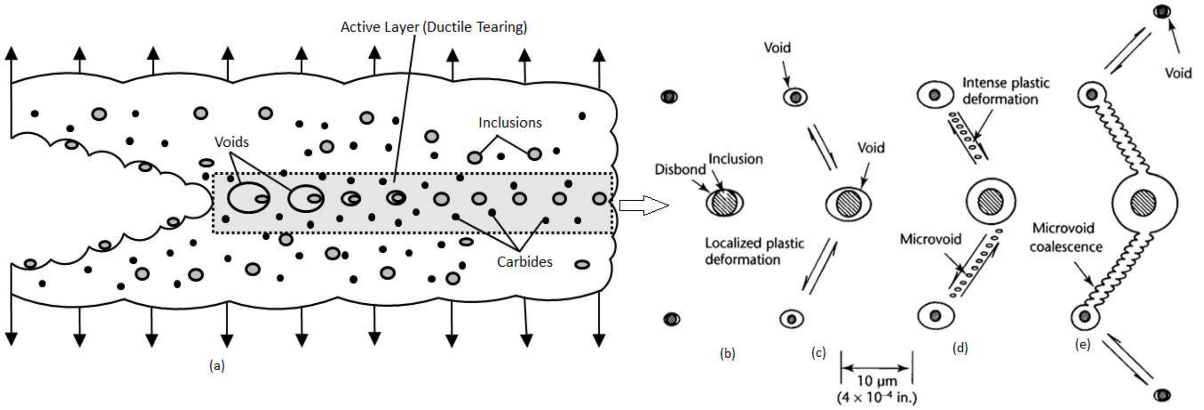

Figure 4.1. Sequence of micro-mechanisms: (a) void nucleation and growth (Ruggieri 2004); (b) disbonding at inclusion-to-matrix interfaces; (c) void growth at interface and plastic deformation between adjacent voids; (d) nucleation of additional microvoids at precipitate interfaces;and (e) coalescence of microvoids resulting in a ductile crack (redrawn after ASNT 2005).

Exactly how these two mechanisms take place on a micro-scale and produce acoustic emission (Figure 4.2) has been an item of interest for experimental research over the last several decades. Many of the earlier studies were hampered by a lack of experimental resources, and none of the studies showed a clear linkage between failure mechanisms in A572 Grade 50 steel and characteristics of the associated acoustic emission. This study builds upon previous work, and critically examines micro-mechanisms of AE sources during fatigue crack propagation in steel material based on the fractographic examinations of the fractured surface through scanning electronic microscopy (SEM) and b-value analysis.

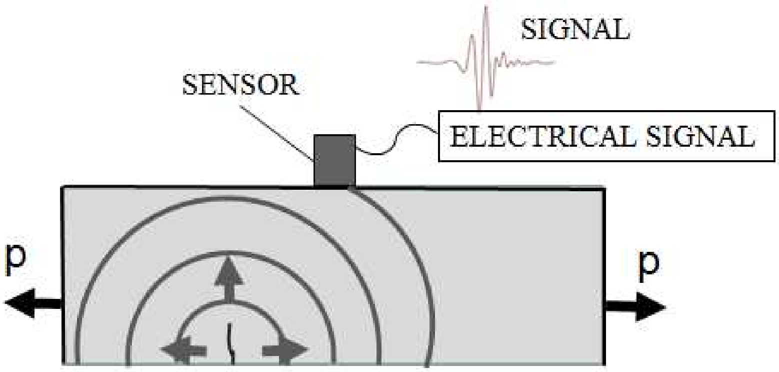

Figure 4.2. Schematic of acoustic emission process.

4.2 SOURCE MECHANISMS AT THE MICRO LEVEL

Ductile Mechanisms:

Thomason (1993) studied the details of the coalescence phenomenon which is considered the final stage of ductile failure mechanisms and showed incipient void coalescence leading to an instantaneous change from incompressible to dilatational plasticity. The condition for the onset of coalescence in a plane strain case has the following form:

$$(\sigma_{Ic} - \sigma_I)\, \varepsilon_{Ic} = 0 \tag{4.1}$$

where σ_{Ic} is the plastic limit-load stress, σ_I is the maximum principal stress, and $\dot{\varepsilon}_{Ic}$ is the maximum principal strain rate across an intervoid matrix neck. If voids are considered as cylindrical then σ_{Ic} can be represented by the following empirical equation (Thomason 1998):

$$\sigma_{Ic} = 2k(1.43 \cdot f^{-1/6} - 0.91) \tag{4.2}$$

where k is the maximum shear stress, $k = \sigma_I - \sigma_m$, [$(\sigma_m = (\sigma_1 + \sigma_2 + \sigma_3)/3 =$ mean stress] and f is a void volume ratio. Thus a micro-crack extension occurs when the condition of equation (4.1) is met. The material rate of hardening in the intervoid matrix approaching ductile fracture is reduced to a very low level and in most cases microvoids do not show significant growth before the onset of coalescence (Thomason 1998). However, if constraint is very high and if very few void nucleation cites are present then volumetric void growth can be very strong.

Huang et al. (1991) analyzed a single spherical void in elastic-plastic materials under a remote stress field and showed that a complex interaction of elasticity and plastic yielding can lead to a “cavitation instability", if the stresses in the material surrounding the void are sufficiently high so that the work produced by these stresses to expand the void is less than the energy released by such expansion. An analogy can be drawn between the above analysis of the cavitation instability and the energy condition of Griffith (1924) for unstable crack growth.

Brittle Mechanisms:

A significant research effort has been made in understanding brittle crack growth mechanisms since Griffith's day (Griffith 1924). A dislocation may pile-up at an obstacle, such as a grain carbide interface, splitting the grain boundary and thus initiating a micro-crack (Lin et al. 1987, McMahon and Cohen 1965, Thompson and Knott 1993). Thus some degree of plastic deformation in a ferrite grain is always necessary to fracture a neighboring carbide (Lin et al. 1987), which may require several load cycles. The stresses required to generate a micro-crack can be written as follows (Hahn 1959):

$$\tau = 4.4 \cdot \gamma / na \tag{4.3}$$

$$\sigma = K \cdot \gamma / na \tag{4.4}$$

where τ and σ are shear and normal stresses accordingly, γ is an effective surface energy, n is the number of dislocations piled up against a grain boundary, a is the atomic spacing, and K is a coefficient depending on the arrangement of the dislocation pile-up (K = 2.7 for Orowan model; K = 5.3 for Bullough model; or K = 2.0 for Cottrell model according to Hahn et al. 1959). Equations (4.3) and (4.4) suggest that the number of cracked carbides increases with increasing applied strain. Indeed the number and intensity of dislocation pile-ups increases with plastic straining and hence the stresses required for the generation of a micro-crack decrease. This point has been supported by experimental observations (Gurland 1972). A micro-crack in a cleaved carbide can advance if the following condition is met: $\sigma_n \geq \sigma_F$, where σ_n is a normal stress acting across the grain-carbide interface and σ_F is a fracture or cleavage stress.

Smith (1966) derived an equation for the fracture stress of a carbide-ferrite interface. Based on Smith's analysis, Lin et al. (1987) obtained a similar equation for the fracture stress of a ferrite-ferrite interface. Both equations are shown below.

$$\sigma_F^{cf} = \sqrt{\pi E \gamma_{cf} / \{d_c (1-\nu^2)\}} \tag{4.5}$$

$$\sigma_F^{ff} = \sqrt{\pi E \gamma_{ff} / \{d_g (1-\nu^2)\}} \tag{4.6}$$

where σ_F^{cf} and σ_F^{ff} are the fracture or cleavage stresses of a carbide-ferrite and ferrite-ferrite interfaces, γ_{cf} and γ_{ff} are the effective surface energies of a carbide-ferrite and a ferrite-ferrite interface; d_c and d_g are carbide and ferrite grain sizes, E is the elasticity modulus, and ν is Poisson's ratio. Ritchie et al. (1973) showed that the condition $\sigma_n \geq \sigma_F$ has to be satisfied over a distance of two grain sizes ahead of the crack tip for the fracture advance to take place. This is commonly called the critical distance idea (Thompson and Knott 1993). Later Curry and Knott (1978) proposed a statistical analysis of eligible particles that can be found within the critical distance. An eligible particle is a cracked particle with the crack length equal to or greater than the critical one. Their conclusion was that a very small percentage of large particles have a predominant influence on the fracture resistance.

4.3 CT SPECIMEN TESTING AND AE MONITORING

To investigate the potential sources of acoustic emission due to fatigue crack extension, a compact tension specimen of ASTM A572 Grade 50 structural steel was utilized for acoustic emission monitoring during constant amplitude cyclic loading (Figure 4.3). The chemical composition is given in Table 4.1. The effective width of the

CT specimen is 241.3 mm (9.5 inch) and the thickness is 12.7 mm (0.5 inch), with initial crack length of 82.6 mm (3.25 inch).

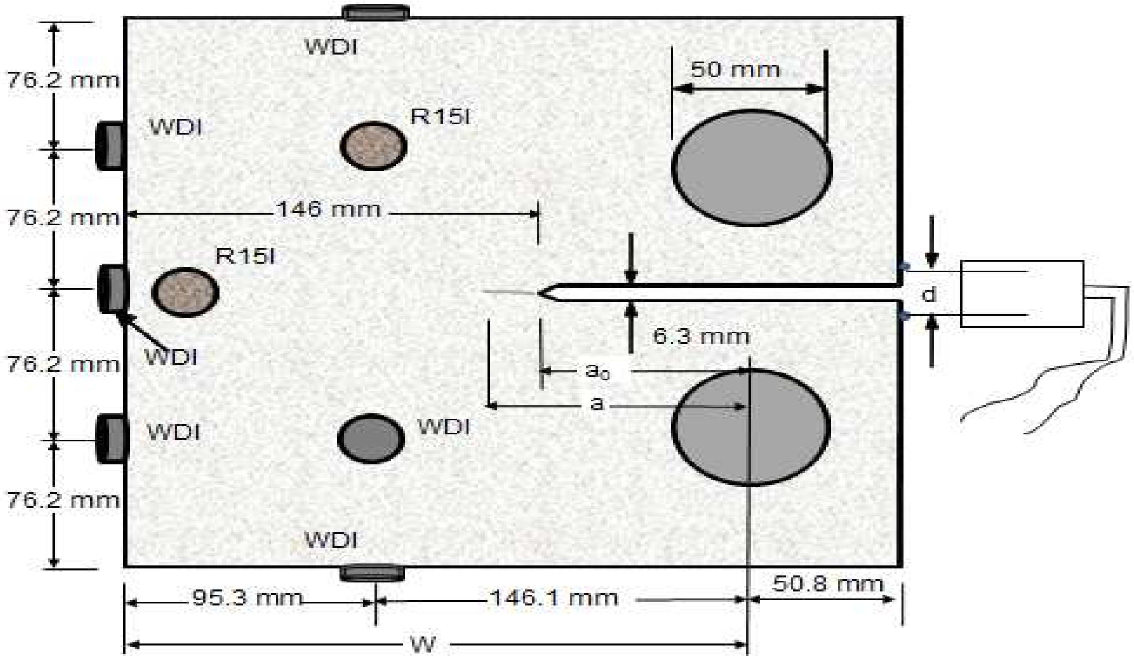

(a) schematic

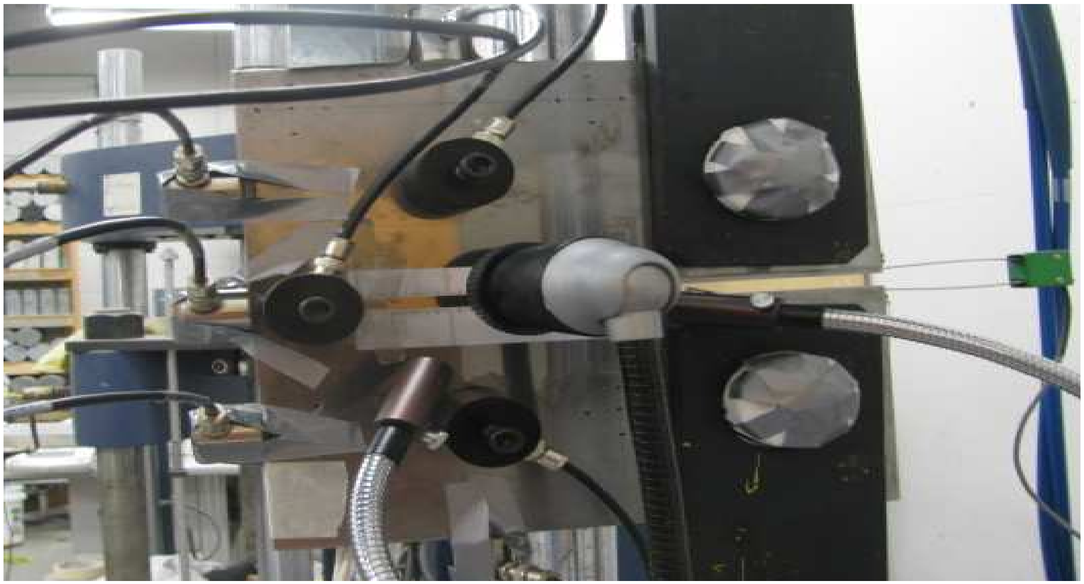

(b) photograph during testing

Figure 4.3. Compact tension (CT) specimen

A clip gage, Vishay crack propagation gages, and a microscopic video camera were used to monitor crack propagation. An MTS 810 test frame was used to apply cyclic load, with a maximum applied load of 65 kN (14.6 kips) with a load ratio (R) of 0.1 and a frequency of 2 Hz. Two R15I-AST and six wideband (WDI) sensors (Mistras Group, Inc.) were used to collect AE signals. Vacuum grease was used as the couplant and magnetic holders were used to maintain constant pressure. The AE signals have internal pre-amplification of 40 dB. The test threshold was 45 dB and signals were stored and displayed with a Sensor Highway II data acquisition system having AEwin software.

Table 4.1. Chemical Composition of ASTM A572 Grade 50 Steel

Element	**Weight %**
Iron (Fe)	Base metal
Manganese (Mn)	1.35 (max)
Silicon (Si)	0.30% (max)
Carbon (C)	0.23% (max)
Copper (Cu)	0.20% (min)
Sulfur (S)	0.05%
Phosphorus (P)	0.04%

Filtering Approach:

Signal identification and data filtering is a necessary step for acoustic emission monitoring. In addition to plastic deformation and crack extension, AE sensors are also sensitive to unrelated noise. Noise mainly arises from grating between fracture surfaces and abrasion in the load train. Grating emission occurs due to friction between the fractured surfaces at crack closure and crack opening. To minimize grating emission, AE collected below 80% of the maximum load was eliminated (Hossain et al. 2012, Hossain et al. 2013, Yu et al. 2011).

Specialized grating emission tests were performed to understand the characteristics of noise due to grating. In these tests, the magnitude of the cyclic load was reduced so as to be insufficient for crack growth. A typical waveform from grating emission is shown in Figure 4.5(a). Pencil lead break tests were also performed to understand the characteristics of genuine hits [Figure 4.5(b)]. In a burst-type waveform, typical parameters include amplitude, rise time, duration, and emission counts. The waveform from grating emission has long rise time, long duration, and poorly defined peak amplitude. The waveform from crack related events is characterized by a relatively clean front-end, short rise time, short duration, and high amplitude. Based on the characteristics of waveforms, Swansong II filtering was also employed to minimize mechanical noise. Swansong II filtering utilizes a technique which takes advantage of specific characteristics of unwanted hits (longer duration and low amplitude), as AE hits arising from sliding or mechanical rubbing typically have relatively longer duration and lower amplitude.

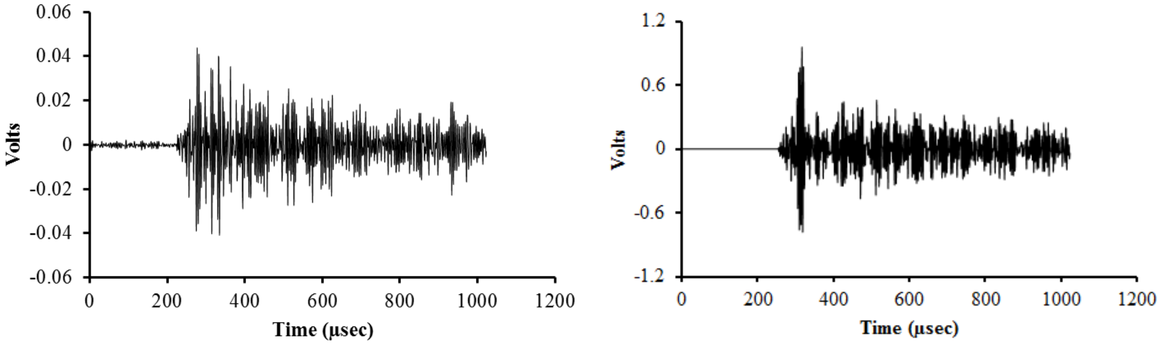

(a) grating emission

(b) pencil lead break test

Figure 4.4. Typical waveforms

Fatigue Crack Growth Rate:

A clip gage was used to record the crack mouth opening displacement (CMOD), ‘d’ (shown in Figure 4.3) and then the ASTM (2006) empirical expression was used to calculate the crack length, ‘a’ (from the center of the loading line, Figure 4.3). The empirical expression is:

$$\mathrm{a} = \mathrm{W}(1.001 - 4.6695u_x + 18.4u_x^2 - 236.82u_x^3 + 1214.9u_x^4 - 2143.6u_x^5) \qquad (4.7)$$

$$u_x = \left[\sqrt{E \cdot t \cdot d / P_{\max}} + 1\right]^{-1} \qquad (4.8)$$

where the effective width of the CT specimen (W) is 241.3 mm (9.5 inch) as shown in Figure 4.3 and the specimen thickness *t* is 12.7 mm (0.5 inch); the Young’s modulus (*E)* of ASTM A572 G50 steel is 200 GPa (29000 ksi) and P_{max} is the peak of the cyclic load. The stress intensity range is determined by using the following equation (ASTM 2006):

$$\Delta K = \frac{\Delta P.(2+\alpha)}{tw^{1/2}(1-\alpha)^{3/2}}(0.886 + 4.64\alpha - 13.32\alpha^2 + 14.72\alpha^3 - \qquad (4.9)$$

where ΔP= P_{max}-P_{min} and *α* is equal to *a*/*W*. By using equation (6.14), the calculated critical crack length, a_c = 55.4 mm (2.18 inch) (from initial crack tip) when the maximum stress intensity at the crack tip reaches to 128 MPa√m (116.5 ksi√in) (Stephens et al. 1982, Yu et al. 2011).

As the stress intensity range approaches the critical value of fracture toughness (K_c), the fatigue crack growth becomes much faster than that predicted by Paris law (1961). Therefore, ΔK is the driving force for crack propagation, and it includes the effect of the changing crack length and cyclic loading. AE transducers are usually made from piezoelectric slabs and have a resonant behavior; their sensitivity varies with frequency

(f_t) and is usually greatest in the range from 0.1 to 1.0 MHz (ASNT 2005). Neither the static surface strains nor very high frequency components are sensed. If the crack extends rapidly and then stops so that its growth time is about equal to $1/f_t$, then the emitted wave fronts are dominated by frequency components in the detectable range (ASNT 2005).

Therefore, the detectability of crack growth events with the acoustic emission method depends on the temporal nature of the source. If the source operates slowly then it is likely no signal will be detected. But if the crack extends rapidly and then stops so that its extension time is about equal to $1/f_t$, the emitted wave forms are dominated by frequency components in the detectable range. Hence, the time-dependent nature of the source mechanism controls the potential detectability.

4.4 RESULTS AND DISCUSSION

Acoustic Emission Data:

Local crack extension was monitored using crack propagation gages (CPAs) in combination with a clip gage to assess the AE events associated with fatigue crack extension. CPAs consist of twenty breakable metallic grid lines (0.02 inches apart) having known electrical resistance. In the majority of the cases (78%), AE hits were not recorded due to wire breakage. This suggests that AE is generally not produced by breakage of the grid line itself. This study is focused on stable fatigue crack growth (Stage II) of in-service steel bridges, so stage I (crack nucleation) and stage III (unstable crack growth, leading to catastrophic failure) are not discussed in detail.

To enable the discussion that follows, the stages of crack growth are defined as follows:

- Early stage II: Stress intensity range (ΔK) is in the range of 57 MPa√m (51.9 ksi√in) (corresponding to the initial crack length) to 60 MPa√m (54.6 ksi√in).
- Mid stage II: Stress intensity range (ΔK) is the range of 60 (54.6 ksi√in) to 95 MPa√m (81.9 ksi√in).
- Late stage II: ΔK is in the range of 95 (81.9 ksi√in) to 128 MPa√m (116.5 ksi√in) near the critical level fatigue crack where the fatigue crack is much faster than calculated using the Paris equation.
- Early stage III: Stress intensity range (ΔK) is between 128 MPa√m (116.5 ksi√in) and 135 MPa√m (122.9 ksi√in) (end of the test).

The total number of AE hits recorded throughout the test was 312,527. By visual inspection of the waveforms, many of the AE hits are considered as hits associated with the grating or friction between the fracture surfaces during opening and closure of the crack. In a previous study it was presumed that fatigue crack extension occurs within 80% of the peak load (Yu et al. 2011). To eliminate hits associated with the grating emissions, hits occurring below 80% of the peak load were filtered. Less than 1% of the hits remained after applying this load based filter along with the Swansong II filter previously described [Figure 4.5].

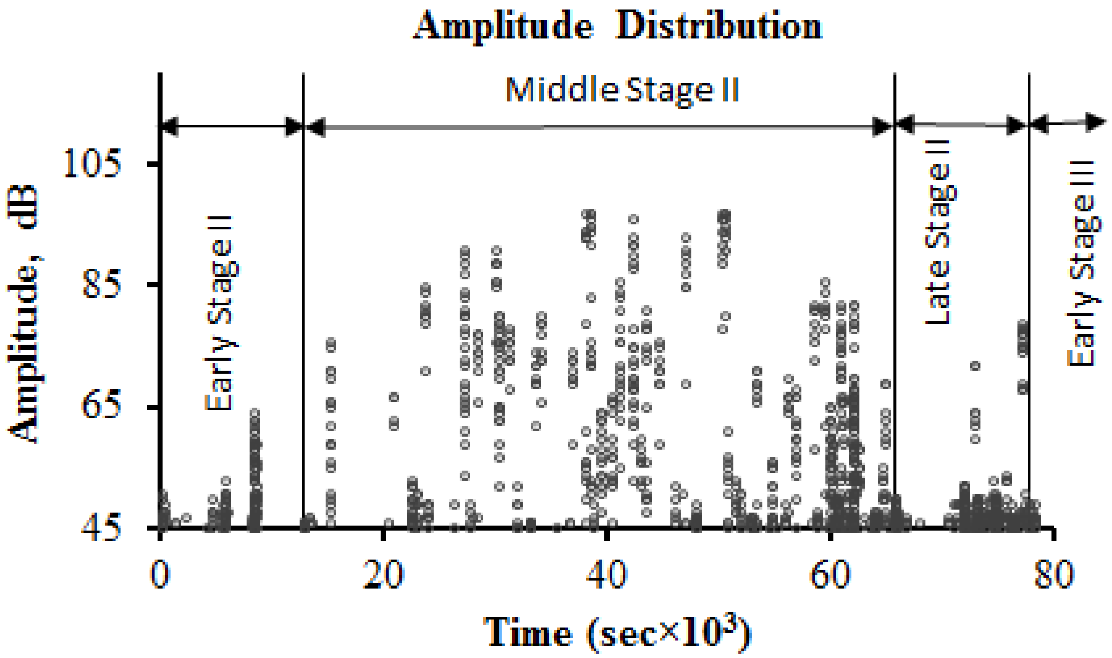

(a) AE hits versus time

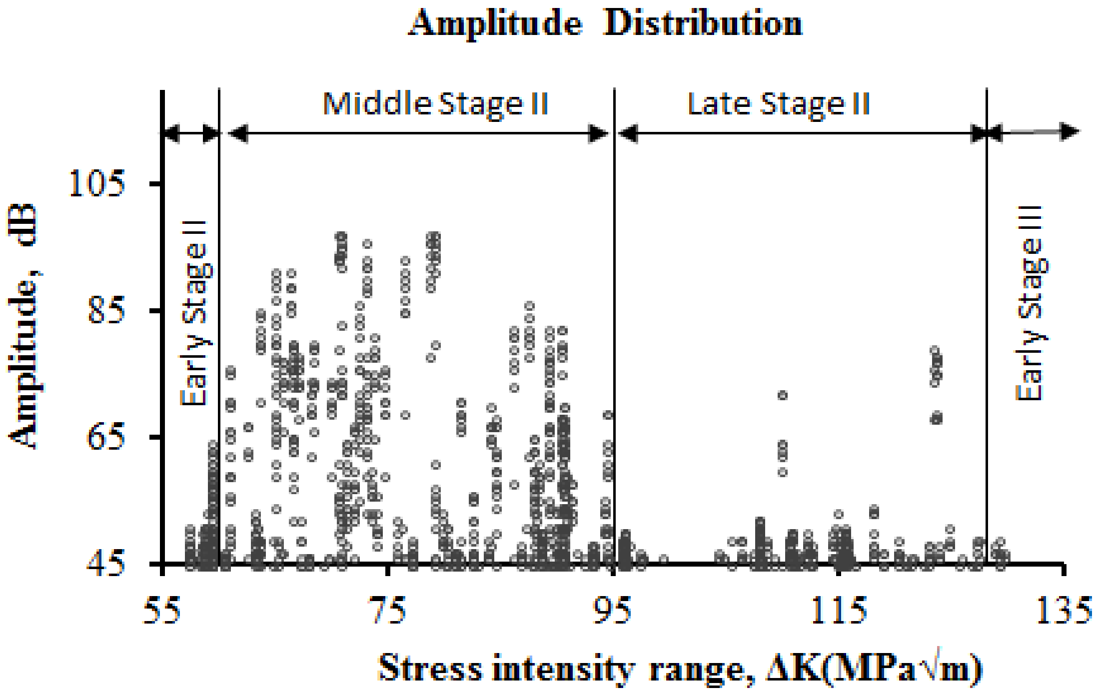

(b) AE hits versus stress intensity range

Figure 4.5. AE amplitude distribution after filtering below 80% of maximum load and Swansong II.

In early stage II [stress intensity range (ΔK) less than 60 MPa√m (54.6 ksi√in)], no AE hits were recorded due to fatigue crack extension. This observation is based on the data received from the Vishay crack propagation gages. Relatively low amplitude AE events (in the range of 45 to 65 dB) were recorded throughout early stage II. This observation indicates that the majority of AE hits in this stage were associated with ductile mechanisms. During ductile mechanisms energy release occurs in step by step processes (inclusion disbanding, micro-void generation, and coalescence) over a wide span of time. This is in contrast to the later stages where the brittle fracture mechanisms dominate and produce high amplitude acoustic emission.

In mid stage II [ΔK in the range of 60 (54.6 ksi√in) to 95 MPa√m (81.9 ksi√in)], high amplitude AE events in addition to low amplitude AE events were observed with increasing stress intensity range. Relatively high amplitude hits in the range of 70 to 95 dB accompanied by wire breakage of the Vishay crack gages were observed, which may be associated with brittle crack extension. In late stage II [ΔK in the range of 95 MPa√m (81.9 ksi√in) to 128 MPa√m (116.5 ksi√in)] and also in early stage III [ΔK greater than 128 MPa√m (116.5 ksi√in)], the stress intensity range (ΔK) is relatively high and dramatically increases, leading to unstable crack growth. Within a very short period of time (around one thousand seconds), ΔK is changed from 95 (81.9 ksi√in) to 128 MPa√m (116.5 ksi√in) near the critical level fatigue crack.

The average crack growth rate obtained from the test varied from 2.5 to 42 μm/cycle. The energy release during crack growth or *strain energy release rate* per unit area of crack growth is $\Delta G = \Delta K^2 / E$ or $(1-\nu^2)\Delta K^2 / E$ for the plane stress and plane strain conditions, respectively (Griffith 1924). According to the above expressions the energy release should increase with increasing numbers of load cycles and therefore should produce higher amplitude acoustic emission. The same trend can be found in Figure 4.5(a), but it can be seen that high amplitude AE hits are distributed throughout the test, and relatively high amplitude AE hits are found in mid stage II [ΔK between 60 (54.6 ksi√in) to 95 MPa√m (81.9 ksi√in)]. In early stage II (delta K between 57 to 60 MPa√m), the amplitude of the AE hits was smaller and no high amplitude AE hits were observed. However, with increasing ΔK, the frequency of high amplitude AE events increased which suggests that with increasing ΔK, the chance of brittle fracture mechanisms is increased. In mid stage II [ΔK between 60 (54.6 ksi√in) to 95 MPa√m (81.9 ksi√in)] the highly energetic AE hits have amplitude in the range of 70 to 95 dB [Figure 4.5 (b)]. However, throughout the fatigue test, most of the AE hits have amplitude in the range of 45 to 65 dB which suggests the majority of the AE events are less energetic. Therefore, it takes several hundred loading cycles to produce a brittle fracture and hence produce a high amplitude AE event. In the region at the end of stage II and the beginning of stage III, very few energetic events were observed. In this region the stress intensity range quickly increased, so hypothetically high amplitude AE events should increase, however this was not observed in the AE data. The reason may be the decrease in the material resilient at this region and the crack propagates mainly via transgranular mechanisms.

b-value Analysis:

There can be many sources of AE, with one of the most important being micro-cracking as far as brittle failure is concerned. This has motivated non-destructive testing (NDT) specialists to develop and refine the AE technique such that it can serve as an NDT tool for monitoring and understanding the mechanisms of dynamic processes and also to forewarn impending failure in engineering materials. Among various parameters, the most significant one is the b-value which is derived from the amplitude distribution data of AE. It represents the 'scaling of magnitude distribution' of AE, and is a measure of the relative numbers of small and large AE which are signatures of localized failures in material.

b-value is an effective tool to characterize AE sources. Pollock (1981) suggested the “average AE amplitudes”, for calculation of b-values:

$$\overline{A} = A_0 + \frac{20}{b \ln 10} \tag{4.10}$$

where $\overline{A}$ = average amplitude, A_0 = threshold amplitude, and b = the calculated b-value. The plot of b-value vs. stress intensity range is a potentially promising way to analyze source mechanisms of AE during fatigue crack growth. The advantages of this method are that it is easy to compute, can be performed in real time, and is easy to understand. It has been shown by Pollock (1981) that the b-value is unique for each failure mechanism, and the log scale will remove the effect of wave attenuation. Therefore, the b value will not change with the distance between source to sensor, if all signals are attenuated equally (Pollock 1981). The b-value can change during a test, which can be explained as the transition from one mechanism to another.

Pollock (1981) also stated that commonly the b-value range is between 0.7-1.5, but it could be as low as 0.4 or as high as 4.0. The lower values are usually associated with discontinuous crack growth in high-strength brittle metals, whereas the high values can be from plastic zone growth prior to crack extension.

The discrete cleavage events that occur during stage II fatigue crack growth should have a random distribution along the crack propagation path. Total fracture surfaces associated with cleavage fracture can then be subdivided into discrete increments based on the b-value. The smallest discrete increment which can produce detectable acoustic emission can then be considered as one “grain” (Pollock 2010).

AE data was processed using *Matlab code* (MATLAB 2010) to carry out a *b*-value analysis. AE data was grouped as Group I (full data set without filtering) and Group II (AE data filtered below 80% of the maximum load and combined with Swansong II). Then the *b*-values versus stress intensity range were plotted for Group I (all channels combined as well as for the individual channels). For Group II all channels were plotted together as there was not enough data to plot for individual channels. For a single b-value calculation, one hundred data points (hits) were used. After employing load filtering and Swangsong II filtering, around two hundred data points per channel remained and therefore it was not meaningful to plot only two points per channel which eventually results in a straight line and does not provide any insight related to the sources.

Using different numbers of AE hits can significantly affect the calculated b-value. Using 100 data points for calculation, the resulting average b-values are about 0.176 for Group I and 0.0655 for Group II (over the entire test) for all channels combined. This implies that the filtering process significantly affects the *b*-value. Another conclusion is that mechanical noise has higher b-value as it produces relatively low amplitude AE. With consideration to the case of in-service steel bridge health monitoring and prognosis, AE data may be collected and b-value plotted against stress intensity range to assess the AE hits associated with fatigue crack growth.

Figure 4.6 shows the synchronization between b-value (Group I) and the AE hits (raw data, Group I). The b-value is highly fluctuated for Group I. The accuracy of *b*-value depends on meaningful data, sample size, and appropriate methods of calculation. A large number of unfiltered data resulting in the greater error, and sometimes the results can not be used to accurate source characterization which describes the rate at which AE hits of specified amplitude generate at a given location.

For each AE hit, the source characterization develops a suite of credible and relevant AE scenarios (amplitude) and computes the rate at which each AE hits occur.

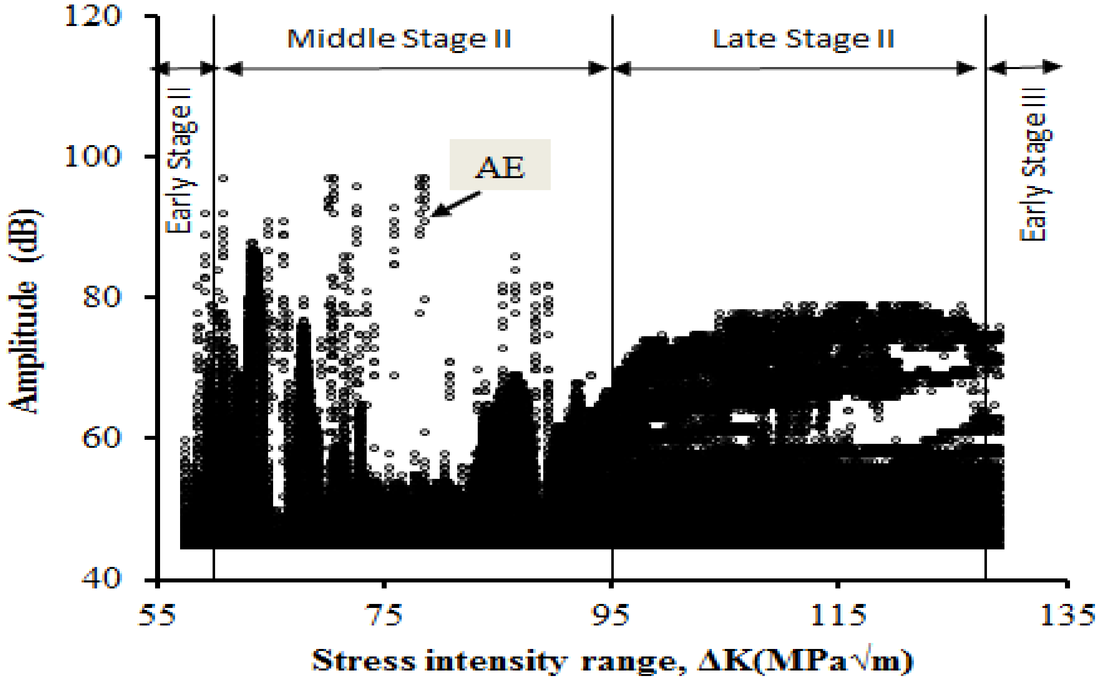

(a) AE amplitude (raw data) verus stress intensity range

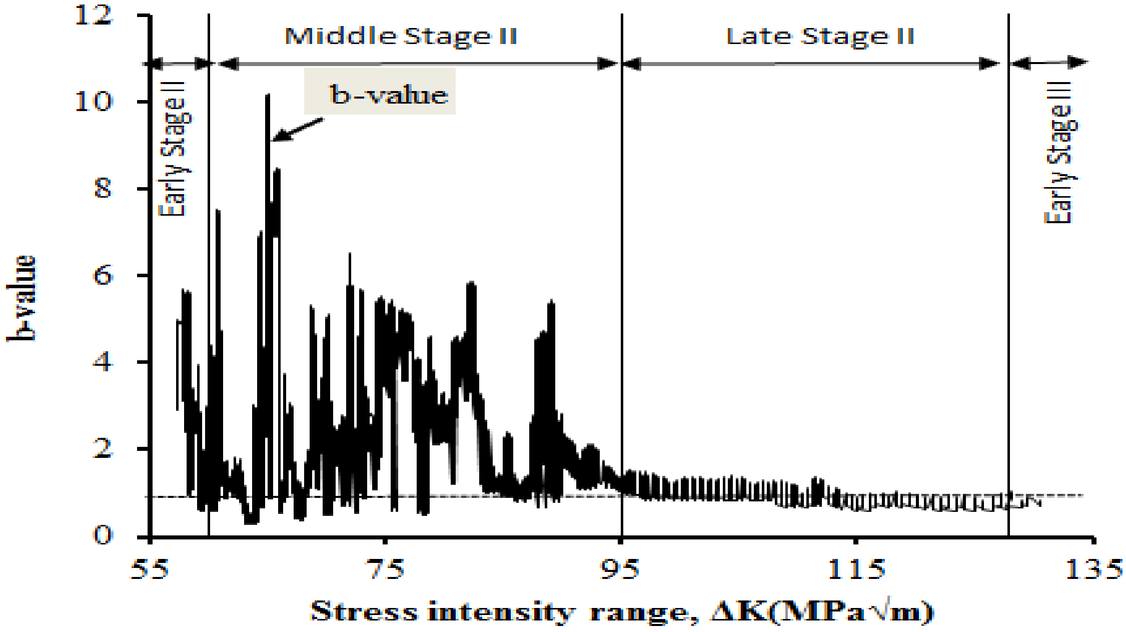

(b) b-value (based on raw AE data) versus stress intensity range

Figure 4.6. AE amplitude and b-value distribution for raw data.

The b-value depends on the amplitude of AE hits, and lower b-values as shown in Figure 4.6 represent higher amplitude AE hits and vice-versa, which involves filtering AE hits in a selective manner. Figure 4.6a presents AE hits obtained from the fatigue test, and Figure 4.6b represents the corresponding b-value to aid in assessment of the fracture process. In mid-Stage II, the b-value is found to range from 0.4 to 10. The higher b-value indicates large number of relatively low amplitude AE hits. Friction between fracture surface and mechanical noises may contribute these large number of low amplitude AE hits. In the middle of Stage II, b-value drops below 1.0 several times and it is as low as 0.4, which may be associated with brittle fracture mechanisms. Then relatively large number of high amplitude banded AE hits which may be associated with friction between fracture surfaces; most of these hits are eliminated after employing load filter and Swansong II filter. And corresponding b-value decreases with increase in stress intensity range to attain values ≈ 1.00 in late Stage II and beyond. Therefore conflict between the friction emission and brittle fracture is taken place in some cases. Hence source characterization based on b-value depends on proper data identification as well as proper data filter. b-value may not be directly applied for source characterization prior proper data filtering.

Figure 4.7 shows the filtered AE hits along with the resulting b-value based on the filtered AE data. Early Stage II may be related to crack nucleation and corresponding b-value is in the range of 4.0, mid-Stage II has almost constant b-value ≈ 0.4, late Stage II demonstrates and significant rise in the b-value followed by a drop and then another rise, and finally early stage III demonstrates high b-value, where crack may grow via transgranular fracture. Hence brittle fracture frequently occurs in the middle Stage II and the corresponding b-value is the lowest and it is in the range of 0.4.

However it is difficult to make precise decisions based on the highly fluctuated diagram of the *b*-value for the raw AE data (Group I, Figure 4.6), but for the filtered AE data (Group II, Figure 4.7) the fluctuation in b-value is less and the pattern is clearer in the early cycles when the cracks nucleate. Higher b-values indicate smaller amplitude AE which may be produced by ductile failure mechanisms that involve plastic deformation, inclusion disbonding, microvoid generation, and coalescence. The presence of a large number of concentrated micro-cracks in Group II (filtered data) creates a clear pattern of b-value (Figure 4.7). The dramatic rise in b-value occurs where there is very little high amplitude and large number of small amplitude AE data as shown in the late Stage II. However, once high amplitude AE hits are detected, the b-value diagram is more fluctuating which suggests that the high amplitude AE sources are random and more scattered along the crack line in late Stage II. This may imply that the analysis of the *b*-value is meaningful for understanding the AE source mechanisms as it provides information between the micro-cracking beginning up to the stage where cleavage fractures frequently occur by brittle failure mechanisms in the middle of Stage II as shown in Figure 4.7. In the middle Stage II, b-value is the lowest and it is in the range of 0.4. Therefore the conclusion can be drawn that the small cluster region known as *grain* is associated with brittle fracture mechanisms when b-value attain to 0.4.

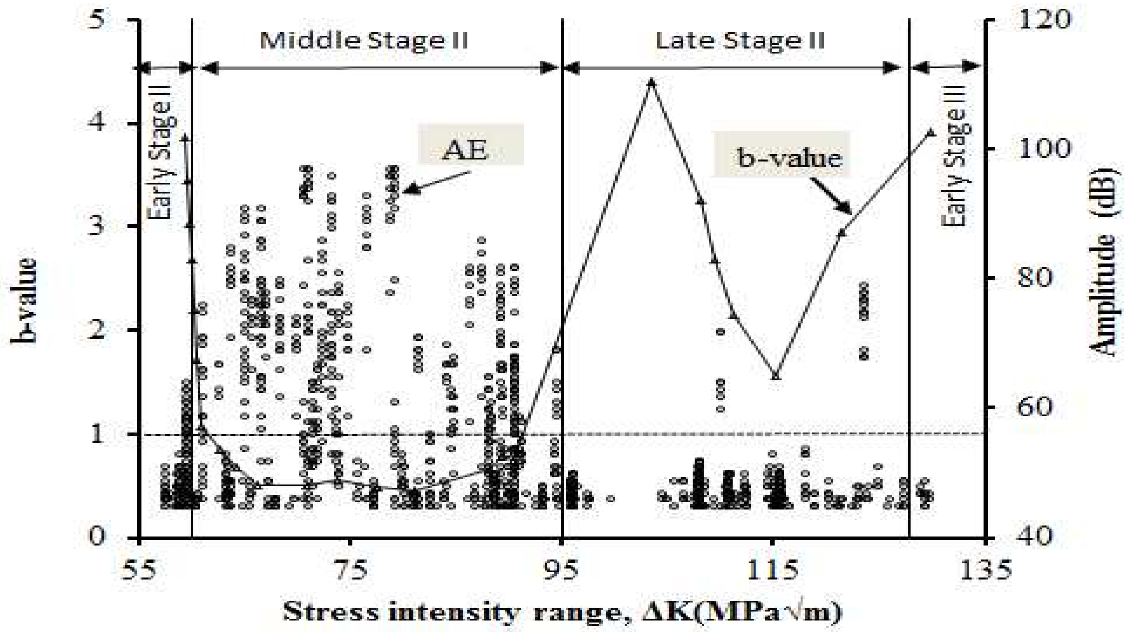

Figure 4.7. AE amplitude (filtered data) and b-value (filtered data) versus stress intensity range.

The trend of the *b*-values is shown for each wide band sensor channel (Channels 1-6) for raw AE data (Group I) in Figure 4.8 and also for each resonant sensor (Channel 7-8) for the raw AE data in Figure 4.9 which show the b-value fluctuates and several times drops below 1.0. However, Figures 4.8 and 4.9 imply that a single channel may not adequate to characterize AE sources and also indicate that filtering is critical to the evaluation of the data. Channel 4 seems to be out of step with the other channels in Stage II [stress intensity range ΔK ≈ 73 (66.4 ksi√in)] and beyond, may be due to the improper attachment or de-attachment of the sensor and lack of proper contact with the plate. Therefore for accurate source characterization, a sufficient number of datasets, sample size and number of AE sensors are obligatory. Optimum number of sensors will minimize this error and will give more accurate b-value prediction as well as the accurate AE sources and associated AE signals. The b-values as presented in Figures 4.8 and 4.9 for unfiltered data, which contain a large number of small amplitude AE hits, rarely drops below 1.0. Thereafter it can be concluded that AE data from individual channels may not adequately identify source mechanisms based on the b-value.

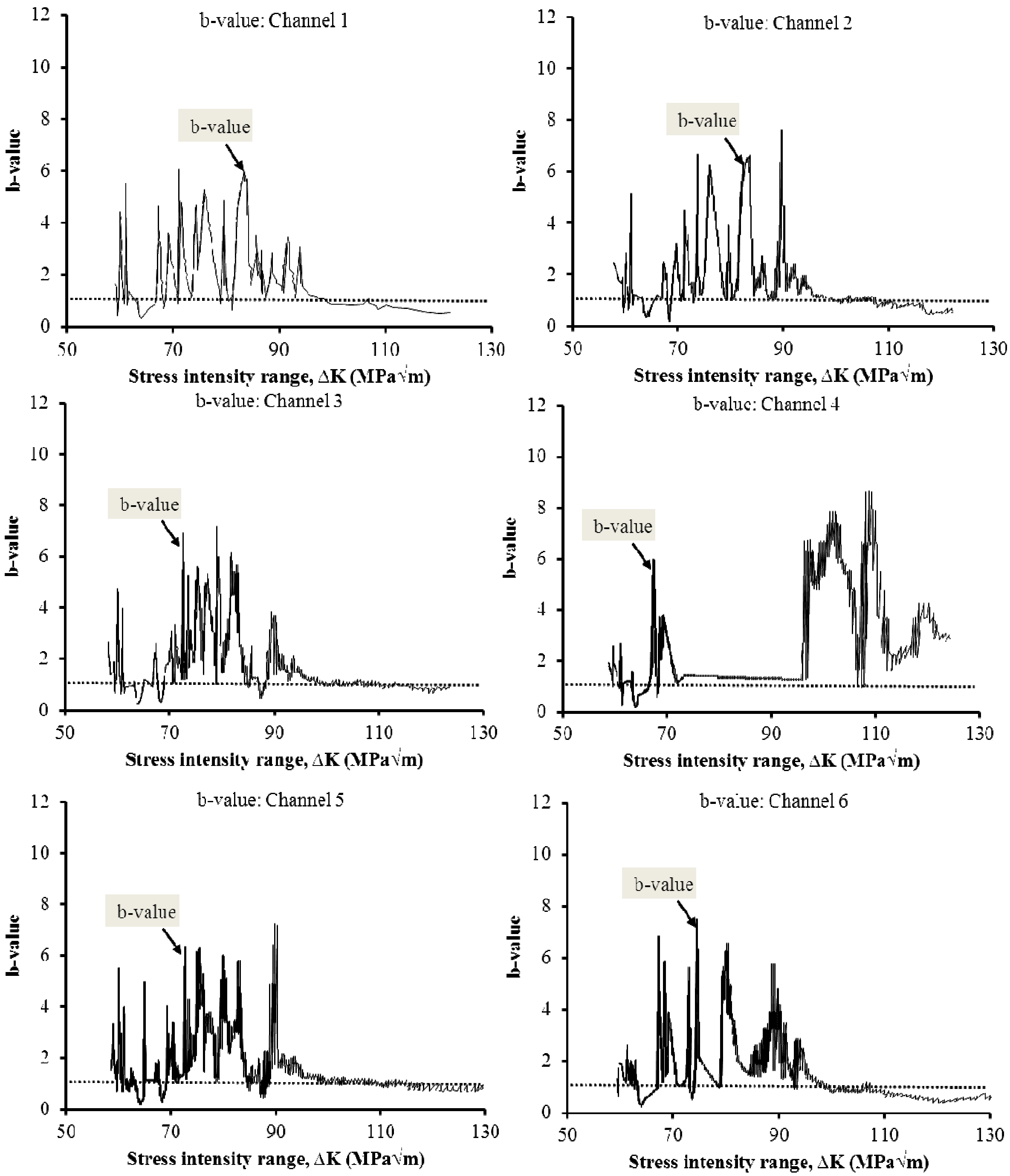

Figure 4.8. b-value versus stress intensity range for WDI sensors (raw data, Group I).

Based on the relationship discussed in the previous sections between the *b*-value and the ductile and brittle failure mechanisms, the minimum *b*-value suggests high amplitude AE events may be associated with cleavage fracture and vice-versa. A higher b-value arises due to a large number of small AE hits (or events) representing new micro-voids formation and slow crack growth, whereas a low b-value indicates faster or unstable crack growth accompanied by relatively high amplitude AE in large numbers as shown in Figures 4.8 and 4.9. Thus there are good prospects for making a quantitative diagnosis of the fracture process in the test material under stress on the basis of AE amplitude information in terms of b-value.

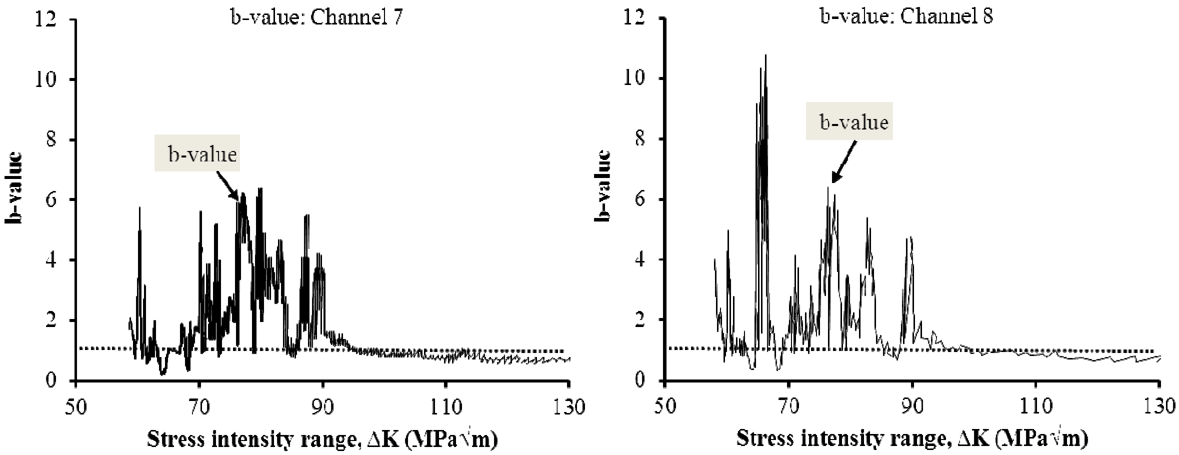

Figure 4.9. b-value versus stress intensity range for R15 sensors (raw data, Group I).

However, the method used for the determination of b-value is important, since selection of the amplitude or magnitude limits of the 'linear range' of the cumulative frequency distribution data of AE is critical. The method used in this study for calculating the b-value is the average amplitude for 100 hits and plotted against the midpoint of these hits. This eliminates effort for choosing optimum amplitude range for determining b-value which is the slope of frequency distribution of a group of AE hits. This implies that the optimum grouping of the amplitude significantly affects the b-value.

All the individual mechanisms (inclusion, microvoids and coalescence) during ductile failure can produce small amplitude AE signals which contribute to AE data depending on the hit. In contrast to ductile mechanisms, cleavage fracture is a very uncertain phenomena depending on the strain rate as well as material properties. Cleavage fracture frequently occurs at higher strain rates during stable fatigue crack growth. For cleavage or intra-granular fracture of ferrite grains, initially micro-cracks nucleate at iron carbide particles on ferrite particles. Carbide particles help to nucleate micro-cracks on ferrite particles. It can be concluded that cleavage fractures frequently occur at higher stress if the ferrite grain contains any initial defects during the manufacturing process of steel which accelerates the micro-crack nucleation process.

In the absence of any micro-crack nucleation factors on ferrite grains, there is more chance to extend the crack by debonding the matrix between two ferrite grains which is known as transgranular cleavage fracture. Figures 4.7 through 4.9 show that after around 1,000 seconds the b-value first drops below 1.0 when the corresponding stress intensity range is between 60 MPa√m (54.6 ksi√in) to 65 MPa√m (59.2 ksi√in), which may be associated with the beginning of brittle fracture mechanisms which produce high amplitude acoustic emission. The following conclusion can be drawn that the AE hits corresponding to b-value less than 1.0 are associated to brittle mechanisms.

Source Characterization with Electron Microscopy:

As discussed in the previous sections, it is hypothesized that only a small fraction (ψ) of the total crack surface is associated with highly emissive mechanisms such as trans-granular or inter-granular cleavage. The balance of the fracture, perhaps a large majority of it, is created by essentially silent mechanisms such as plastic deformations, inclusion disbonding, microvoid generation, and microvoid coalescence. In fatigue crack growth as discussed in previous sections, there are two main types of failure mechanisms. Ductile mechanisms can be considered as salient failure mechanisms as they produce more acoustic emission having small amplitude. In contrast, brittle fracture mechanisms, such as cleavage fracture, produce less frequent but higher amplitude acoustic emission. The brittle fracture fraction (ψ) is the key descriptor of material emissivity and can be assessed by fractographic analysis.

At the conclusion of fatigue testing, samples were cut (1 and 2 from early Stage II, 3 and 4 from mid Stage II, and 5 and 6 from late Stage II) from the fracture surfaces of the CT specimen as shown in Figure 4.10 and examined with a Scanning Electronic Microscope (SEM). In early Stage II (crack length around 15 mm), the fracture surface was dominated by microvoid coalescence [Figure 4.11(a) and (b)]. In mid Stage II (crack length around 30 mm) [Figure 4.11(c) and (d)] the fracture surface shows quasi-cleavage with some traces of fatigue striations [Figure 4.11(c)]. The striation spacing, approximately 1μm, is compatible with the crack growth rate (2.5- 42.4 μm/cycle) observed in this stage of the test. The quasi-cleavage appearance persisted to late Stage II (crack length around 50 mm) [Figure 4.11(f) and (g)]. Figure 4.11(a) and (b) show micro-voids and coalescence (separation) which is indicative of ductile failure mechanisms.

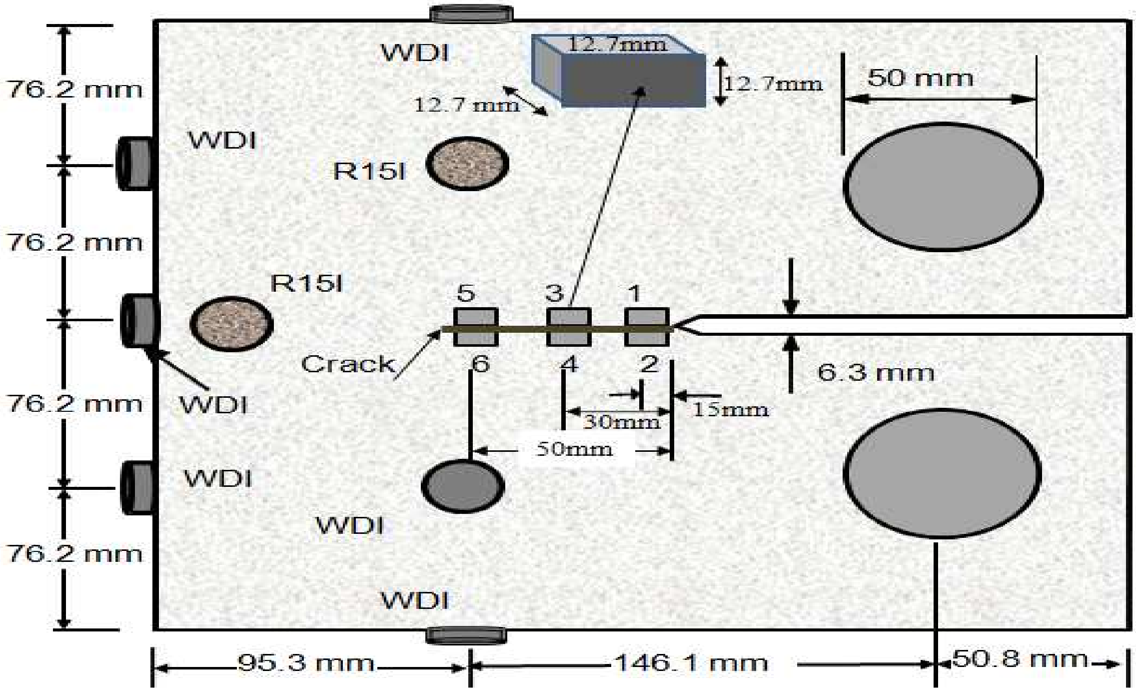

Figure 4.10. Schematic diagram for the locations of SEM images.

Macroscopic examination of the fracture surface may also permit discrimination of the fatigue fractures. The classic feature associated with fatigue crack growth is the formation of fatigue striations. The typical appearances of ductile fracture in steel under fatigue loading conditions are shown below in Figures 4.11(a), (b) and (d). Figure 4.11(c), (f) and (g) show the striation-like marking on the fracture surface, cleaved slits, and cleavage fracture. Striation-like markings are produced by relative movement (plastic deformation) between the two fracture surfaces during cyclic loading.

The major interest in striations arises from the possibility that they can be used to assess the stress on the component during fatigue crack growth. While such marks are due to crack extension, likely associated with fatigue crack growth, the mechanism of formation of microvoids requires the presence of hard inclusions which plays a key role for crack propagation by means of ductile fracture.

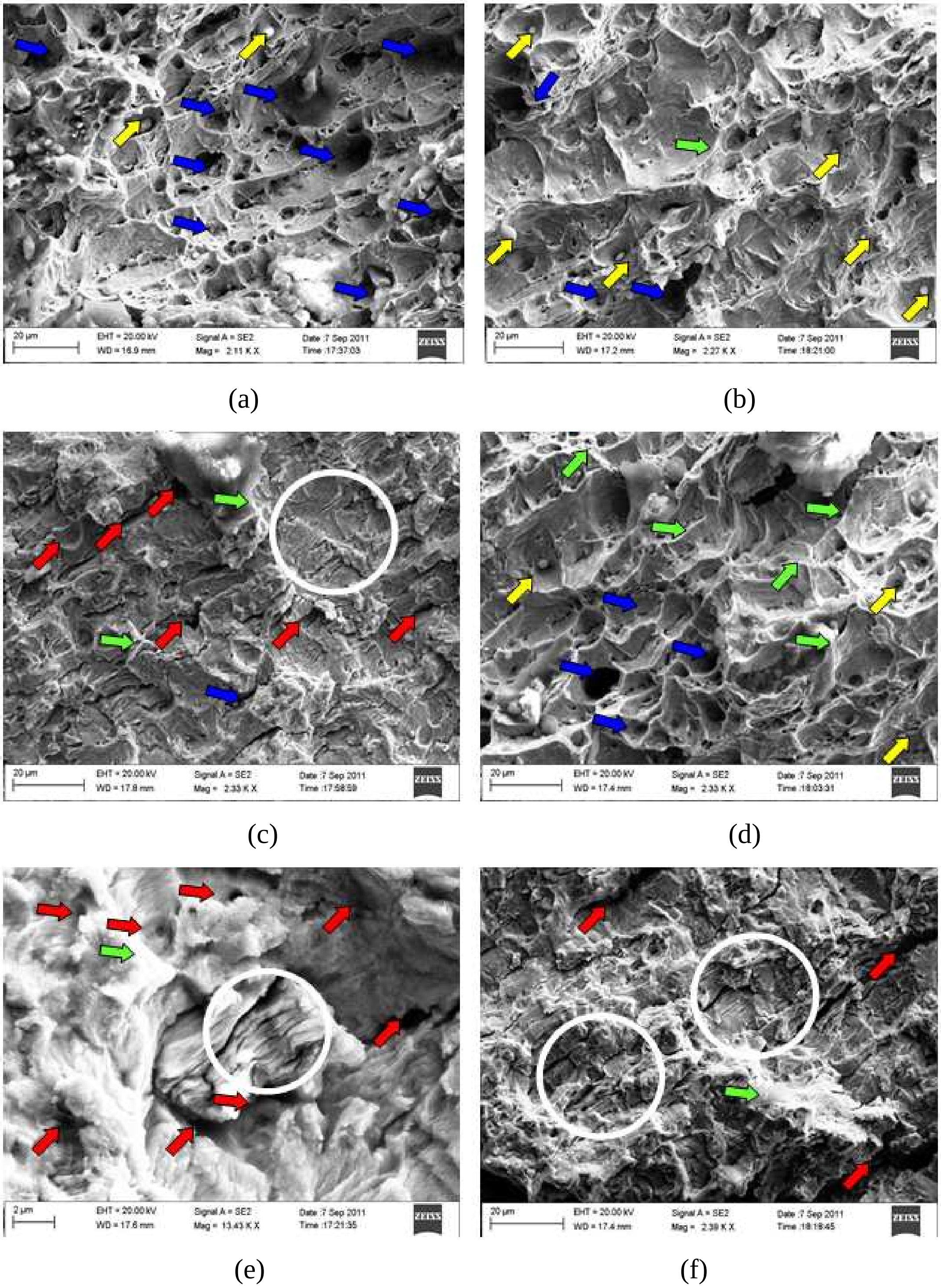
(a) (b)

(c) (d)

(e) (f)

Figure 4.11. Scanning electron micrographs: (a) sample 1; (b) sample 2; (c) sample 3; (d) sample 4; (e) sample 5; (f) sample 6. Legend: yellow arrow = inclusion; blue arrow = microvoid; green arrow = separation; red arrow = cleavage fracture; circle = striations.

As discussed earlier ductile fracture is normally trans-granular. The typical mode of ductile fracture is microvoid generation, and coalescence is the final stage in void controlled ductile fracture. Plasticity is localized between the voids. This localized deformation leads to final coalescence of voids which leads to complete failure. These three sequential steps for fracture by voids are and indicator of ductile fracture. Cleaved slits are also found on the cracked surface [Figure 4.11(c), (f) and (g)] which is an indicator of the cleavage feature of brittle fracture and hence both mechanisms are present in the middle and end stages of fatigue crack behavior. Therefore gradual transitions from ductile to mixed mechanisms occur. This observation indicates that a ductile failure mode is prominent as the crack grows trans-granularly through the material and, in contrast, brittle mechanisms are prominent as the crack extends by means of intergranular fracture.

Unlike cleavage fracture, which is a mechanism driven almost entirely by the local tensile stresses, hard inclusions [Figure 4.11(a), (b) and (d)] in the micro-regime play a prime role in ductile fracture in a continuum framework. The plastic strains for microcrack nucleation are small thereby causing only little damage in the material ahead of the internal crack formed in the neck region. More damage ahead of the crack in the final stages of microvoid coalescence carries only insignificant stresses and hence produce less energetic acoustic emission. However, the complex interplay of the key processes (microvoid nucleation, growth, and coalescence) leading to ductile failure underlies the need for additional consideration for improved understanding of the entire process.

Consequently, the kinetics of the (macroscopic) crack extension process during ductile fracture can be considered as driven primarily by the growth of microvoids. According to Ruggieri (2004), a process zone in the material layer enveloping the growing crack for the ductile fracture, must be thick enough to include at least a void to nucleate more microcrack. Hence void growth and coalescence in the fracture plane may cause the surface tractions in the process zone. Micrographs reveal a negligible degree of void growth in material at distances from the crack plane of more than 1-2 times the spacing of larger inclusions (i.e., in the material outside the planar layer) as indicated previously in Figure 4.1. SEM images [Figure 4.11(d), (e) and (f)] also show the highly tortuous (alternate sliding-off) localized path followed by the crack front. However macroscopic crack growth follows a simpler planar character.

According to equations (4.5) and (4.6), the fracture stress of a ferrite-ferrite interface is inversely related to the grain size, so the fine grain region represents a significant obstacle to an advancing crack. According to ASNT (2005) the ferrite grain size for steel is in the range of 11 µm. And a horizontal micro-crack in steel with a ferrite grain size of 10 µm, source speed of 1000 ms^{-1}, stress in material about to crack of 500 MPa, at a distance of 0.04 m from source to sensor can produce a vertical displacement of around 2.5×10^{-11}m having a time duration of (~10^{-5}m/103 ms^{-1}) 10 ns. Such a displacement signal is readily detectable under laboratory conditions even with narrow band transducers.

4.5 CONCLUSIONS

The objective of this work is to investigate and characterize the sources of acoustic emission signals in ductile steel parent material during fatigue crack growth. This was approached through b-value and fractographic analysis in an attempt to distinguish between AE events due to crack extension and other sources. The fractographic observations and b-value analysis of a compact tensile specimen made of ASTM A572 Grade 50 steel show that silent mechanisms such as microvoid coalescence are dominate in major portions of the fractured surface and contribute to generate large numbers of relatively small amplitude (around 50 dB) AE signals. Only a small fraction of the total crack surface is associated with highly emissive mechanisms such as transgranular or intergranular cleavage that may be considered as a key descriptor of emissivity in ASTM A572 Grade 50 steel. From the above discussion, the following conclusion can be drawn:

- b-value and fractographic analysis can provide indications of the mechanisms of AE during fatigue crack growth in steel bridge material and can aid in the assessment of the transition from ductile to ductile-brittle mechanisms.

- The early stage of fatigue crack growth in ASTM A572 Grade 50 steel is dominated by ductile mechanisms. With increasing stress intensity at the crack tip, brittle mechanisms (i.e. cleavage fracture) are also found in a small fraction of the total crack surface along with ductile mechanisms.

- Brittle fracture mechanisms produce relatively energetic acoustic emission events. In contrast, ductile fracture mechanisms produce relatively small amplitude acoustic emission hits. As stress intensity at the crack tip increases, intergranular cleavage fracture becomes more likely, resulting in relatively high amplitude AE.

- The logarithm of the number of hits is inversely proportional to AE amplitude. For high AE amplitudes, the regression analysis results in an approximate b-value of unity. This value reflects the brittle nature of the source mechanisms of AE events during middle stage II in the stable fatigue crack growth.
- Brittle fractures and hence the production of energetic acoustic emission events are relatively random phenomena and are related to number of different factors (i.e. ferrite grain contains initial defects on the crack path, fracture or cleavage stresses of a carbide-ferrite and ferrite-ferrite interfaces, ferrite grain sizes, effective surface energies of a carbide-ferrite and a ferrite-ferrite interface). Cleavage fractures frequently occur at higher strain rates during stable fatigue crack growth when other microcrack nucleation factors are available.

CHAPTER 5

ASSESSING ACOUSTIC EMISSION RELATED TO FATIGUE CRACK EXTENSION IN STEEL BRIDGE MATERIAL USING DIGITAL IMAGE CORRELATION

Over the past several decades acoustic emission (AE) has been studied for applications related to structural health monitoring (SHM) of metallic structures. The success of the AE technique for health prognosis of in-service steel bridges depends on reliable interpretation of the received AE signals. The emphasis of this chapter is on assessment and characterization of AE events associated with fatigue crack growth in ASTM A572 grade 50 steel which is widely utilized for steel bridge construction. The assessment of AE events associated with fatigue crack behavior was executed through monitoring the strain field near the crack tip using digital imaging correlation (DIC). Microscopic source characterization was aided by Scanning Electronic Microscopy (SEM). DIC offers the potential for providing real-time assessment of AE source mechanisms and associated AE hits, and therefore offers advantages over fractrographic analysis of SEM images. In contrast, fractographic analysis performed in several cluster areas in the fractured surface can provide an overall view of source mechanisms, but correlation between SEM and AE events cannot be established in real time.

Full-field strain measurement during fatigue crack extension was obtained using DIC and strain localizations were found along the slip bands near the crack tip. SEM results indicate that both ductile and brittle mechanisms are present in fatigue crack growth in the steel material. However, the fracture mechanisms are predominantly ductile in the early stage and cleavage fracture is found randomly in the middle and end stages. A key finding is that fatigue crack extension does not generally produce readily discernible AE events in the early stages, but AE events are found at the middle and end stages for the steel bridge material investigated. Throughout the test, AE is mainly associated with plastic deformation. For cleavage fracture, small plastic deformation is required and hence no strain redistribution is observed. At higher strain rates cleavage fractures are predominant, and these are theoretically linked to high amplitude AE events.

5.1 INTRODUCTION

The correlation of source mechanisms with AE data is important for prognosis of steel structures. Steel bridges are often subjected to fatigue loading and repeated load cycles greater than the fatigue limit may initiate micro-cracking in fatigue sensitive details (Carroll 2011, Elbert 1971, Ewing and Humfrey 1903). Each load cycle generates a plastic zone ahead of the crack tip. As the crack propagates, the initial plastic zone progressively expands forming an increasing plastically deformed area ahead of the crack tip. This process, which is shown schematically in Figure 5.1 (Carroll 2011), forms the basis for the subsequent plasticity-induced crack closure. Initially, many microcracks are formed in a random manner prior to the final growth of a crack (Hoshide and Socie 1988, Magnin et al. 1985, Ochi et al. 1985). Researchers have been attempting to relate fatigue crack growth to the characteristic microstructure of the damaged steel for decades following the early work of Laird (Laird and Smith 1963). Lankford and Davidson (Lankford and Davidson 1983) studied striations and crack growth rates in relation to crack closure, and Davidson (Davidson 1984) studied slip localizations at the crack tip. Certain aspects of crack propagation can be viewed as a result of localized plastic deformation near the crack tip in ductile materials.

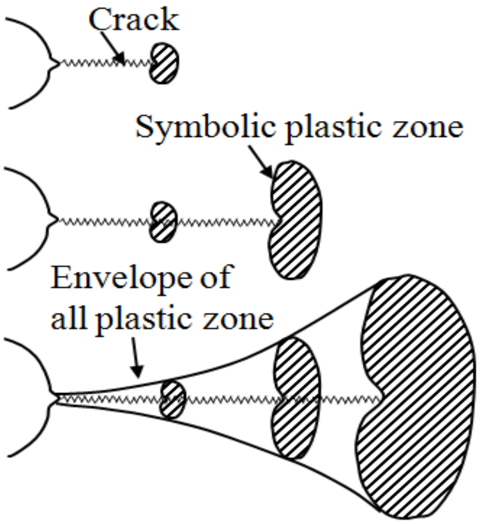

Figure 5.1. Envelope of plastic zones in ductile material during fatigue crack growth (after Carroll 2011).

The size of the plastic zone ahead of the crack tip increases with increasing load cycles under constant loading conditions. The strain field ahead of the crack tip suddenly redistributes and the released stress is partially manifested as transient elastic waves referred to as acoustic emission (ASNT 2005). Ductile fractures of steel are initiated by the nucleation and subsequent coalescence of micro-cracks (or voids) which form at second phase particles (see Table 5.1) (ASNT 2005, Hossain et al. 2013). In fatigue testing of a specimen with pre-cracking, voids may form at a preferred distance ahead of the crack tip due to the tri-axial stress field. For typical structural steels the site of micro-cracking is primarily around the inclusions (ASNT 2005, Hossain et al. 2013). Further increasing the strain in the plastic zone leads to ligament shearing which finally leads to macro-scopic crack extension.

The energy release during the formation of the plastic zone and the associated crack extension is a ductile mechanism which takes place over a comparatively longer period of time. This type of mechanism produces relatively low amplitude AE that is difficult to detect with conventional AE sensors (ASNT 2005). AE counts, N, have been reported to be proportional to the m-th power of the stress intensity factor ($N \alpha K^m$) (ASNT 2005, Davidson 1984). A typical value of m is 4 and the AE source is distributed not only on the main fracture plane but also within a small volume ahead of the crack tip referred to as the plastic zone (ASNT 2005). In contrast, cleavage fracture entails release of energy over a relatively short period of time. This type of mechanism produces higher amplitude AE signals that are readily detectable with conventional AE sensors (ASNT 2005, Hossain et al. 2013).

The relationship between the strain fields near the crack tip has been recognized as an important one (Carroll 2011, Chauvot and Sester 2000, Davidson 1984, El Bartali et al. 2008, Elbert 1971, Jonnalagadda et al. 2010, Laird and Smith 1963, Lambros and Patel 2011, Lankford and Davidson 1983, Peralta et al. 2007) to understand micro-level fatigue crack extension. While extensive research has been conducted in relation to fatigue crack growth (Carroll 2011, Davidson 1984, El Bartali et al. 2008, Elbert 1971, Ewing and Humfrey 1903, Hoshide and Socie 1988, Laird and Smith 1963, Lankford and Davidson 1983, Magnin et al. 1985, Ochi et al. 1985, Peralta et al. 2007), at present no consensus exists regarding the mechanisms that cause the associated AE in steel bridge materials.

In this paper, time synchronization of AE data with Digital Image Correlation (DIC) measurements is carried out to examine the source mechanisms associated with AE activity.

5.2 FATIGUE CRACK GROWTH

Fatigue crack behavior can be divided into five stages (Carroll 2011): (1) microstructural changes due to plastic deformation leading to permanent damage accumulation, (2) microcrack nucleation, (3) microcrack growth and coalescence into a dominant crack, (4) growth of the dominant fatigue crack, and (5) final fracture. Structural components subjected to high cycle fatigue (*i.e.*, low stress and lifetimes more than 10,000 cycles) are dominated by microcrack nucleation in stage I with relatively little time spent in the other two stages (II and III). In low cycle fatigue (*i.e.*, high stress and lifetimes of 10,000 cycles or less), many microcracks nucleate in the early cycles, but most of the fatigue life is spent linking microcracks to form a dominant crack. Fatigue crack growth analysis is used when a significant portion of the lifetime is spent growing a single crack to failure. Because the focus of this work is fatigue crack growth, notched specimens with pre-cracking in compression were used so that a dominant fatigue crack initiated early with minimum residual stress.

Fatigue crack growth is divided into three stages. Stage I refers to low speed cracking near the threshold. In this stage, fatigue crack growth typically occurs when cracks are microstructurally short and is characterized by a crack tip plastic zone size that is smaller than the grain size. In stage I, fatigue cracks follow slip systems within grains changing direction at grain boundaries. Stage II refers to stable crack growth, and is sometimes referred to as the Paris regime. Once the crack has grown through several grains, its associated plastic zone covers multiple grains, and it is said to be in stage II crack growth. The fatigue crack path in stage II is dominated by global loading conditions that cause the crack to generally grow perpendicular to the direction of maximum principal stress. Although stage II fatigue crack growth is often thought of as independent of microstructure, the crack path still changes direction according to microstructural parameters. The interplay between global crack driving forces and microstructural effects on the crack path in stage II and the resulting acoustic emission are the focus of this study. Stage III is associated with unstable fatigue crack growth.

Fatigue crack growth in metals occurs by the repeated blunting and shear deformation process shown schematically in Figure 5.2 (Laird and Smith 1963). According to Laird and Smith (1963), as a cracked specimen is loaded the material at the crack tip yields in shear deformation at the crack tip resulting in crack tip blunting. Unloading subsequently results in a sharpening of the crack as the elastic material surrounding the crack tip region forces the crack closed once again. Although this basic fatigue crack growth mechanism does not explicitly consider the effects of microstructure, the concept can be used to qualitatively explain many of the features seen in experimental observations of fatigue crack growth. At the first instance, this can be thought of as the collective response of two or more grains in the vicinity of the crack tip. Interaction at this scale would include the effects of grain boundaries in the evolution of plastic deformation in fatigue. The grain boundaries may act either as deformation initiators, or as deformation inhibitors depending upon the type of boundary and/or the local loading conditions.

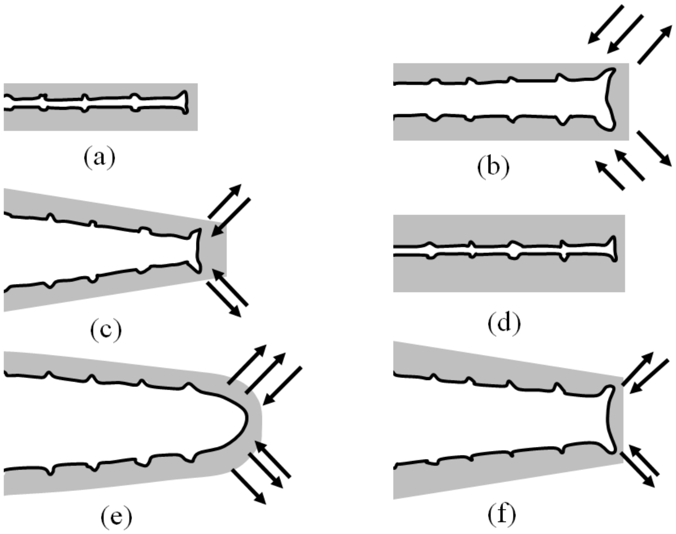

Figure 5.2. Mechanism of fatigue crack propagation proposed by Laird in 1963 (after Laird and Smith 1963) (a) unloading, (b) increasing tension, (c) peak load, (d) unloading, (e) unloaded, (f) increasing load on the subsequent cycle (after Carroll 2011).

5.3 STRAIN MEASUREMENTS IN FATIGUE CRACK GROWTH

Despite extensive study of fatigue cracking, published measurements of full-field strains associated with fatigue crack growth are relatively limited. One of the earliest measurements of the strain field near a fatigue crack was made by Morris et al. (1985). The authors computed strains by manually comparing optical micrographs in a rudimentary form of digital image correlation. These low-resolution strain fields were used to examine the shape of the plastically deformed material on the surface containing the crack tip.

Recently Carroll (2011) studied crack nucleation and fatigue growth rates in relation to microstructure at the crack tip with measurements of strain fields. Previously Peralta et al. (2007) studied full-field measurements of strain fields in fatigue crack growth. However, in their work, there was little consideration of microstructure and no consideration of acoustic emission monitoring. These researchers measured the strain field around crack tips for several specimens and found strain localizations in lobes along slip bands ahead of the crack tip.

5.4 DIGITAL IMAGE CORRELATION (DIC)

DIC is a technique for measuring full-field displacements by comparing an image of a deformed specimen surface with a speckle pattern () to a reference image at an earlier state (Figure 5.3). More information can be found in Sutton et al. (1983, 1999, 2009). At the micro-scale, sub-grain level deformation can be captured (Sutton et al. 2009) and eventually strain fields near the crack tip can be obtained. DIC can also be effective for nanoscale measurements (Carroll 2011, Sutton et al. 1999). DIC is typically implemented by matching image subsets having sizes that range from 21×21 px to 101×101 px depending on the quality of the speckle pattern (Carroll 2011, Sutton et al. 2009, Sutton et al. 1983, Sutton et al. 1999).

In addition to plastic deformation and crack extension, AE sensors are also sensitive to other noise, which is primarily generated from grating between the fracture surfaces and abrasion within the load train. Grating emission occurs mainly during reverse cycling. To minimize grating emission, AE collected below 80% of the maximum load was eliminated from the dataset (Hossain et al. 2013, Yu et al. 2011). Based on the characteristics of the waveforms, duration-amplitude filters similar to the Swansong II (Fowler et al. 1989) for a threshold equal to 45 dB were employed to minimize mechanical noise in the AE dataset.

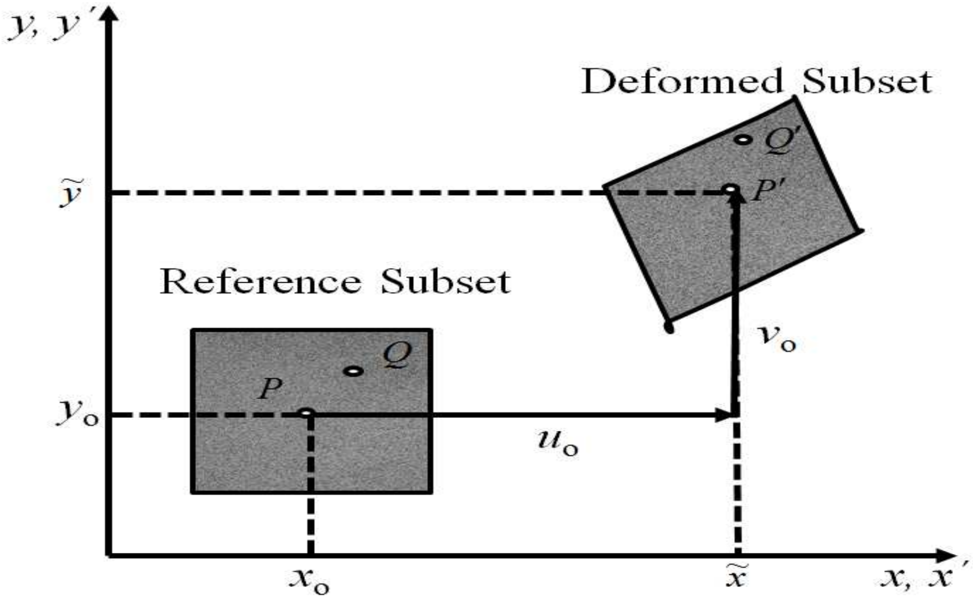

Figure 5.3. Subsets are mapped to their deformed locations to determine the displacement at each correlation point (after Carroll 2011).

For this study, a compact tension specimen was polished and a speckle pattern was created by spraying black and white paint. High-resolution images were acquired with a five Mega-pixel Point-Gray camera and a macro lens (NIKKOR-50 mm F/1.4G AF-S) (Figure 5.4). The camera was triggered to acquire images at a rate of 5 frames per second using the software Vic-Snap 2010 (Correlated Solutions). The distance of the camera from the measurement area was approximately 760 mm (30 in). The area of the speckle pattern was 146 mm × 120 mm (5.7 inch × 4.73 inch). The size of the measurement area was 73 mm × 65 mm (2.9 inch × 4.73 inch) along the x-axis and y-axis, respectively. The average highest-level value of noise at zero displacement was approximately ± 0.023 percent (an average noise level was calculated based on 10 data sets collected at zero displacement). The selection of subset size and step for a better correlation is important for DIC and the default subset of 21 and step of 5 were used for this study. The distance between the boundaries of the measurement area and the boundaries of the speckle pattern, which are well known to be the areas more prone to noise in DIC measurements, was in the range of 10 mm (0.4 inch) to 30 mm (1.2 inch) along the y-axis and 8 mm (0.3 inch) to 50.8 mm (2 inch) along the x-axis. The average strain field along the y-axis was extracted using inspector tools (a circular strain monitoring area was used) and plotted over time. The strain monitoring inspection circle was placed at the crack tip in different locations and the whole process was repeated several times. In most cases no significant relative strain variations were observed. Further information is discussed in the following sections.

5.5 CT SPECIMEN TESTING AND AE MONITORING

A compact tension (CT2) specimen of ASTM A572 Grade 50 structural steel was utilized for AE monitoring during constant amplitude cyclic loading. The chemical composition of the steel is shown in Table 5.1. The effective width of the CT specimen was 241 mm (9.5 inch), and the thickness was 12.7 mm (0.5 inch), with an initial crack (notch) length of 82.6 mm (3.25 inch) (Figure 5.4). A clip gage and a microscopic video camera were used to monitor crack propagation. The maximum applied load was 65 kN (14.6 kips) with a load ratio (R) of 0.1 at a frequency of 2 Hz. Two R15I-AST AE sensors and six wideband (WDI) sensors were used as shown in Figure 5.4 (a). Epoxy and tape were used to secure the sensors on the steel surface. All AE sensors had internal pre-amplification of 40 dB. The test amplitude threshold was set to 45 dB and signals were stored and displayed with a DiSP unit (Mistras Group, Inc.).

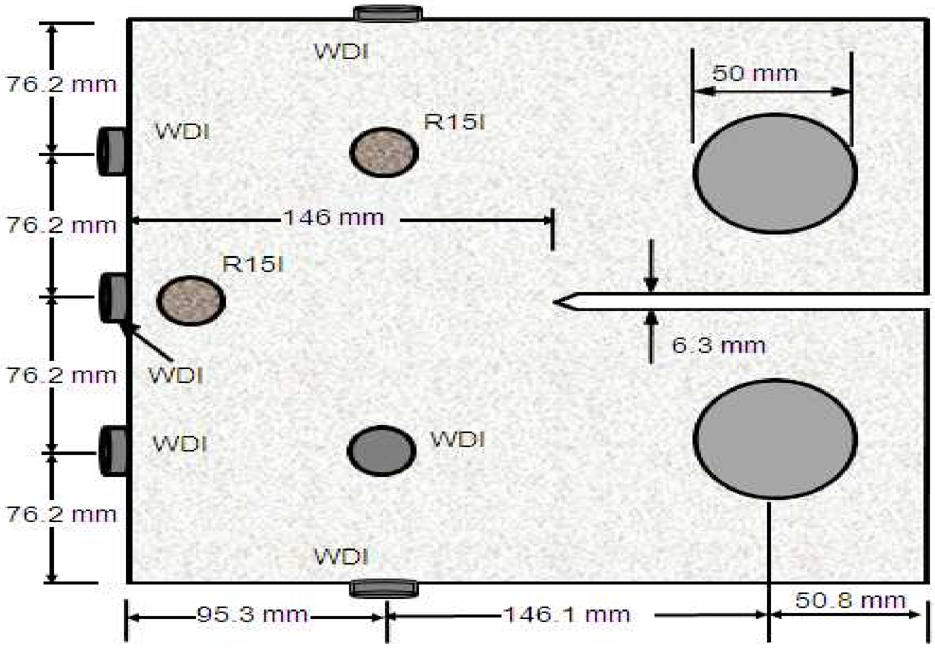

(a) schematic

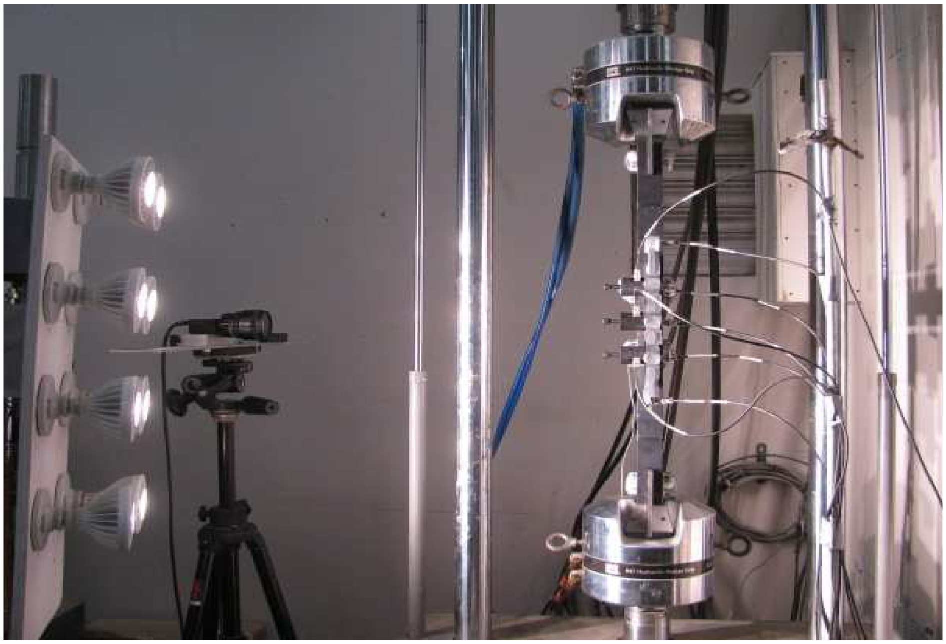

(b) photograph during testing with DIC setup

Figure 5.4. Compact tension (CT) specimen.

Table 5.1. Chemical Properties of Steel.

Element	**Weight %**
Iron (Fe)	Base metal
Manganese (Mn)	1.35 (max)
Silicon (Si)	0.30 (max)
Carbon (C)	0.23 (max)
Copper (Cu)	0.20 (min)
Sulfur (S)	0.05
Phosphorus (P)	0.04

5.6 Results and Discussion

Strain Fields:

Specimens were cycled by sine-wave loading at 2-Hz in an MTS machine. Periodically, at maximum load as shown in Figure 5.5, a picture was captured with a NIKKOR-50mm F/1.4G AF-S lens triggered by computer using Vic-snap 2009 software (Correlated Solutions). For this study, changing of the strain field near the crack was examined to monitor the cracking phenomena. The DIC technique presented here is far more powerful than simple imaging of the raw pictures.

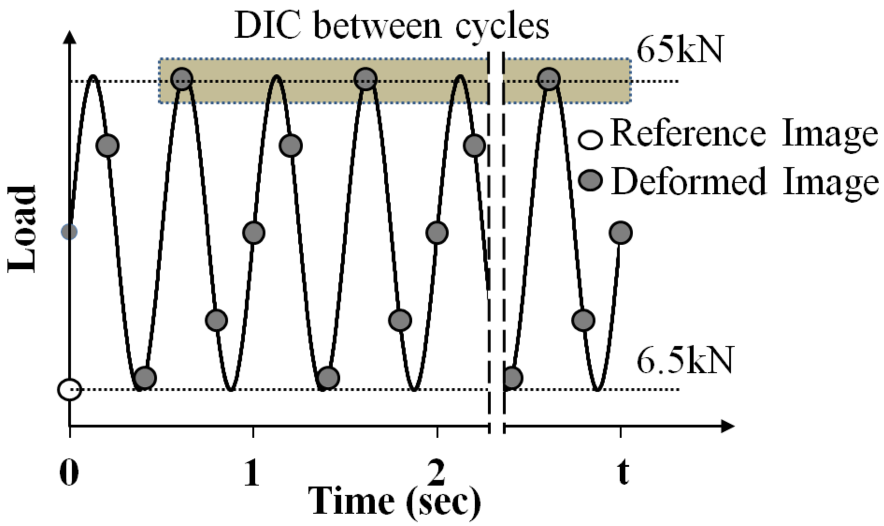

Figure 5.5. Schematic of DIC image acquisition steps between fatigue cycles.

Post-processing was performed using Vic-2D 2009 software (Correlated Solutions). Figure 5.5 shows the schematic of DIC image acquisition steps between fatigue cycles. The process for analyzing the strain field near the crack tip relies on a series of images of the deformed specimen during cyclic loading as summarized in Figures 5.6 through 5.9. These figures are presented with stress intensity range on the horizontal axis, where the stress intensity range is related to crack growth behavior as follows:

- Early stage II: Stress intensity range (ΔK) between 57 MPa√m (51.9 ksi√in) (corresponding to the initial crack length) to 60 MPa√m (54.6 ksi√in).
- Mid stage II: Stress intensity range (ΔK) between 60 (54.6 ksi√in) to 95 MPa√m (81.9 ksi√in).
- Late stage II: ΔK is in the range of 95 (81.9 ksi√in) to 128 MPa√m (116.5 ksi√in) near the critical level fatigue crack where the fatigue crack is much faster than calculated using the Paris equation.
- Stage III: Stress intensity range (ΔK) is greater 128 MPa√m (116.5 ksi√in) to the end of the test, critical level fatigue cracking where crack grows much faster than the Paris regime.

DIC is performed between load cycles to describe the accumulation of plastic strain that was used to investigate the accumulation of fatigue damage and microlevel crack extension. The black region on the left side of the representative DIC strain contours in Figures 5.6 through 5.9 show the initial V-notch from which the fatigue crack originates. The contours shown in Figures 5.6 through 5.9 are DIC measurements of the

ε_{yy} strain field (i.e., perpendicular to the x direction) that describes a formed plastic zone [red area in Figure 5.6(a)] and a rapid decrease in local strain during cyclic loading. The crack tip is indicated by the blank mark.

Figure 5.6(a) shows the average strain during the fourth cycle at the peak load. The maximum strain recorded was 0.89 ± 0.023 %. The deformed images within the shaded area are captured at the same level of cyclic load, so it is reasonable to compare the average measured strain within the same circular area, which can provide insight into the cracking phenomena at the microlevel.

Fatigue strain accumulated in each cycle during the formation of the plastic zone and the measured maximum strain was 1.13 ± 0.023 % at stress intensity range of 59.21 MPa√m (53.88 ksi√in) [Figure 5.6(b)]. Accumulated strain at the crack tip causes a sudden crack extension that is accompanied by a redistribution of stress near the crack tip and peak strain as shown in Figures 5.6(c) and (d). Figure 5.6(d) shows the change of maximum strain around -0.16% between 59.21 MPa√m (53.88 ksi√in) and 59.22 MPa√m (53.89 ksi√in), which clearly indicates the microlevel crack extension and hence a sudden drop in strain.

In Figures 5.6, the strain field indicates that several strain localizations occured in early stage II– primarily starting at grain boundaries but also appearing as strain accumulation along specific slip systems – before the crack even enters the region. Even more interesting is that in Late Stage II, measurable strain redistribution are visible as shown in Figure5.7 primarily in the form of strain field dropping. The evolution of strain fields in Figure 5.8 and 5.9 show that many areas start accumulating strain long before the crack reaches the region of interest (i.e., ahead of the high strain lobes at the crack tip). As the crack tip approaches each region, other strain localizations form, but the earliest slip band localizations intensify and most become the sites where some of the highest strains in the region are observed.

This sequence of events is apparent in Figures 5.6 through 5.9. The phenomenon is repeatedly observed throughout the crack propagation.The strain fields also show that plastic strain accumulation occurs when the two lobes emanating from the crack tip reach the point of interest. The material directly ahead of the crack tip is relatively unstrained until the crack tip passes through it. A good examples of this is in Figures 5.6 through 5.8. Crack tip locations (the same ones displayed in Figures 5.7, 5.8 and 5.9) were identified in the deformed images as demonstrated in Figure5.6 on DIC images within inspection region. These inspection locations were then transformed to the desired locations and the average strain field at each image was calculated.

In Figures 5.7 through 5.9, ε_{yy} strain fields at different stress intensity range are shown for mid stage II, late stage II to stage III, and late Stage III, respectively. These six strain fileds in each figure, at the stress intensity range (ΔK) indicated; provide an accurate indication of strain evolution with crack location. When the crack crosses the region of observation, the crack line (black line) with a white circle indicating the crack tip (Figures 5.7 and 5.8), the inspection circle is replaced to the new observation point at the crack tip to monitor the local strain field and thereby monitor the microlevel fatigue crack extension.

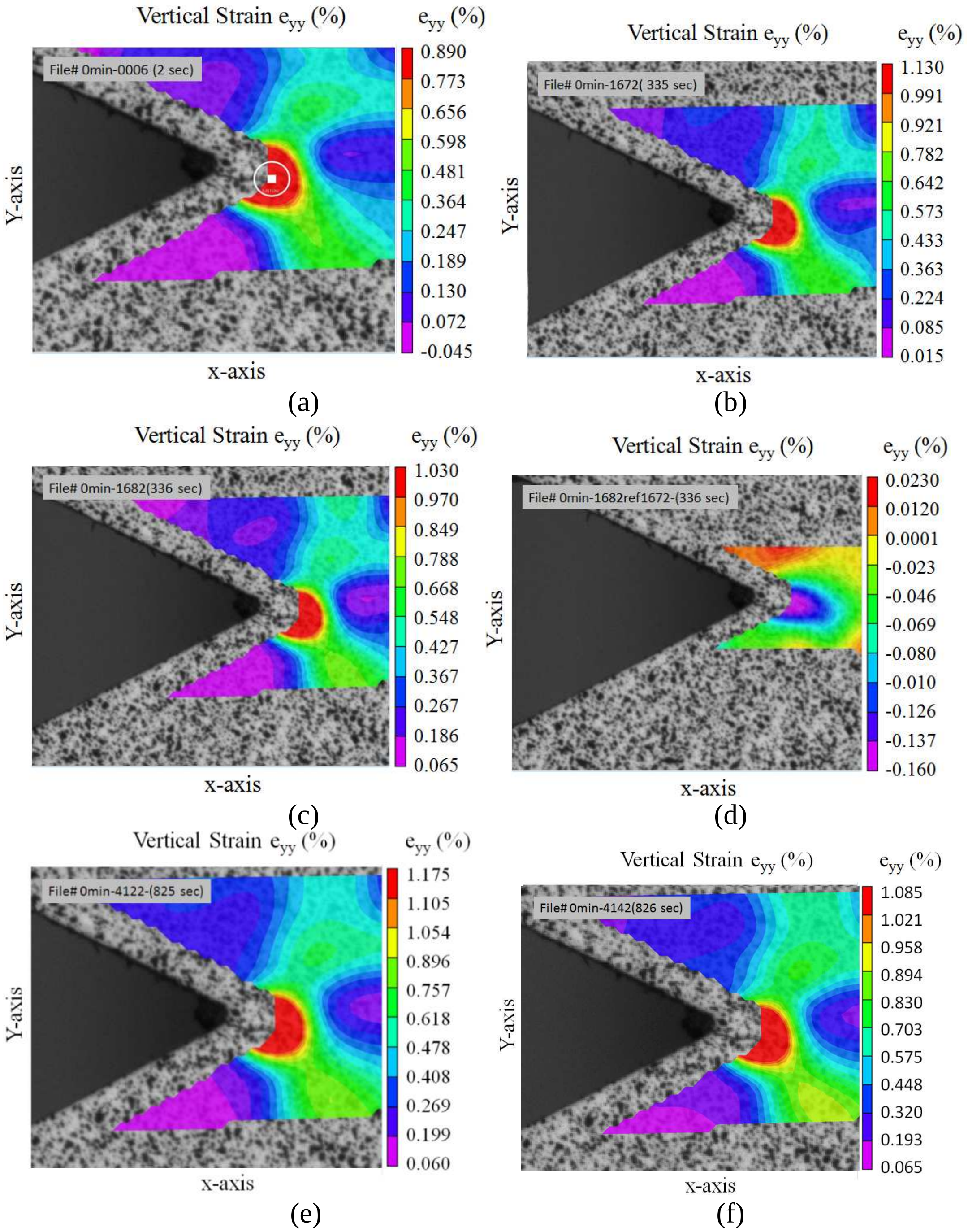

(a) (b)

(c) (d)

(e) (f)

Figure 5.6. Strain fields, εyy – (Early to Mid Stage II): (a) DIC performed at 56.94 MPa√m (51.82 ksi√in); (b) DIC performed at 59.21 MPa√m (53.88 ksi√in); (c) DIC performed at 59.22 MPa√m (53.89 ksi√in); (d) Strain drop between 59.21 MPa√m (53.88 ksi√in) and 59.22 MPa√m (53.89 ksi√in); (e) DIC performed at 61.54 MPa√m (56.00 ksi√in); (f) DIC performed at 61.55 MPa√m (56.01 ksi√in).

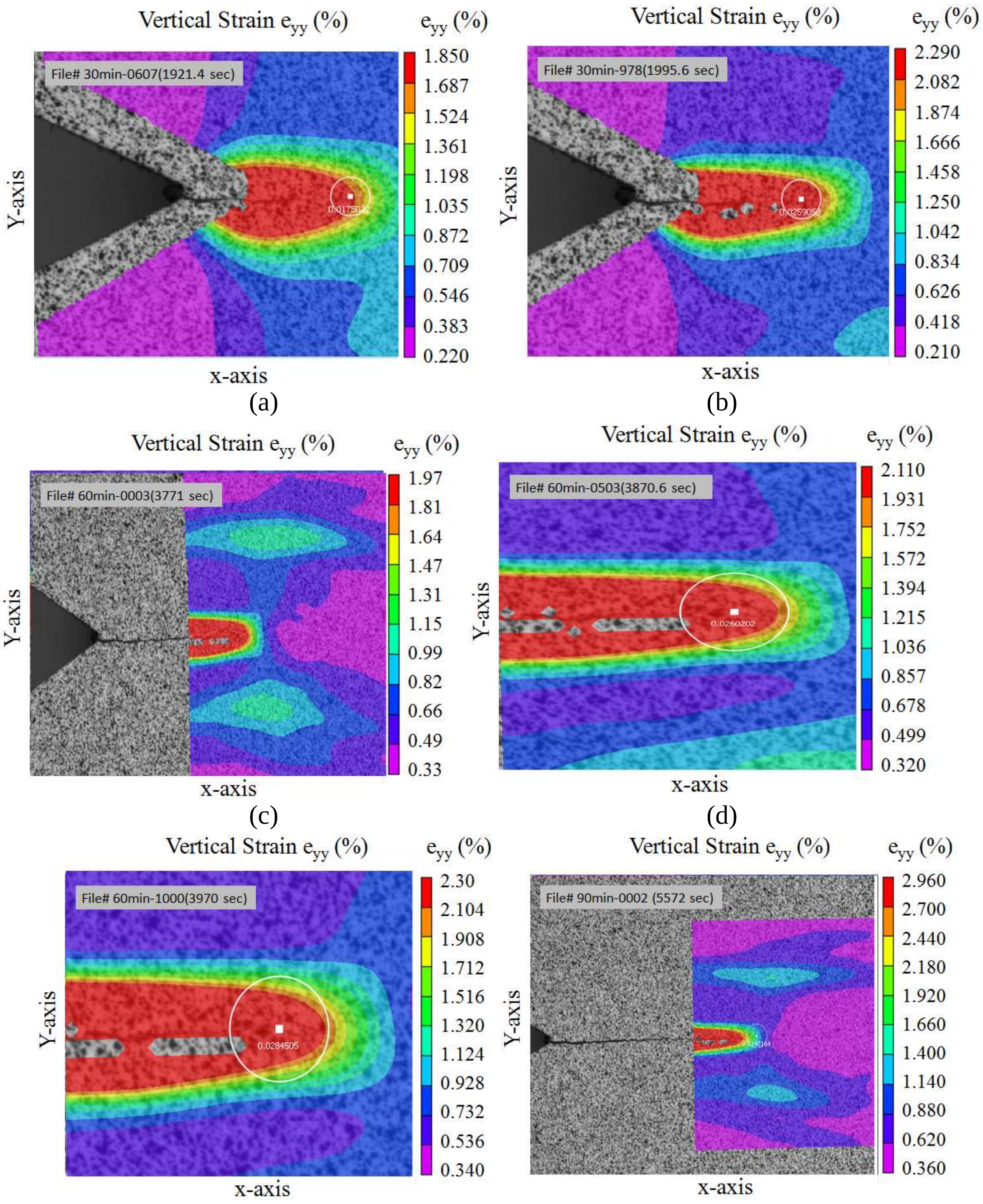

(a) (b)

(c) (d)

(e) (f)

Figure 5.7. Strain fields, ε_{yy} – (Mid Stage II): (a) DIC performed at 66.25 MPa√m (60.29 ksi√in); (b) DIC performed at 66.62 MPa√m (60.63 ksi√in); (c) DIC performed at 76.06 MPa√m (69.22 ksi√in); (d) DIC performed at 76.61 MPa√m (69.72 ksi√in); (e) DIC performed at 77.17 MPa√m (70.23 ksi√in); (f) DIC performed at 88.26 MPa√m (80.32 ksi√in)

Figure 5.7 provides the average strain fileds at Mid Stage II [60 (54.6 ksi√in) to 95 MPa√m (81.9 ksi√in)]. The maximum accumulated strain field recorded was 1.85 ± 0.023 % as shown in Figure 5.7(a) at stress instensity range 66.25 MPa√m (60.29 ksi√in) to 2.96 ± 0.023 % as shown in Figure 5.7(f) at the end of mid stage II [88.26 MPa√m (80.32 ksi√in)]. Therefore, DIC provides grain level measurements of the strain fields and how they developes as the crack grow through the CT specimen in addition to crack tip location. These strain field measurements linked to the microstructure with scanning electron microscope (SEM), eventually provides insight of the fatigue crack growth mechanisms at microlevel. After ending the fatigue test, SEM analysis was perfprmed and that gives visual confirmation of the slip bands seen in the DIC measurements and a clearer picture of the crack path in relation to the microstructure, finally, images of the fracture surface give limited but useful glimpse of fracture mechanisms within the interior of the specimen and will be discussed in the following section.

Figure 5.8 shows the average strain fileds at Late Stage II to Stage III [95.77 MPa√m (87.16 ksi√in) to 147.58 MPa√m (134.30 ksi√in)]. The maximum accumulated strain field recorded was 5.4 ± 0.023 % as shown in Figure 5.8 (a) at stress instensity range 95.77 MPa√m (87.16 ksi√in) and 2.98 ± 0.023 % as shown in Figure 5.8 (b) at 105.53 MPa√m (96.04 ksi√in), therefore strain redistribution occured at the crack tip [Figure 5.8 (a) and (b)]. Strain accumulation that indicate the microcrack extension. Results show that some plastic strains accumulate ahead of the crack tip, but most strain localization occurs when the crack tip pass through the material. In the area directly ahead of the crack tip, between the crack tips, there is relatively little strain as shown in Figures 5.6-5.9 until the crack tip passes.

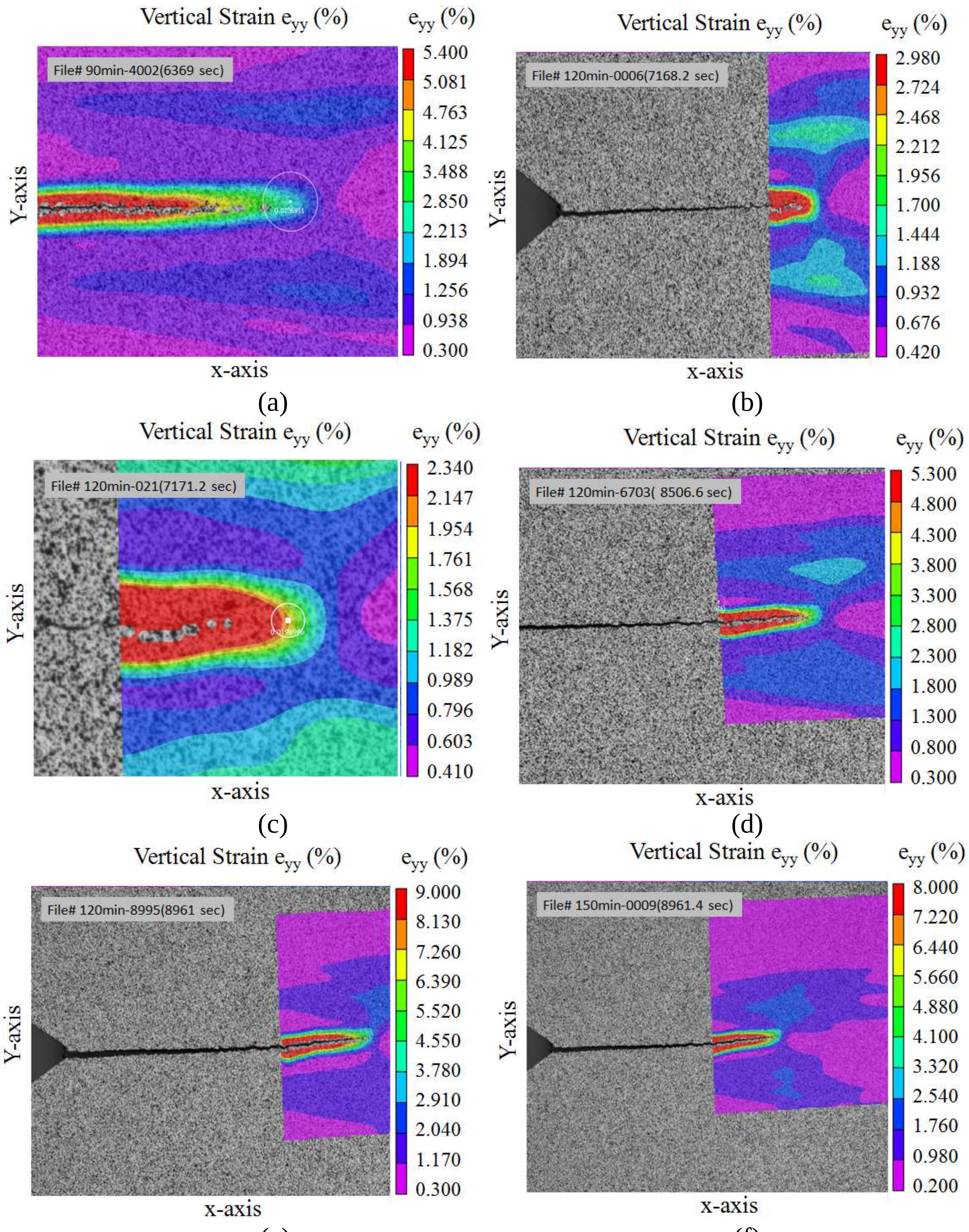

Figure 5.8. Strain fields, ε_{yy} – (Late Stage II to Stage III): (a) DIC performed at 95.77 MPa√m (87.16 ksi√in); (b) DIC performed at 105.53 MPa√m (96.04 ksi√in); (c) DIC performed at 105.58 MPa√m (96.08 ksi√in); (d) DIC performed at 133.37 MPa√m (121.37 ksi√in); (e) DIC performed at 147.56 MPa√m (134.29 ksi√in); (f) DIC performed at 147.58 MPa√m (134.30 ksi√in).

The strain value 2.34 ± 0.023 % as shown in Figure 5.8 (c) at 105.58 MPa√m (96.08 ksi√in) is increased to 5.30 ± 0.023 % as shown in Figure 5.8 (d) at 133.37 MPa√m (121.37 ksi√in). Strain accumulation, localization and redistribution within the plastic zone of the fatigue crack has a complex dependency on several factors including stress intensity range (driving force for the fatigue crack growth), position with relation to the crack line, crack direction, grain geometry and orientation, and sub-surface grains. Further strain accumulation is observed and the maximum strain field increased to 9.0 ± 0.023 % as shown in Figure 5.8 (e) at 147.56 MPa√m (134.29 ksi√in); and finally strain field is droppedto 8.0 ± 0.023 % as shown in Figure 5.8 (d) at 147.58 MPa√m (134.30 ksi√in). At higher stress intensity range, crack growth is in a transgranular fashion, most frequently following slip bands. These phenomena can be found in Figures 5.6 though 5.9. DIC images as shown in Figures 5.9 (a) through (f) provide the average strain fileds at the crack at late Stage III [164.79 MPa√m (149.97 ksi√in) to 203.63 MPa√m (185.31 ksi√in) The average strain field recored at 178.33 MPa√m (162.29 ksi√in) was 17.50± 0.023 % and then strain field result as shown in Figure 5.9 (b) that was obtained at 192.66 MPa√m (175.33 ksi√in); which shows the average strain value was 49.50 ± 0.023 % at crack tip Therefore microstructure of the grain and stress intensity range are the complex dependency factor on crack growth. The microstructural effects are evident in the form of generating microcracks and frequent changes the main crack direction. Ultimately, the crack path depends on a number of factors including the local stress field, the global crack driving force, and local microstructural inhomogeneities. The strain field gradually increased at Late Stage III as shown in Figures 5.9.

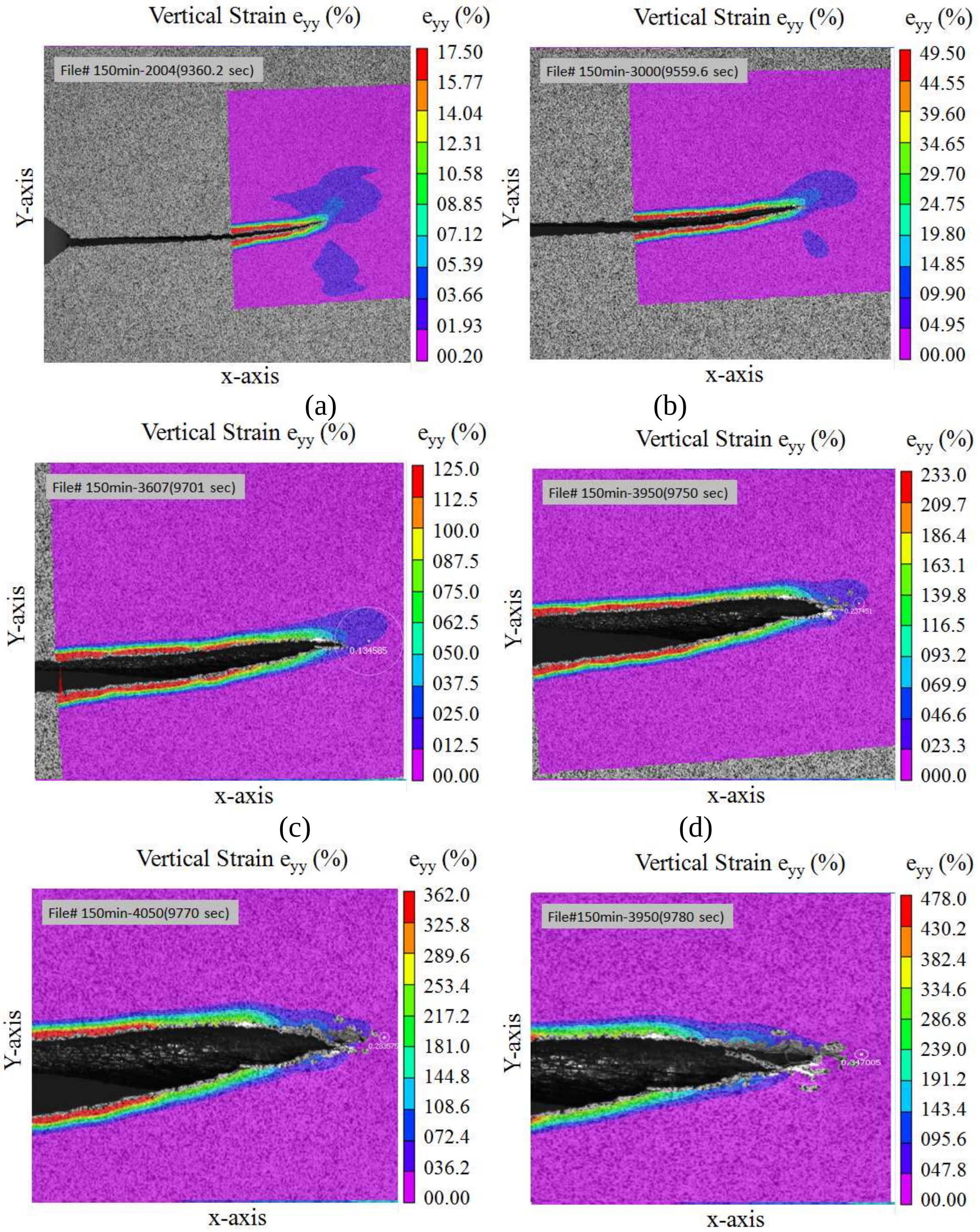

(a) (b) (c) (d) (e) (f)

Figure 5.9. Strain fields, ε_{yy} – (Late Stage III): (a) DIC performed at 164.79 MPa√m (149.97 ksi√in); (b) DIC performed at 178.33 MPa√m (162.29 ksi√in); (c) DIC performed at 192.66 MPa√m (175.33 ksi√in); (d) DIC performed at 199.14 MPa√m (178.11 ksi√in); (e) DIC performed at 202.08 MPa√m (183.91 ksi√in); (f) DIC performed at 203.63 MPa√m (185.31 ksi√in).

The average strain field at stress intensity range of 199.14 MPa√m (178.11 ksi√in) was 233 ± 0.023 % (Figure 5.9(d); at 202.08 MPa√m (183.91 ksi√in) and 203.63 MPa√m (185.31 ksi√in), it was 362 ± 0.023 % and 478 ± 0.023 %, respectively. No strain redistribution is observed in Stage III. Crack extention is namely transgranular or intergranular.

The above discussion, it can be summarized that in early stage II the ε_{yy} strain fields is nearly linear with a relatively static crack and the stress intensity range is almost constant. The deviations from linearity in ε_{yy} strain field are primarily due to microstructural effects, but there may be some amount of crack tip identification error present as well to calculate the average strain (ε_{yy} strain field) at the crack tip. As the crack grows through the microstructure, the crack growth rate varied due to changes in crack direction and varying resistance of the microstructure to crack growth with location and stress level. Therefore, subsequent DIC images are capable of inspecting grain level crack extension and the movement of the crack tip can be identified with high accuracy to make conclusions about crack growth extensions at the grain level.

Synchronization of AE and DIC Data:

AE above 45 dB was continuously recorded and the cracking phenomenon was monitored using a clip gage and DIC to correlate AE hits and events associated with fatigue crack growth. The total number of AE events and hits recorded throughout the test was 33,777 and 150,615 respectively as shown in Figure 5.10(a). The term 'hit' refers to the detection and measurement of an AE signal on any individual channel and the term 'event' refers hits of 3 or more sensors within a particular period of time. Based on the characteristics of the waveform of AE hits, Swansong II filter and 80 % of the peak load filters are applied. Swansong filter is based on the amplitude and durations of the AE hits. Mechanical noises have higher duration and relatively low amplitude. AE hits. Details of the Swangsong II filter and load filter may be found in article of Yu et at. (2011). the idea for load filter is fatigue crack extents during cycling loading only during opening of the crack. Previous study showed the crack extends above the 80 % (52 kN) of the peak load (65 kN). After filtering, the number of hits was reduced to 107,642 [Figure 5.10(b)], which is approximately 70% of the total hits. A previous study has shown that less than 1% of the total hits during fatigue testing may be potentially associated with fatigue crack extension (Hossain et al. 2012), where as the remaining singals may be associated with mechanical noise in the loading train, reflections, and grating emissions.

To minimize acoustic emission associated with reflections the hit lockout feature was used. The hit lockout value is a length of time or distance, which controls the interval between consecutive hits. The hit lockout value used in this test was 40 micro-seconds. This hit lockout time was calculated based on the specimen dimension and wave speed. Calculated average wave speed was 5,770,000 mm (227,000 inch) per second and the wave travels a distance of 231 mm (9.10 inch) during a 40 micro-second period. The distance between the crack tip and the edge of the specimen is in the range of 114 mm (4.49 inch) to 146 mm (5.75 inch). Any energy release at the crack tip will travel as elastic waves and hits the sensors directly and part of the wave reflected at the edge of the specimen, and come back toward the sensors. For example, any crack extension may produce an elastic wave, travel through the medium, hits sensor 3 directly (shortest distance from crack tip) and top (face where sensor 5 is attached) or bottom edge (face where sensor 1 is attached), as shown in Figure 5.4, simultaneously. Depending on the energy of the incident wave, part of the incident energy may reflect from the edge, travel toward and hit sensor 3. Therefore the time difference between these two successive hits is in the range of 13 (3 inch/227,000 inch/sec) to 33 (7.5/227,000 inch/sec) micro-seconds. Hence after receiving the direct hit, the sensor will lock out and will not receive any hit when the time difference between two successive hits is less than 40 micro-seconds.

AE data was plotted against the stress intensity range [Figures 5.10(c), (d), (e)]. The stress intensity was calculated based on the ASTM 2006 emperical expression (ASTM, 2006). A clip gage was used to record the Crack Mouth Opening Displacement (CMOD), ‘d’ and then the ASTM (2006) empirical expression was used to calculate the crack length, ‘a’ (from the center of the loading line) which in turn is used to calculate the stress intensity range.

AE data was plotted against the load data. In most cases AE events were recorded during crack closure and high amplitude AE events which may generate reflections were not present immediately before these events. Though the dataset has been filtered to exclude hits below 80 % of peak load, these AE events may still be due to friction between the fracture surfaces as shown in Figures 5.6 through 5.9. The other potential source can be mechanical noise from the loading pins.

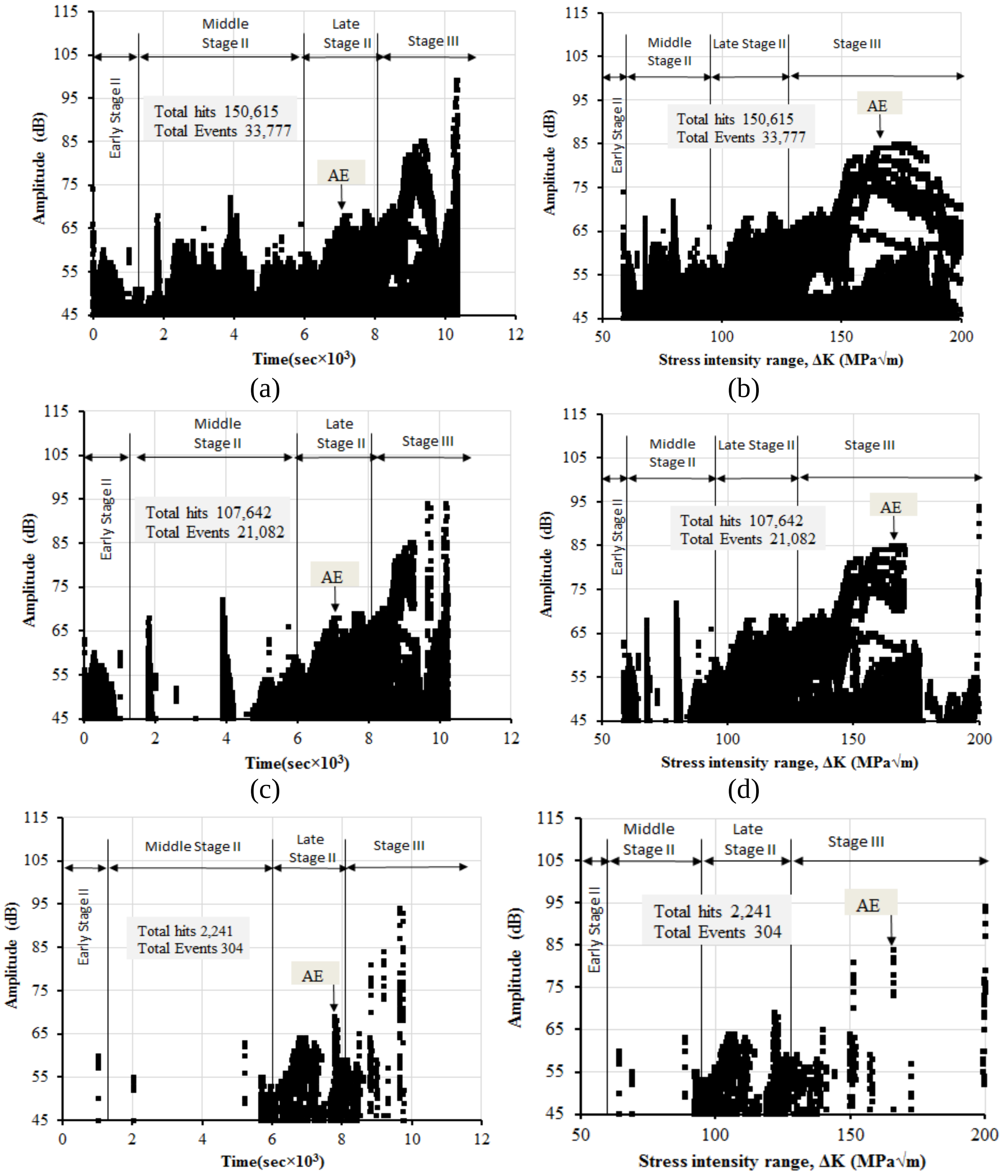

(a) (b)

(c) (d)

(e) (f)

Figure 5.10. Amplitude distribution: (a) hit amplitude vs time without filter (full-data); (b) hit amplitude vs time after eliminating below 80% of the peak load and applying Swansong II filter; (c) hit amplitude vs stress intensity range without filter (full-data); (d) hit amplitude vs stress intensity range after eliminating below 80% load of the peak load and applying Swansong II filter; (e) hit amplitude vs time after eliminating below 80% of the peak load and applying Swansong II filter along with a source location based filter (f) hit amplitude vs stress intensity range after eliminating below 80% load of the peak load and applying Swansong II filter along with a source location based filter.

To minimize this noise, source location filtering (SLF) was employed. Only the events near the crack tip were extracted by using MATLAB code based on the source sensor distance and the sequence of the arrival time of the waveforms. The basic idea is that the closest sensors are triggered by the waveform first and vice-versa. After employing the SLF technique, the remaining hits and AE events are 2,241 and 334, respectively [Figure 5.10(e)].

The source location based filtering technique possesses several advantages over other filtering methods, such as high sensitivity and ability to filter the crack related AE data located along the source of damage. Source localization is an important part of any monitoring process and can also be utilized as a filtering method. The other advantage of SLF method lies in the fact that the proper filtering algorithm can detect the real hits as they occur, that is, in real time for reduction of the unrelated AE data; whereas other filtering methods such as Swansong II filter are often customized to the dataset and are therefore employed after the data has been acquired. The sequence of arrival time (TOA) of AE waves is utilized based on the sensor location on the CT specimen and the location of the defect source is determined by minimizing the *Chi Squared* error function. More details of *Chi Squared* Error function can be found in literature (PAC 2004, ASNT 2005).

Figures 5.11 to 5.14 show synchronization between the AE data and the strain field near the crack tip during cyclic loading which was monitored through DIC. The strain value perpendicular to the crack line as shown in Figure 5.11 through 5.14 was calculated based on the average strain in the area marked with a white circle at the crack tip as shown in the Figures 5.6 through 5.9. As the crack tip throughout the test is changing with time, this white circle was always placed in such a way so that the strain field near the crack tip was effectively monitored. The wave forms of the AE events at 335.65 seconds [61.1 MPa√m (55.6 ksi√in), early stage II] for different channels are shown in Figure 5.15, and these waveforms are indicative of events generated from friction. The micro-level fatigue crack extension (indicated by strain drop) did not produce detectable AE events at 335.65 seconds [61.1 MPa√m (55.6 ksi√in), early stage II], 825 seconds [63.5 MPa√m (57.8 ksi√in), middle stage II], or 1,296 seconds [65.5 MPa√m (59.6 ksi√in), middle stage II] (see Figure 5.11). Figure 5.11(a) shows accumulation of the strain field which indicates gradual formation of the plastic zone at the crack tip during cyclic loading and then extensive plastic deformation causing sudden micro-crack extension. Due to this tiny crack extension the strain field near the crack tip rapidly redistributes and the average strain measured within the white circular area drops as shown in Figure 5.11, where three micro-crack extensions are marked. It can be seen that several hundred load cycles are required to generate the plastic zone and subsequently the final fracture, where the process is considered to be dominated by ductile mechanisms such as plastic deformation, disbonding of inclusions, and generation and coalescence of microvoids.

In early stage II, stress intensity range ΔK less than 60 MPa√m (54.6 ksi√in) (see Figure 5.10), ductile mechanisms are dominant. For these mechanisms, it is speculated that waveforms are mainly associated with plastic deformation, disbonding of inclusions, and generation/coalescence of microvoids. The individual processes can produce AE events which are less energetic than brittle cleavage fracture, and the energy releases over a relatively longer period of time (ASNT, 2005). AE hits with relatively small amplitude were recorded at 1025.57 [64.4 MPa√m (58.6 ksi√in) middle stage II] and 2025.57

seconds [69.0 MPa√m (62.8 ksi√in), middle stage II]. However, it is difficult to conclude which mechanisms produce the events. Plastic deformation, inclusion disbanding, and cleavage fracture are potential sources. For inclusion disbonding and cleavage fractures small plastic deformation is required. In each load cycle, small plastic deformations occur at the crack tip. Throughout the test, fatigue crack extension predominantly occurs by plastic deformations which were observed in the strain field data as well as the stress intensity range values. Plastic deformations generally do not produce detectable AE events when the instrument threshold is set to 45 dB. No irregularities were observed in the strain field at 1025.57 seconds [64.4 MPa√m (58.6 ksi√in), middle stage II] and 2025.57 seconds [69.0 MPa√m (62.8 ksi√in), middle stage II], as shown in Figures 5.12(a) and (b). This indicates that either disbonding or cleavage fracture may produce these AE events. In early stage II, inclusion disbonding governs which may contribute to these events.

During the later stages [ΔK greater than 95 MPa√m (86.5 ksi√in), late stage II, see Figure 5.10], high amplitude AE data is dominant which may be produced by brittle fracture mechanisms such as cleavage fracture. From Figure 5.11 (a) it can be seen that the strain field drops due the the small crack extensions are slightly decreasing. This may be due to accumulation of strain near the crack tip decreasing before crack extensions. At higher stress intensity [greater than 95 MPa√m (86.5 ksi√in), late stage II] (higher strain), the crack grows in each fatigue cycle via plastic deformation. For cleavage fracture during fatigue crack extensions, small plastic deformation is required. When a crack tip is located at a ferrite grain, the strain rate is high enough to split the grain and pass through it which may then produce high amplitude AE events.

Figures 5.12 (b) and (c), 5.13 (a) and (c), and 5.14 (d) and (e) show strain drops which produce AE events. These drops may be considered to be due to fatigue crack extension via ductile mechanisms. Hence crack extension via ductile mechanisms in the later stage II [ΔK greater than 95 MPa√m (86.5 ksi√in)] can produce detectable AE events. When high amplitude AE hits are found in AE data [Figure 5.14 (b) and (f)], relatively small amplitude AE events are also found just surrounding those events. This observation can be explained using the theoretical background for dislocation crack tip shielding (Weertman 2007). According to this theory, a dislocation leaves the crack tip (into previously plastically deformed material) when the applied stress intensity factor K reaches the level:

$$K=gK_{\mathrm{gc}}=K_{\mathrm{gb}} \qquad (5.1)$$

Here K_{gc} is the critical K value for cleavage fracture for a Griffith–Inglis crack in an elastic solid, K_{gb} is the critical K value for dislocation emission, and g is a constant of order of magnitude 1.0. Dislocation emission occurs before cleavage failure when g is smaller than 1.0. It is argued that if the applied K is much greater than K_{gb} many dislocations will leave the crack tip but no further dislocation emission occurs once the radius ρ of the blunted crack tip reaches the value:

$$\rho \approx \frac{bK^2}{K_{gb}^2} = \frac{bK^2}{g^2K_{gb}^2} = \eta\frac{K^2}{G^2} \qquad (5.2)$$

Here b is the Burgers vector length of a dislocation. Hence, dislocations can be expected to be emitted from a blunted crack tip until ρ attains the value given by equation (5.2). In equation (5.1) and equation (5.2) K_{gc} is equal to:

$$k_{gc} = \sqrt{\frac{4\gamma G}{1-\upsilon}} \tag{5.3}$$

where γ is the surface energy of the solid and v is Poisson's ratio. (Note that the surface energy $\gamma \approx (1/2)\, \sigma_t\, d_t$ where $\sigma_t \approx (1/5)\, G$ is the theoretical strength of the solid and $d_t \approx 2b$.

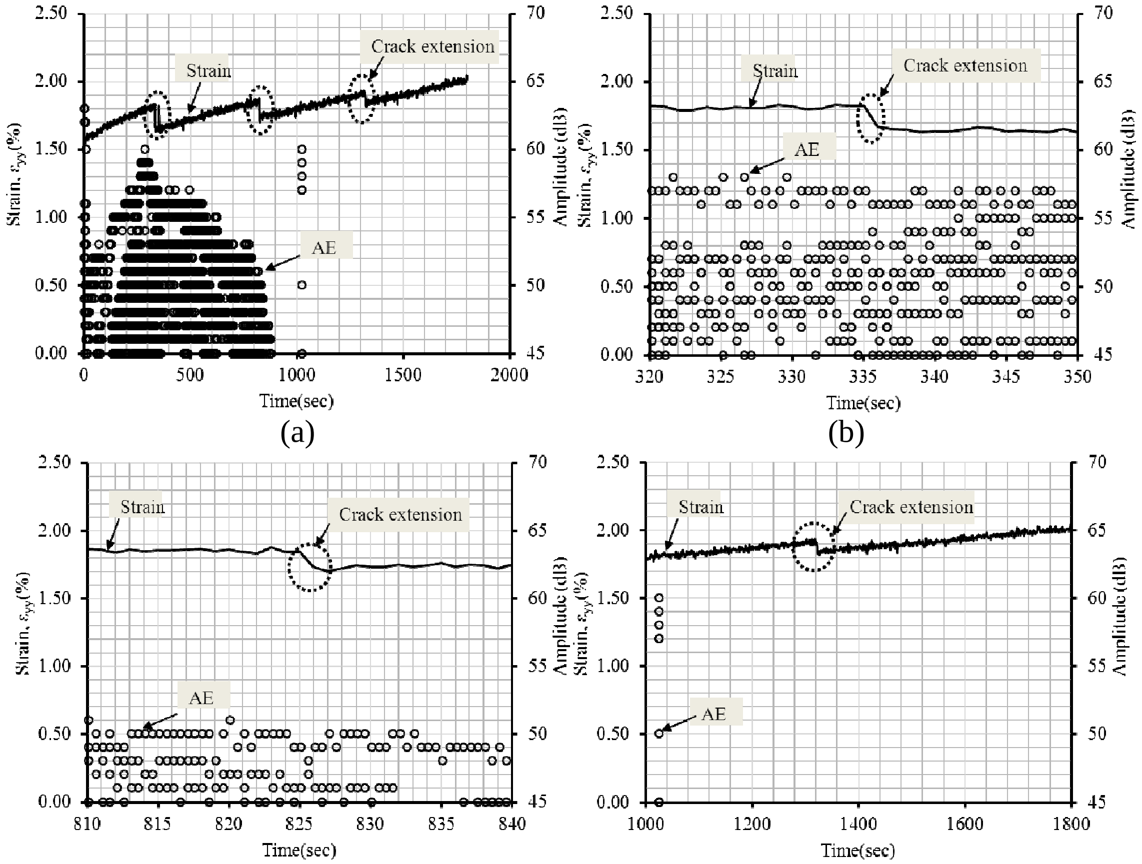

(a) (b)

(c) (d)

Figure 5.11. Strain fields, ε_{yy} and AE hits after eliminating below 80% load of the peak load and applying Swansong II filter along with a source location based filter: (a) between 0 to 1,800 seconds; [58.7 to 67.8 MPa√m (53.5 to 61.7 ksi√in)] (b) between 320 to 350 seconds [61.0 to 61.2 MPa√m (55.5 to 55.7 ksi√in)] (zoomed to assess first crack extension); (c) between 810 to 840 seconds [63.4 to 63.6 MPa√m (57.7 to 57.9 ksi√in)]; and (d) between 1,000 to 1,800 seconds [64.2 to 67.8 MPa√m (58.5 to 61.7 ksi√in)].

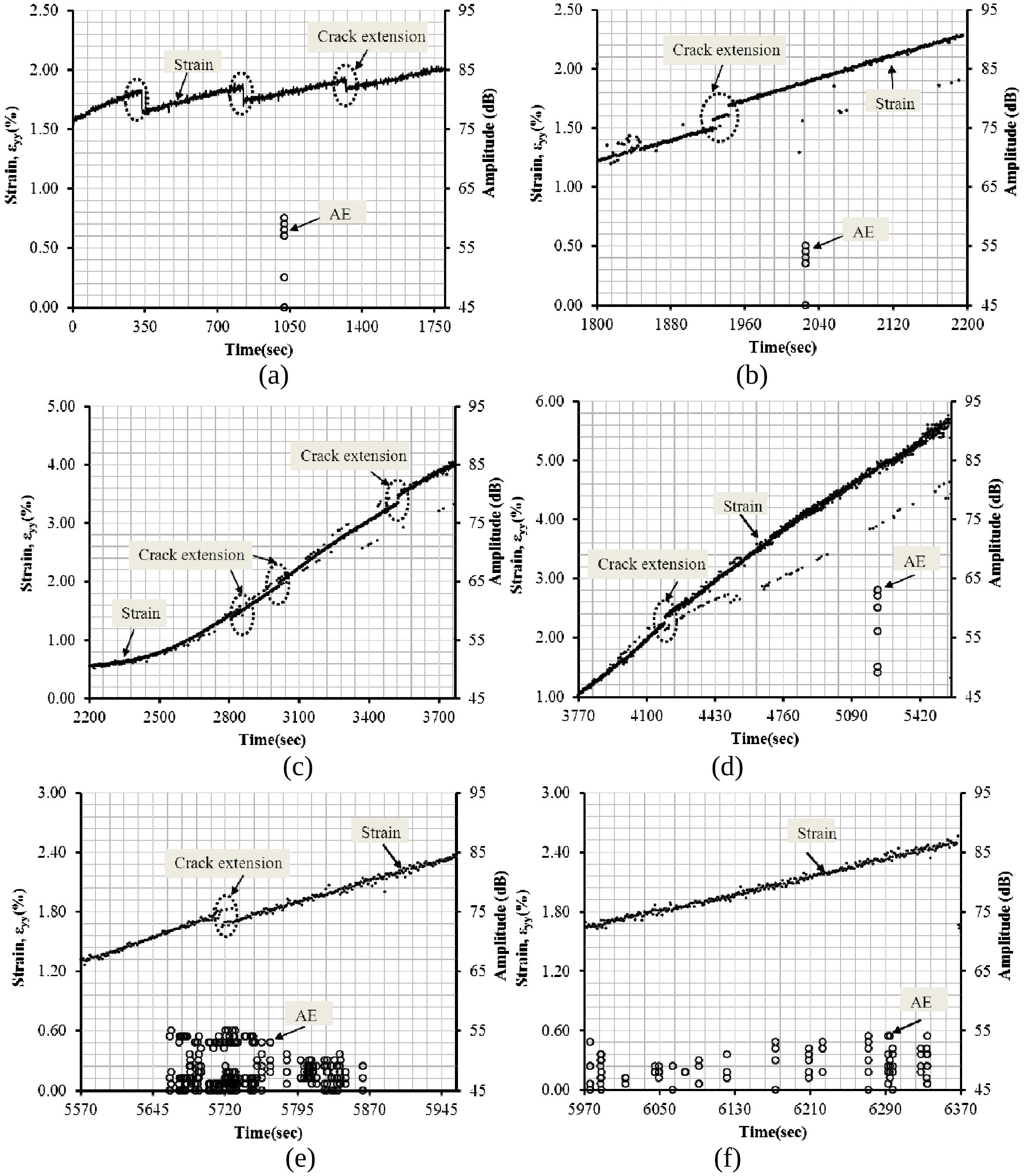

Figure 5.12. Strain fields, ε_{yy} and AE hits after eliminating below 80% load of the peak load and applying Swansong II filter along with a source location based filter: (a) between 0 to 1,800 seconds [58.7 to 67.8 MPa√m (53.5 to 61.7 ksi√in)]; (b) between 1,800 to 2,200 seconds [69.9 MPa√m (63.6 ksi√in)]; (c) between 2,200 to 3,769 seconds [78.7 MPa√m (71.6 ksi√in)]; and (d) between 3,770 to 5,569 seconds [91.6 MPa√m (83.4 ksi√in)]; (e) between 5,570 to 5,970 seconds [95.4 MPa√m (86.8 ksi√in)]; and (f) between 5,970 to 6,370 seconds [99.7 MPa√m (90.7 ksi√in)].

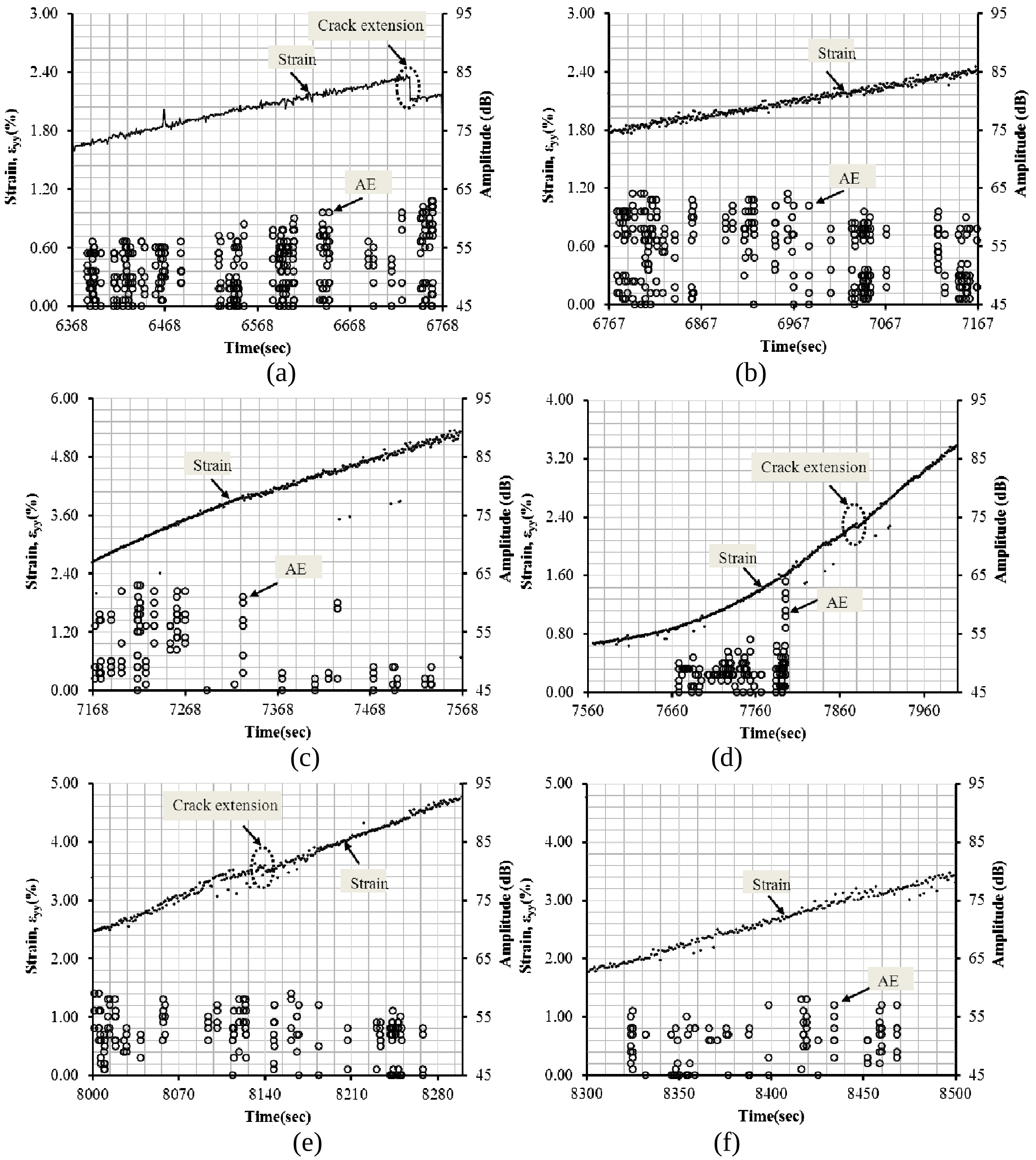

Figure 5.13. Strain fields, ε_{yy} and AE hits (filtered data): (a) between 6,368 to 6,768 seconds [99.6 to 104.4 MPa√m (90.7 to 95.1 ksi√in)]; (b) between 6,767 to 7,167 seconds [104.4 to 110.1 MPa√m (95.0 to 100.2 ksi√in)]; (c) between 7,168 to 7,568 seconds [110.1 to 117.0 MPa√m (100.2 to 106.5 ksi√in)]; and (d) between 7,560 to 7,960 seconds [116.9 to 125.4 MPa√m (106.4 to 141.1 ksi√in)]; (e) between 8,000 to 8,300 seconds [126.4 to 134.2 MPa√m (115.0 to 122.1 ksi√in)]; and (f) between 8,300 to 8,500 seconds [134.2 to 140.0 MPa√m (122.1 to 127.4 ksi√in)].

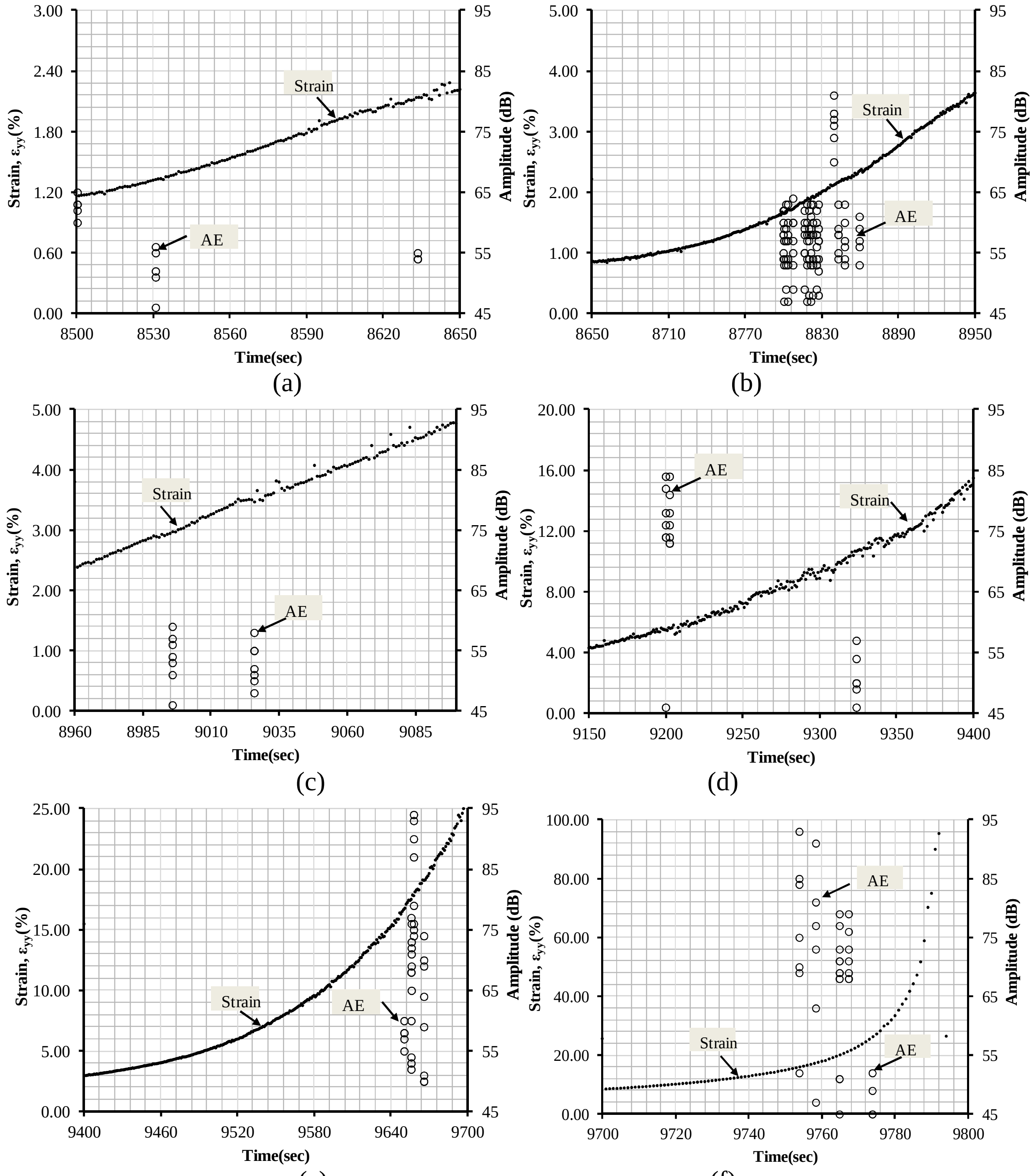

(a) (b)

(c) (d)

(e) (f)

Figure 5.14. Strain fields, ε_{yy} and AE hits (filtered data): (a) between 8,500 to 8,650 seconds [144.8 MPa√m (131.8 ksi√in)]; (b) between 8,650 to 8,950 seconds [155.7 MPa√m (141.7 ksi√in)]; (c) between 8,960 to 9,150 seconds [163.6 MPa√m (148.9 ksi√in)]; (d) between 9,150 to 9,400 seconds [177.2 MPa√m (161.3 ksi√in)]; (e) between 9,400 to 9,700seconds [205.4 MPa√m (186.9 ksi√in)]; and (f) between 9,700 to 9800 seconds [221.4 MPa√m (201.5 ksi√in)].

Characteristics of Waveforms:

During testing of the CT specimen, AE waveforms above 50 dB were recorded. Local crack extension was monitored through the strain field at the crack tip to assess the AE events associated with fatigue crack extension. Figures 5.15 and 5.16 show the typical waveforms of AE events in the time domain during the fatigue test. The waveforms of the AE signals considered to be associated with friction in the load trains are shown in Figure 5.15. From the overall scenario of the waveform analysis a completely different AE behavior was noticed where AE was first detected at the earlier stage of fatigue testing, where the wave forms may be mainly associated with ductile fracture mechanisms which produce less energetic AE and the energy release rate is relatively slow [Figure 5.16(a)], with alternating appearances during later stages where the brittle fracture mechanisms produce high amplitude acoustic emission and the energy is released within a very short period of time as shown in Figure 5.16(b). Therefore, these waveforms have important roles in AE source characterization and later may also be used as supportive for AE source characterization. Grating emission tests were performed to understand the characteristics of noise due to grating of the fractured surface [Figure 5.16(c)]. During grating tests, the magnitude of the cyclic load was insufficient for crack extension. A typical waveform from grating emission is shown in Figure 5.16(c). Pencil lead break tests were also performed to understand the characteristics of genuine hits [Figure 5.16(d)]. In a burst-type waveform, typical parameters include amplitude, rise time, duration, and counts.

The waveforms from grating emission have long rise time, long duration, and poorly defined peak amplitude. The waveforms from brittle crack related events are characterized by a relatively clean front-end, short rise time, short duration, and high amplitude [Figure 5.16(b)]. From a previous study it is generally believed that false 'hits' typically have low amplitude and longer duration. These waveforms can play important roles in AE source characterization and may be utilized to extract AE events associated to fatigue crack growth for in-service steel bridge health monitoring.

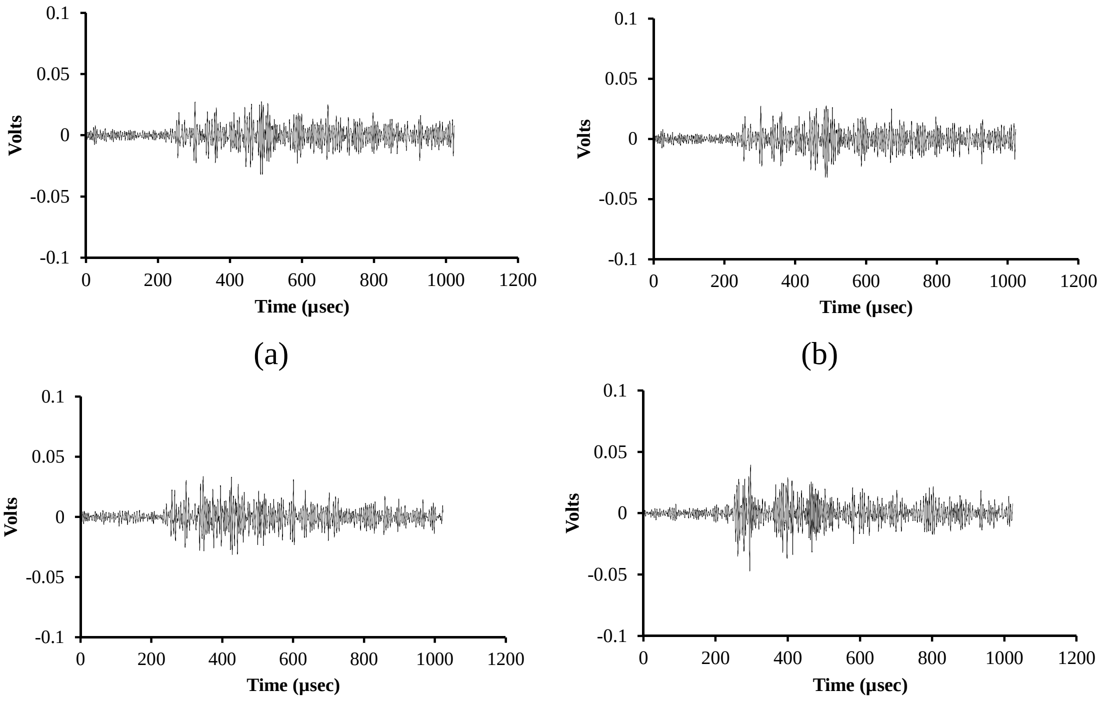

(a)

(b)

(c)

(d)

Figure 5.15. Friction waveforms at 335.65 seconds [61.1 MPa√m (55.6 ksi√in)]: (a) channel 1; (b) channel 2; (c) channel 3; and (d) channel 4.

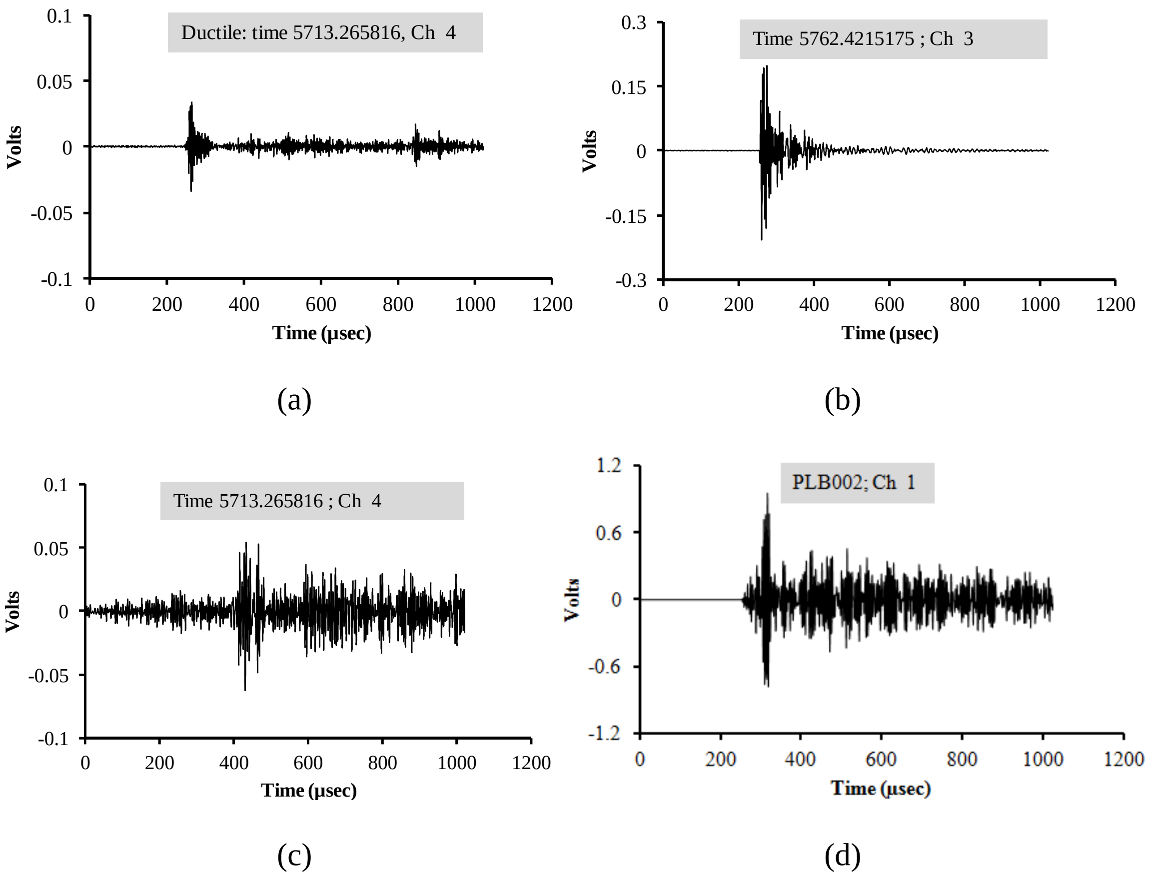

(a) (b)

(c) (d)

Figure 5.16. Typical waveforms (x-axis in microseconds and y-axis in millivolts) of AE hits associated with fatigue: (a) ductile mechanism; (b) brittle mechanism; (c) grating emission; (d) pencil lead break (PLB) test

Fractographic Analysis:

At the conclusion of fatigue testing, samples were cut (1 and 2 from early Stage II [57 to 60 MPa√m (51.9 to 54.6 ksi√in)], 3 and 4 from middle Stage II [60 to 95MPa√m (54.6 to 86.5 ksi√in)], and 5 and 6 from the late Stage [95 to 128 MPa√m (86.5 to 116.5 ksi√in)] / early stage Stage III [128 to 135 MPa√m (116.5 to 122.9 ksi√in)] of the fatigue crack) from the fracture surfaces of the CT specimen and examined with a Scanning Electronic Microscope (SEM). In early Stage II fatigue (crack length around 10 mm), the fracture surface was dominated by microvoid coalescence [Figures 5.17(a) and (b)]. In mid Stage II (crack length around 30 mm) [Figures 5.17(c) and (d)] the fracture surface shows quasi-cleavage with some traces of fatigue striations [Figure 5.17(c)]. In late Stage II (crack length around 60 mm) [Figures 5.17(c) and (d)] the fracture surface shows quasi-cleavage with some traces of fatigue striations [Figure 5.17(c)].

Fractographic analysis of SEM images can provide indications of failure mechanisms during fatigue crack growth. The failure mechanisms depend on the stage of fatigue cracking (Figure 5.17). In this study three representative clusters in stage II of fatigue crack growth are considered. Region I [Figure 5.17(a) and (b)] corresponds to early stage II [57 to 60 MPa√m (51.9to 54.6 ksi√in)] fatigue crack growth. The mechanisms are predominantly transgranular (ductile), although grating action may affect the fractured surface and could preclude further in-depth examination. Mid-region Stage II [60 to 95MPa√m (54.6 to 86.5 ksi√in)] (intermediate stable crack growth) fracture tends to be intergranular (splitting of the ferrite grain) combined with transgranular (separation of grain).

Region III is at the end of stable crack growth (Stage II) [128 MPa√m (116.5 ksi√in)]. In this region stress intensity has a higher value and hence cracking propagates at a higher strain rate (plastic zone formation takes place more quickly). Crack growth mechanisms are predominantly transgranular with few brittle mechanisms (cleavage-type fractures). The presence of striations, attributed to ductile mechanisms, was observed throughout all three regions. At higher stress levels when the maximum stress intensity approaches the fracture toughness, crack growth is predominantly due to cleavage fracture which produces relatively high amplitude AE.

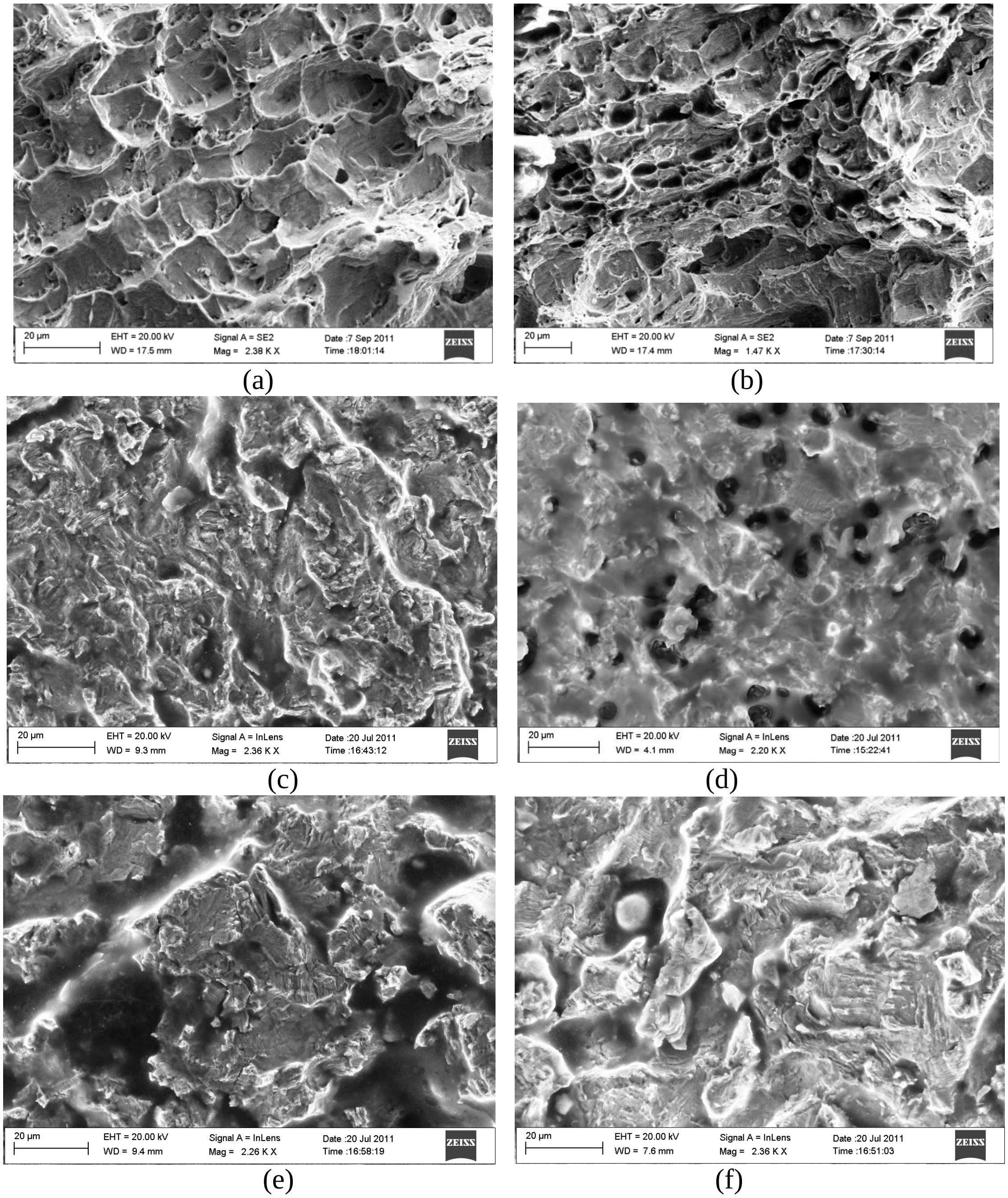

Figure 5.17. Scanning electron microscopic images in stage II fatigue crack growth: (a, b) early stage II; (c, d) middle of stage II; and (e, f) end of stage II.

The above discussion summarizes two governing mechanisms: one of which is predominantly ductile and includes plastic deformation, inclusion disbonding, and microvoid coalescence (ligament shearing). The other is predominantly brittle and is based on intergranular cleavage fracture. Ductile mechanisms, which are predominant at lower crack growth rates, are due to intergranular crack growth, while the brittle mechanism is due to intergranular cleavage crack growth.

Because splitting of the ferrite gain is affected by initial defects one can conclude that the resulting intergranular fracture is primarily a random phenomenon, the frequency of which increases with increasing stress intensity range (ΔK). On the other hand, transgranular fracture characterizes the ductile mechanisms and these are predominant in the lower stress intensity ranges. The AE data investigated to date is generally consistent with the fractographic evidence.

5.7 CONCLUSIONS

The objective of the research presented in this paper is to investigate the AE source mechanisms of a steel bridge material, and to characterize the AE waveforms, if any, associated with fatigue crack extension. The following conclusions are drawn:

- Proper data filtering is critical for the successful implementation of the AE technique for in-service structural health assessment and monitoring.
- Digital Image Correlation (DIC) can provide clear forewarning of plastic zone formation and subsequent crack extension. This is useful for assessing AE events associated with fatigue crack extension. However, not until recent advances in computing, digital imaging, and electron microscopy has the acquisition of high-resolution strain fields and their comparison with microstructure been possible.
- AE depends on the cracking phenomena. In the early stage, fatigue crack extensions do not generally produce detectable AE events as crack growth rates are relatively low. At middle and end of stage II fatigue crack extension by means of ductile

mechanisms produce small amplitude acoustic emission events. It is hypothesized that other contributing phenomena such as plastic deformation, disbonding in the microstructure, and generation of microvoids may contribute to AE in fatigue cracking.

- A brittle mechanism via cleavage fracture occurs at higher strain rate while stress intensity is relatively high. It is a random phenomena and very challenging in extracting from the AE data by monitoring the strain field using digital image correlation, as it requires very small plastic deformation.
- From fractographic analysis, it can be seen that there are two governing mechanisms. Ductile mechanisms may produce low amplitude AE events. Brittle mechanisms are a more random phenomenon. While higher stress intensity can increase the probability of intergranular cleavage fracture, fatigue crack growth in the typical steel bridge material studied is dominated by transgranular fracture.
- Brittle mechanisms produce very energetic, relatively clean front-end, short rise time, short duration, and high amplitude AE wave forms. While others have long rise time, long duration, and poorly defined peak amplitude AE waveforms.

CHAPTER 6

ASSESSING PROBABILITY DETECTION BASED ON ACOUSTIC EMISSION ASSOCIATED WITH FATIGUE CRACK EXTENSION IN A572 STEEL

The probability of Acoustic Emission (AE) detection associated with fatigue crack extension in steel bridge components is a challenging problem due to the complexity of the AE sources. AE is a very promising technique for structural health monitoring, particularly for automated micro-crack detection, as it is generated by the material itself, unlike other nondestructive testing techniques (such as impact echo and ultrasonics), which require external input sources. The probability of detection is an ongoing challenge because AE sensors are not only sensitive to the AE signals but also to mechanical noise; and it is therefore difficult to interpret the actual signals related to microcrack extension. Probability of detection may also be influenced by the medium of wave propagation, threshold settings, sensitivity and frequency range of the sensors, and the source to sensor distance. This chapter presents the probability of AE detection associated with fatigue crack extension in steel bridge elements as a function of the stress intensity range. The AE events associated with fatigue crack extension are assessed using moment tensor and b-value analysis. The Poisson distribution and Weibull distribution are employed to calculate the probability of AE detection associated with fatigue crack extension at different levels of fatigue crack growth which may later facilitate determining the priorities of instrumentation to the in-service steel bridges for health assessment, thereby reducing the cost of maintenance and repair.

6.1 INTRODUCTION

When a crack is subjected to cyclic loading, the crack tip will travel a very short distance in each loading cycle, in the range of 0.10 μm/cycle (4 x 10^{-6} in./cycle) to 1 μm/cycle (4 x 10^{-5} in./cycle) (Hamstad and McColskey 1999, ASNT 2005). As a small crack extends, stress free surfaces are created and stress fields in the crack tip abruptly redistribute**.** Typically, at the lower crack growth rate, several thousand cycles are required to obtain one valid acoustic emission signal. At the higher crack growth rate, approximately one or two cycles are required for a valid event from A514 steel and the other steels require 18 to 130 cycles for a valid event (Hamstad and McColskey 1999, ASNT 2005). Plastic deformation is the primary source of acoustic emission in metallic materials (ASNT 2005); however, they are rarely very energetic events (Scruby 1987). When plastic deformation at the crack tip is prohibited, the crack can travel through grains by splitting atomic bonds in lattice planes (ASNT 2005). This is called intra- or trans-granular cleavage. When the crack propagates along grain boundaries, it is referred to as inter-granular cleavage. Cleavage or similar highly emissive mechanisms produce very energetic acoustic emissions events (Scruby 1987, Hossain et al. 2012, Hossain et al. 2013).

AE transducers are usually made of piezoelectric slabs and have a resonant behavior; their sensitivity varies with frequency (f_t) and is usually greatest in the range from 0.1 to 1.0 MHz (ASNT 2005). Neither the static surface strains nor very high frequency components are sensed. If the crack extends rapidly and then stops so that its growth time is about equal to $1/f_t$, then the emitted wave fronts are dominated by frequency components in the detectable range (ASNT 2005).

6.2 FATIGUE CRACK PROPAGATION

Crack growth rate curves (for example Figure 6.1) describe crack growth behavior. Such curves show the relationship between crack growth rate, da/dN, and stress intensity range, ΔK. Crack growth has three stages depending on the stress intensity: Stage I-low speed cracking near the threshold, Stage II-stable cracking, and Stage III-unstable cracking. Stage II is of practical importance. Stage III crack growth leads rapidly to catastrophic failure, so a cracking level of interest is the transition point between stage II and stage III. Stress intensity is a key factor for understanding fatigue crack growth behavior.

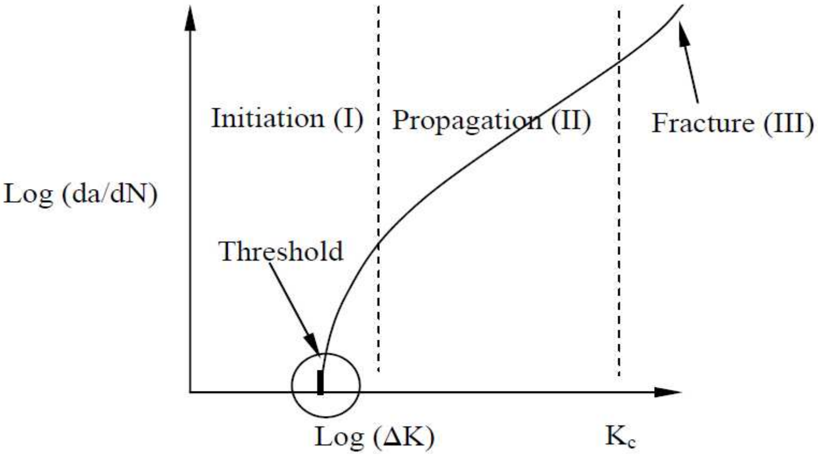

Figure 6.1. Typical fatigue crack growth rate curve (after Anderson 2005).

6.3 PART A: ASSESSING AE DATA ASSOCIATED WITH CRACK EXTENSION

Fatigue testing was conducted for evaluating the probability of AE detection associated with fatigue crack extension using compact tension (CT) specimens. Two CT (designated as CT1 and CT2) specimens of ASTM A572 Grade 50 structural steel were utilized for AE monitoring during constant amplitude cyclic loading. The specified yield strength and ultimate strength of ASTM A572 Grade 50 structural steel are 374 MPa (54.3 ksi) and 535 MPa (77.6 ksi), respectively. The effective width (W) of the CT specimen is 241 mm (9.5 inch) and the thickness (t) is 12.7 mm (0.5 inch), with an initial crack (notch) length of 82.6 mm (3.25 inch) [Figure 6.2(a)]. A clip gage and a microscopic video camera were used to monitor crack propagation for the first CT specimen (CT1). Digital image correlation (DIC) was employed to monitor the strain field near the crack tip for the second CT specimen (CT2). The maximum applied load was 65 kN (14.6 kips) with a load ratio (R) of 0.1. Both specimens were loaded at a frequency of 2 Hz. Two R15I-AST and six wideband (WDI) sensors were used to collect acoustic emission data (Mistras Group, Inc.) [Figure 6.2(b)]. Specially designed magnetic hold downs were used to couple the sensors to the face of the steel surface and epoxy was used to couple the sensors to the specimen edges. All AE sensors had internal pre-amplification of 40 dB. The amplitude threshold was set at 45 dB and signals were stored and displayed with a DiSP unit (Mistras Group, Inc.). The AE events associated with different mechanisms were screened using moment tensor analysis, b-value analysis, and visual examination of the waveforms.

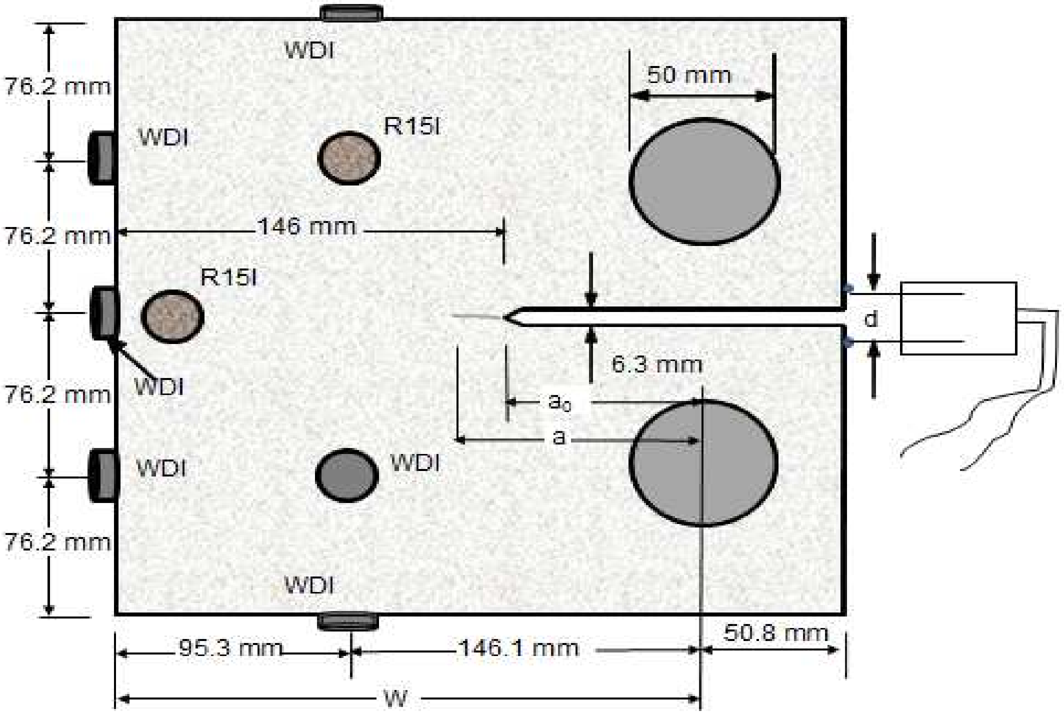

(a) schematic

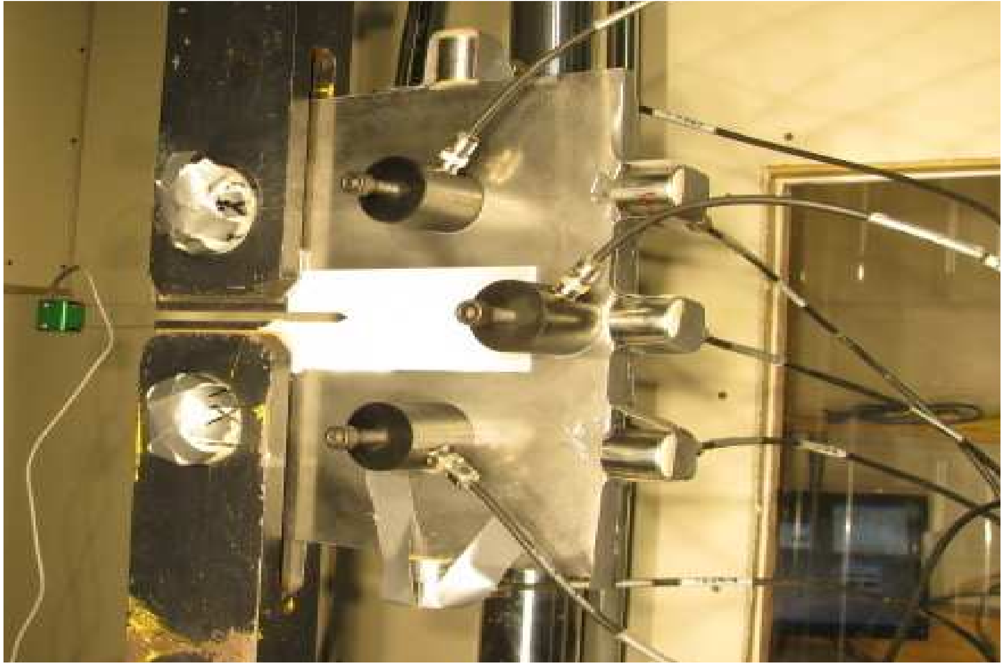

(b) photograph during testing with DIC setup

Figure 6.2. Compact tension (CT) specimen.

6.4 MOMENT TENSOR ANALYSIS

Shen et al. (2001) developed a moment tensor inversion procedure by using only P-wave amplitudes. The computer code SiGMA (simplified Green's function for moment tensor analysis) is commonly used for this procedure. For this study a MATLAB (Matlab 2010) code was developed for solving equation (6.1) by selecting the P-wave portion from the full-space Green's function of homogeneous and isotropic material-

$$A(x) = \frac{CsR(s,r)}{R}\begin{pmatrix} r_1 & r_2 & r_3 \end{pmatrix}\begin{bmatrix} m_{11} & m_{12} & m_{13} \\ & m_{22} & m_{23} \\ Sym & & m_{33} \end{bmatrix}\begin{pmatrix} r_1 \\ r_2 \\ r_3 \end{pmatrix} \tag{6.1}$$

where Cs = coefficient containing the sensor sensitivity to be calibrated (25 volts/mbar), R = the distance between the source and the sensor, and R(**s**, r**) =** the reflection coefficient associated with the direction of sensor sensitivity **s** and direction of wave incidence r from the source, as shown in Figure 6.3. r_1, r_2 and r_3 are direction cosines from the source to the sensor. The co-ordinate definition (x, y, z) or (1, 2, 3), transducer locations and typical source location and R are shown in the Figure 6.4. The reflection co-efficient, R(s, r) is calculated using equation (6.2) as per Giurgiutiu (2007)-

$$R(s,r) = -\frac{\rho c_p \cos\theta - \rho^* c_p^* \cos\theta *}{\rho c_p \cos\theta + \rho^* c_p^* \cos\theta *} \tag{6.2}$$

Where density of ASTM A572 Grade 50 structural steel ρ = 7850 kg/m^3, and the case and face materials of WDI sensor are stainless steel (304) and ceramic, respectively (Mistras Group, Inc.). The material information of ceramic is not provided. Therefor ceramic material can be Porcelain (Specific Gravity, G = 2.2-2.4), Alumina Porcelain (G = 3.1-

3.9), Zirconia Porcelain (G = 3.5-3.8), Alumina Silicate Refractory (G = 2.2-2.4), Magnesium Silicate (G = 2.3-2.8), Steatite (G = 2.5-2.7), and/or Forsterite (G = 2.7-2.9) (Wikipedia.org). The density of 2700 kg/m^3 is considered for ceramic face material of the sensor face. Therefore, density of steel of CT specimen, ρ = 7850 kg/m^3 and the ceramic material, ρ^* = 2700 kg/m^3.

Table 6.1. Wave speed calculation.

Material	**Elastic Modulus, E (GPa)**	**Density (kg/m^3)**	**Axial speed, $C_p=\sqrt{(E/\rho)}$ (m/s)**
Steel	200	7850	5048
Ceramic	15	2700	2357

The transducers (1, 2, 3, 4, and 5) are attached on the edges of the CT specimens, whereas the sixth transducer is attached on the surface (out of plane) as shown in Figure 6.4 to avoid non-trivial solution of the moment tensor. The direction of the transducer sensitivity (s), θ, as shown in Figure 6.3 (typical) is summarized in Table 6.2. The direction of wave incidence (r), θ^*, depends on the location of the transducers as well as the source location of the AE events. Therefore the reflection co-efficient R(s, r) also varies accordingly. A typical cosine of wave incidence and reflection co-efficient of the wave R(s, r) are summarized in Table 6.2. When the source location and the amplitudes of the first motion are known, the six independent components of the moment tensor m_{pq} can be determined by solving the simultaneous equations of equation (6.1) for each individual AE event.

Applying the eigenvalue analysis to the moment tensor, the crack kinematics can be obtained. A classification of the crack types into shear mode, tensile mode, and mixed mode can be quantitatively made.

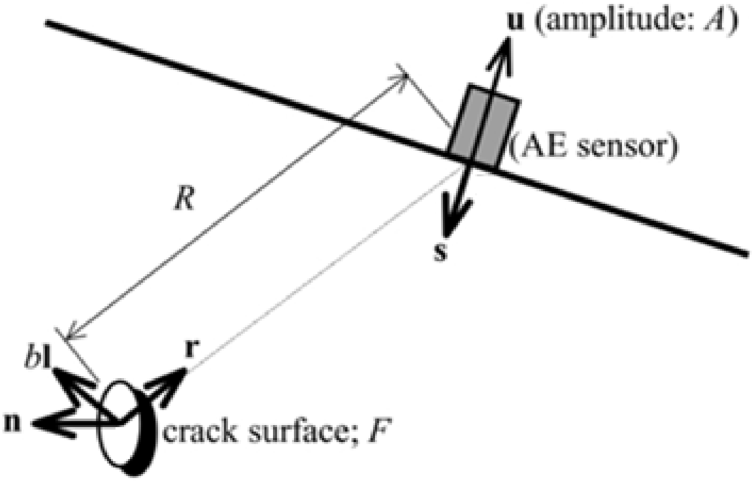

Figure 6.3. AE wave observation (after Shen et al. 2001).

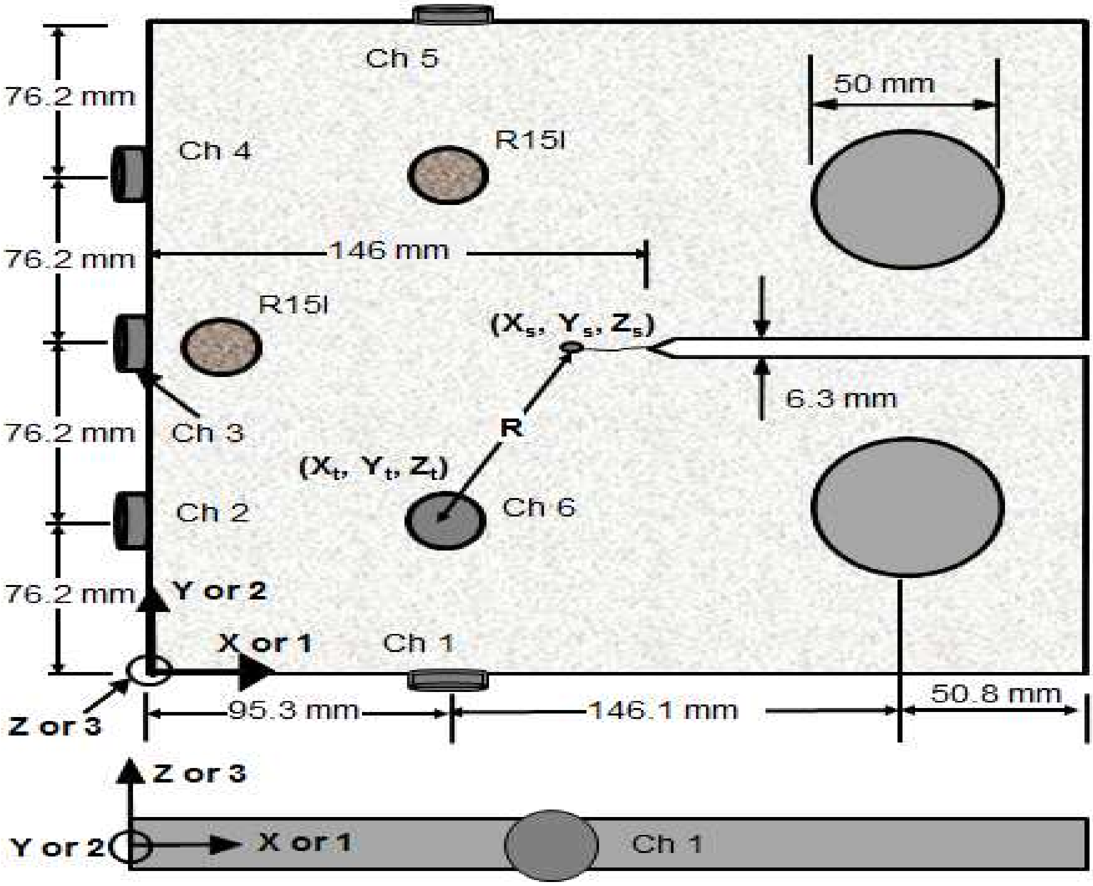

Figure 6.4. Co-ordinate and transducers location.

The eigenvalues of the moment tensor are decomposed into X = shear component; Y = deviatoric (compensated linear vector dipole; CLVD) component and Z= hydrostatic component as shown in Figure 6.5. Three eigenvalues are normalized and uniquely decomposed into three ratios X, Y, and Z. Conveniently, the following tensor, m_{pq}, is defined from the vector components b_k and n_l and is referred to as a moment tensor:

$$m_{pq} = C_{pqkl} b_k n_l \tag{6.3}$$

where C_{jklm}= elastic modulus. Solving the characteristic equations of equation (6.3), three eigenvalues are obtained. One decomposition of the eigenvalues can be developed to classify the AE source into a tensile crack and a shear crack depending on the X values. Setting the maximum eigenvalue X for the shear crack, the principal components become X, 0, and -X. In the pure tensile crack, three eigenvalues are decomposed into deviatoric components (CLVD, or compensated linear vector dipole) and hydrostatic mean components (the isotropic part), of which the maximum values are indicated by Y and Z, respectively.

Assuming an AE source as a crack of mixed mode, the tensor components are considered as the sum of tensile and shear components. Thus, three eigenvalues are decomposed into three ratios X, Y, and Z as follows: 1.0 = X + Y + Z. The intermediate eigenvalue/the maximum eigenvalue = 0 - 0.5Y + Z. The minimum eigenvalue / the maximum eigenvalue = - X - 0.5Y + Z. After determining the eigenvalues of the moment tensor, the above decomposition is solved and the ratios X: Y: Z are determined. Based on the results of numerical experiments, a simple criterion is proposed for the classification of crack types.

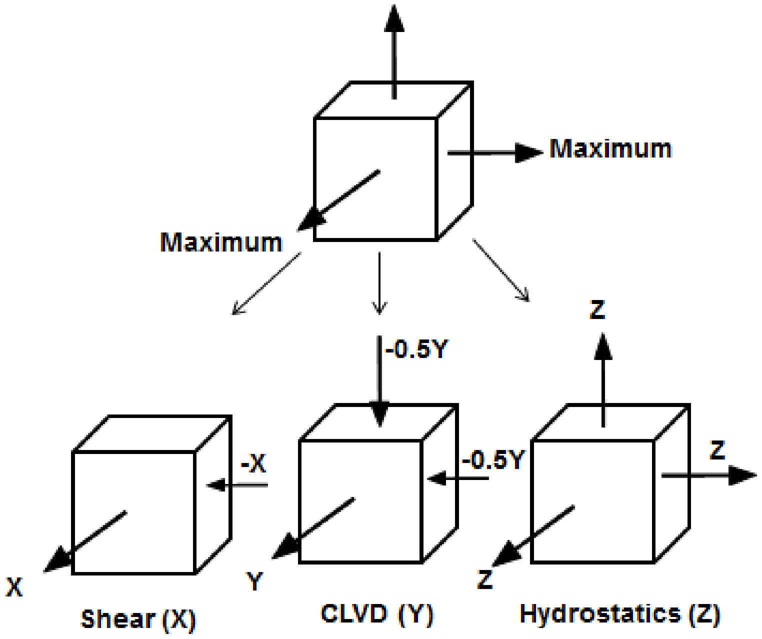

Figure 6.5. Eigenvalue decomposition of the moment tensor.

When the ration, X, is greater than 60%, AE source is referred to as a shear crack. In the case less than 40%, AE source is classified as a tensile crack. In the procedure, the ratios of eigenvalues and the relative values of moment tensor components are necessary. It implies that amplitude of the first notion in equation 6.1 should be recorded as relative values. Consequently, the sensor calibration is only needed to compensate the equal sensitivity. In a general sense, the relative value X shows the contribution of shear crack motion. From the relative value of X, each crack growth event can be classified into either a tensile or a shear failure. A pure tensile crack implies that the crack vector is parallel to the crack normal, in which case X becomes 0 %. In contrast, a pure shear crack corresponds to the case X = 100%, where the crack vector is perpendicular to the crack normal. Thus, all events can be classified into tensile cracks (X < 40%), mixed cracks (40% < X < 60%), or shear cracks (X > 60%). Sample calculations of moment tensor and composition ratios of Eigen values are shown in Figures 6.6, 6.7 and Table 6.2.

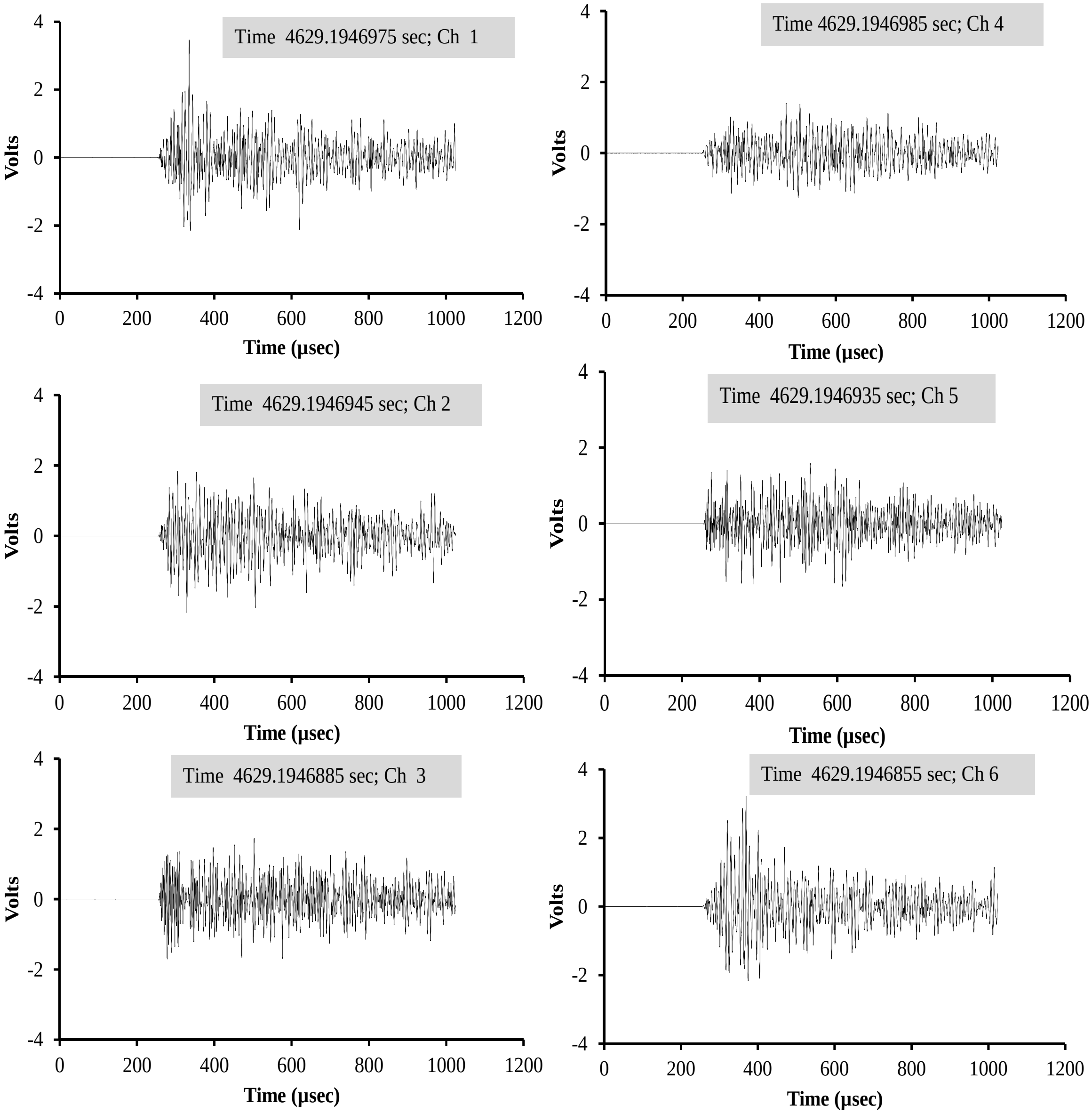

Figure 6.6. Presentation showing a typical waveform set.

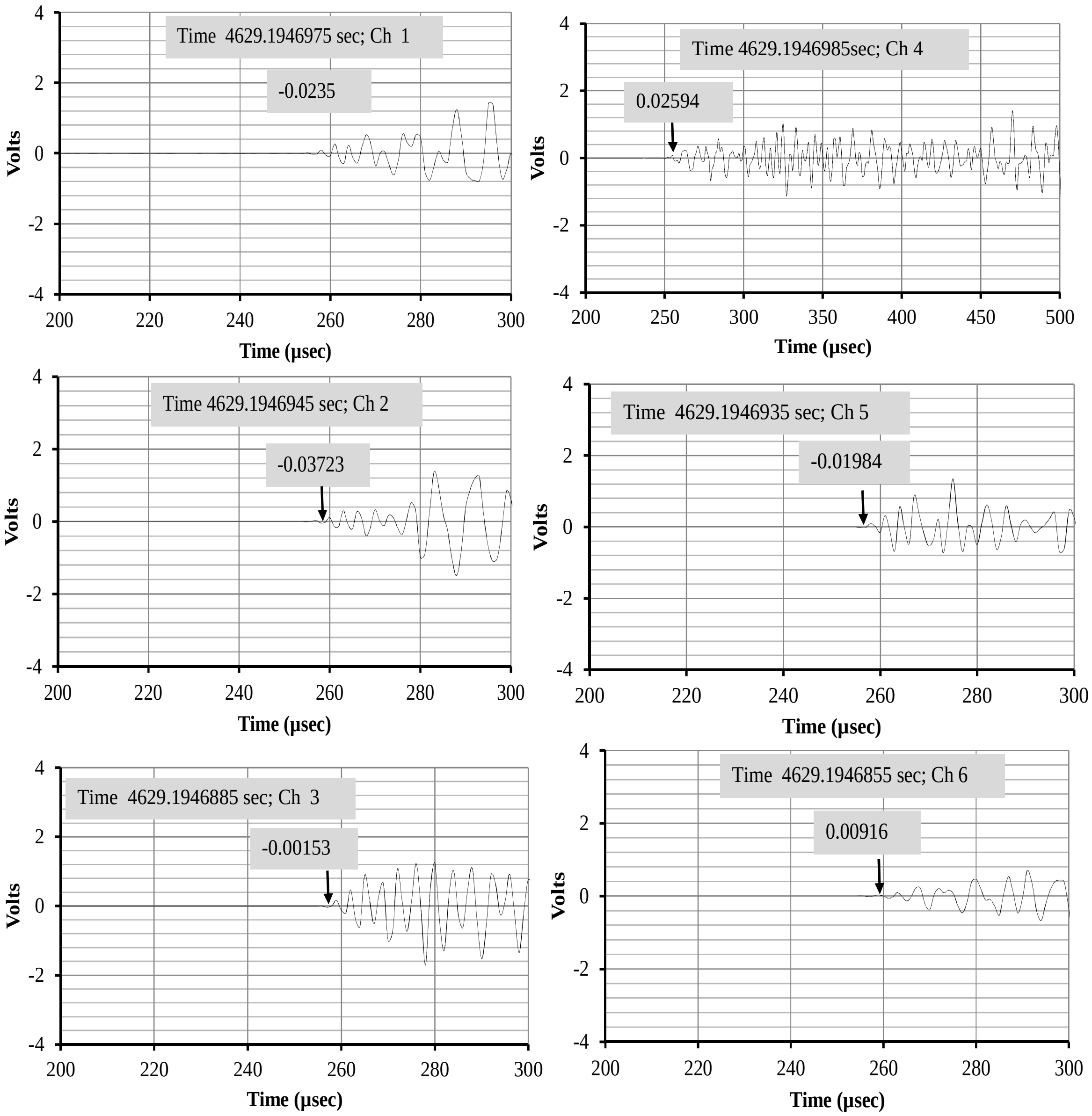

Figure 6.7. Presentation showing a typical waveform set (zoomed to assess amplitude of first wave amplitude for P-wave)

Table 6.2. Sample Output from the Moment Tensor Analysis (in metric system)

*** AE Source Inversion***

[Channel Data]

Ch.	Transducer Position (m)			Arrival Time	Amplitude
	x_t	y_t	z_t	second	Volt
Ch 1	0.09525	0	0.0000	4629.1946975	0.02350
Ch 2	0.0000	0.0762	0.0000	4629.1946975	-0.03723
Ch 3	0.0000	0.1524	0.0000	4629.1946885	-0.00153
Ch 4	0.0000	0.2286	0.0000	4629.1946985	0.02594
Ch 5	0.09525	0.3048	0.0000	4629.1946935	-0.01984
Ch 6	0.09525	0.0762	0.0063	4629.1946855	0.00916

*Velocity of P-wave : 5048 (m/sec) (Table 6.1)
*Poison's ratio : 0.2900

[Solution]

Step 1: AE Source Location (m) $x_s = 0.1135$ $y_s = 0.1502$ $z_s = 0$ (assume)

Step 2:	Direction Cosines			Transducer Direction			Reflection Co-efficient
Channel	r_1^*	r_2^*	r_3^*	x	y	z	R(s, r)
Ch 1	0.121	0.993	0	0	1	0	-0.2777
Ch 2	0.838	0.546	0	1	0	0	-0.1975
Ch 3	1.000	-0.019	0	1	0	0	-0.2808
Ch 4	0.823	-0.568	0	1	0	0	-0.1889
Ch 5	0.117	-0.993	0	0	-1	0	-0.2777
Ch 6	0.239	0.968	-0.082	0	0	-1	-0.2657

* $r_1 = (x_s-x_t)/\sqrt{[(x_s-x_t)^2+(y_s-y_t)^2+(z_s-z_t)^2]}$
$r_1 = (y_s-y_t)/\sqrt{[(x_s-x_t)^2+(y_s-y_t)^2+(z_s-z_t)^2]}$
$r_1 = (z_s-z_t)/\sqrt{[(x_s-x_t)^2+(y_s-y_t)^2+(z_s-z_t)^2]}$

Step 2: Moment Tensor Solution

0.0358	0.1642	0.0451
0.1642	1.0000	0.3177
0.0451	0.3177	0.0693

Step 3: Eigen Value Analysis

Eigen vector, v =			Eigen value, e =		
-0.1339	0.9789	0.1544	-0.0295	0	0
0.3116	-0.1063	0.9442	0	0.0099	0
0.9407	-0.1745	0.2908	0	0	1.1247

Table 6.2. Sample Output from the Moment Tensor Analysis (continue)

Normalized Eigen value, en(diagonal) =

$X+Y+Z = e_1/e_1 = 1.1247/1.1247= 1$
(A)
$0-0.5Y+Z = e_2/e_1 = 0.0099/1.1247 = 0.0088$ (B)
$-X-0.5Y+Z = e_3/e_1 = -0.0295/1.1247-0.0263 = -0.0262$ (C)

X= Ratio of the maximum shear contribution; Y = Ratio of tensile component; Z = Ratio of the maximum isotropic tensile.

Tensile crack :$X < 40\%$; Shear crack: $X > 60\%$; Mixed mode: $40\% \leq X \leq 60\%$

Step 4: Source characterization solution

Solving Equations A, B and C for X,

Shear, X (percentage) = $0.09 < 40\%$ '****** Therefore,

Type of crack:*****Tensile Crack*****

6.5 AE DATA FILTERING

Signal identification and data filtering is a necessary step for acoustic emission monitoring. In addition to plastic deformation and crack extension, AE sensors are also sensitive to unrelated noise. Noise mainly arises from grating between fracture surfaces and abrasion in the load train. Grating emission occurs due to friction between the fractured surfaces at crack closure and crack opening. To minimize grating emission, AE collected below 80% of the maximum load was eliminated.

Specialized grating emission tests also were performed to understand the characteristics of noise due to grating. In these tests, the magnitude of the cyclic load was reduced so as to be insufficient for crack growth. Pencil lead break tests were also performed to understand the characteristics of genuine hits. In a burst-type waveform, typical parameters include amplitude, rise time, duration, and emission counts. The waveform from grating emission has long rise time, long duration, and poorly defined peak amplitude. The waveform from crack related events is characterized by a relatively clean front-end, short rise time, short duration, and high amplitude. Based on the characteristics of waveforms, Swansong II filtering was also employed to minimize mechanical noise. Swansong II filtering utilizes a technique which takes advantage of specific characteristics of unwanted hits (longer duration and low amplitude), as AE hits arising from sliding or mechanical rubbing typically have relatively longer duration and lower amplitude.

6.6 ACOUSTIC EMISSION DATA

The total number of AE hits recorded throughout the test was 312,527 and 150,615, for specimen CT1 and CT2 [Figure 6.8(a)], respectively. The term 'hit' refers to the detection and measurement of an AE signal on any individual channel and the term 'event' refers hits of 3 or more sensors within a particular period of time. Based on the characteristics of the waveform of AE hits, Swansong II filter and 80 % of the peak load filters are applied. Swansong filter is based on the amplitude and durations of the AE hits. Mechanical noises have higher duration and relatively low amplitude. AE hits. Details of the Swansong II filter and load filter may be found in article of Yu et at. (2011).

By visual inspection of the waveforms, many of the AE hits are considered as hits associated with the grating or friction between the fracture surfaces during opening and closure of the crack. Previous study showed the crack extends above the 80 % (52 kN) of the peak load (65 kN). The idea for load filter is fatigue crack extents during cycling loading only during opening of the crack. Among those 1,484 (less than 0.5%) of the hits were classified as being of interest when the data was filtered to eliminate hits occurring below 80% of the peak load for CT1. Whereas after employing the 80% load filter and Swansong II filter, AE data contains lots of noises, remaining hits 107,642, which is approximately 70% of the total hits in CT2 specimen [Figure 6.8 (b)]. Though the dataset has been filtered to exclude hits below 80% of peak load, some AE events may still be due to friction between the fracture surfaces. Synchronization of AE data with parametric (load) shows the presence of AE in each cycle during crack opening as well as crack closure also. From CT1 it can be seen that less than 1% of the total hits during fatigue testing may be potentially associated with fatigue crack extension, whereas the remaining signals may be associated with mechanical noise in the loading train, reflections, and grating emissions. The waveforms of these AE events for different channels were visualized manually and it seems to indicate that these AE events are generated from friction or reflections.

To minimize acoustic emission associated with reflections the hit lockout feature was used. The hit lockout value is a length of time or distance, which controls the interval between consecutive hits. The hit lockout value used in this test was 40 micro-seconds. This hit lockout time was calculated based on the specimen dimension and wave speed. Calculated average wave speed was 5,770,000 mm (227,000 inch) per second and the wave travels a distance of 231 mm (9.10 inch) during a 40 micro-second period. The distance between the crack tip and the edge of the specimen is in the range of 114 mm (4.49 inch) to 146 mm (5.75 inch). Any energy release at the crack tip will travel as elastic waves and hits the sensors directly and part of the wave reflected at the edge of the specimen, and come back toward the sensors. For example, any crack extension may produce an elastic wave, travel through the medium, hits sensor 3 directly (shortest distance from crack tip) and top (face where sensor 5 is attached) or bottom edge (face where sensor 1 is attached), as shown in Figure 6.2, simultaneously. Depending on the energy of the incident wave, part of the incident energy may reflect from the edge, travel toward and hit sensor 3. Therefore the time difference between these two successive hits is in the range of 13 (3 inch/227,000 inch/sec) to 33 (7.5/227,000 inch/sec) micro-seconds. Hence after receiving the direct hit, the sensor will lock out and will not receive any hit when the time difference between two successive hits is less than 40 micro-seconds.

Furthermore AE data was also plotted against the load data. In most cases AE events were recorded during crack closure and high amplitude AE events which may generate reflections were not present immediately before these events. Though the dataset has been filtered to exclude hits below 80 % of peak load, these AE events may still be due to friction between the fracture surfaces. The other potential source can be mechanical noise from the loading pins.

To minimize this noise, source location filtering (SLF) was employed. Only the events near the crack tip were extracted by using MATLAB code based on the source sensor distance and the sequence of the arrival time of the waveforms. The basic idea is that the closest sensors are triggered by the waveform first and vice-versa. After employing the SLF technique, the remaining hits and AE events are 2,241 and 334, respectively.

The source location based filtering technique possesses several advantages over other filtering methods, such as high sensitivity and ability to filter the crack related AE data located along the source of damage. Source localization is an important part of any monitoring process and can also be utilized as a filtering method. The other advantage of SLF method lies in the fact that the proper filtering algorithm can detect the real hits as they occur, that is, in real time for reduction of the unrelated AE data; whereas other filtering methods such as Swansong II filter are often customized to the dataset and are therefore employed after the data has been acquired. The sequence of arrival time (TOA) of AE waves is utilized based on the sensor location on the CT specimen and the location of the defect source is determined by minimizing the *Chi Squared* error function. More details of *Chi Squared* Error function can be found in literature (PAC 2004, ASNT 2005).

Moment tensor and b-value analysis was employed to assess the AE events associated with different failure mechanisms. According to Pollock (1981), a different failure mechanism results in distinct b-values. It is in the range of 0.7-1.5 for brittle fracture mechanisms in steel and can be as high as 2.0–4.0 for plastic deformation prior to crack extension in steel material. Based on the moment tensor analysis as discussed in previous section, b-value and visual inspection of waveforms, AE events associated with the fatigue crack extension (cleavage fractures) are extracted from the test data. This process is shown in Figures 6.9 through 6.11. All AE events associated with the tensile crack (brittle crack extension - cleavage fracture) are marked with a square bullet marker as shown in Figures 6.9 through 6.11.

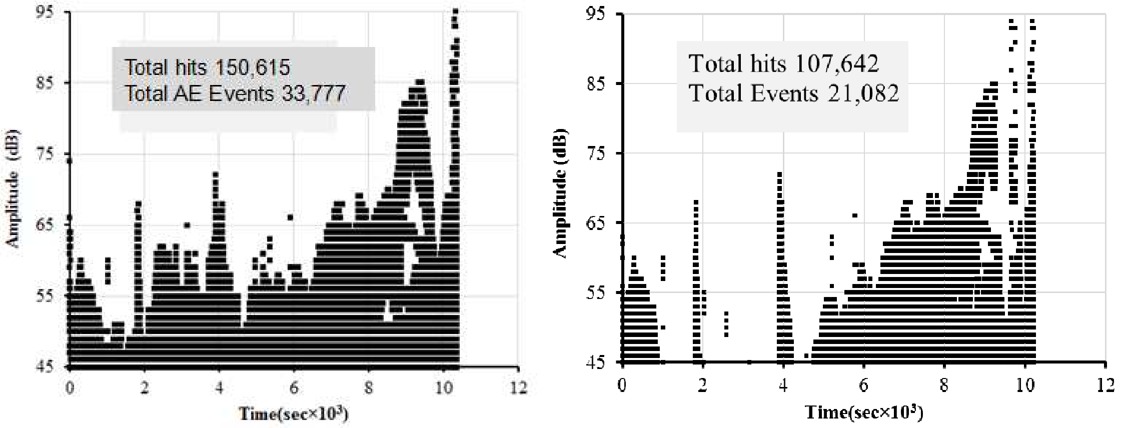

(a) **(b)**

Figure 6.8. Test results CT2: (a) AE hits without filter; (b) AE hits after 80% of peak load and Swangsong II filter.

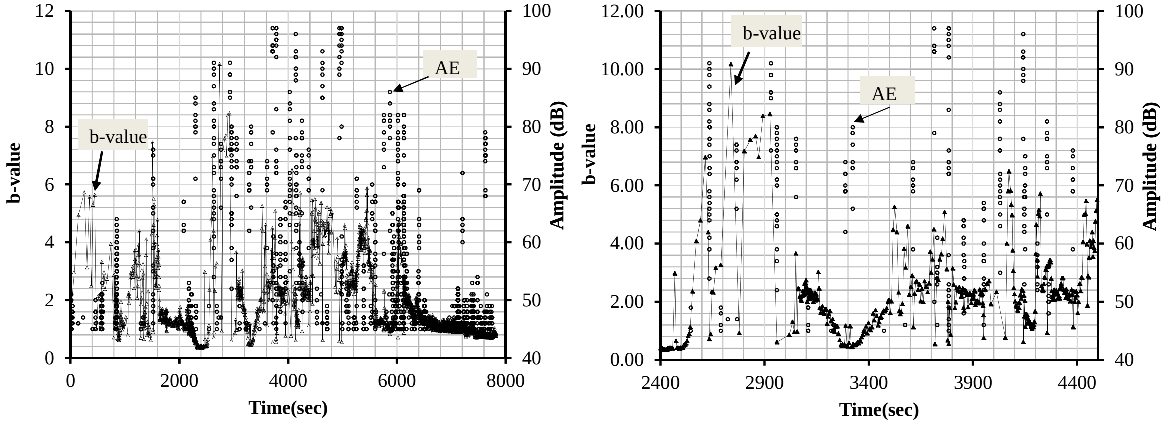

(a) **(b)**

Figure 6.9. Synchronization of b-value with AE data: (a) full data in CT specimen (CT1); (b) zoomed to extract AE events associated with brittle mechanism via b-value (CT1).

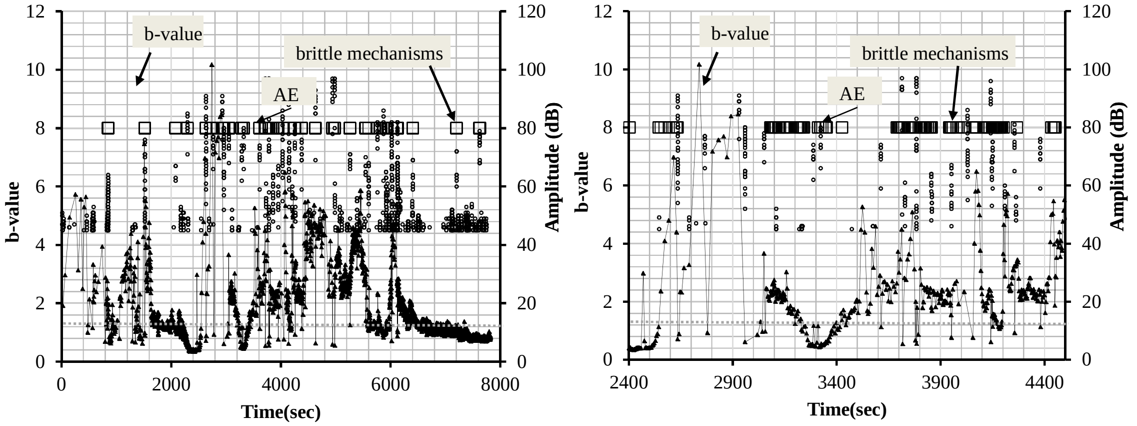

(a)

(b)

Figure 6.10. Synchronization of AE data with b-value and moment tensor: (a) full AE data; (b) zoomed to extract AE events associated with brittle mechanism.

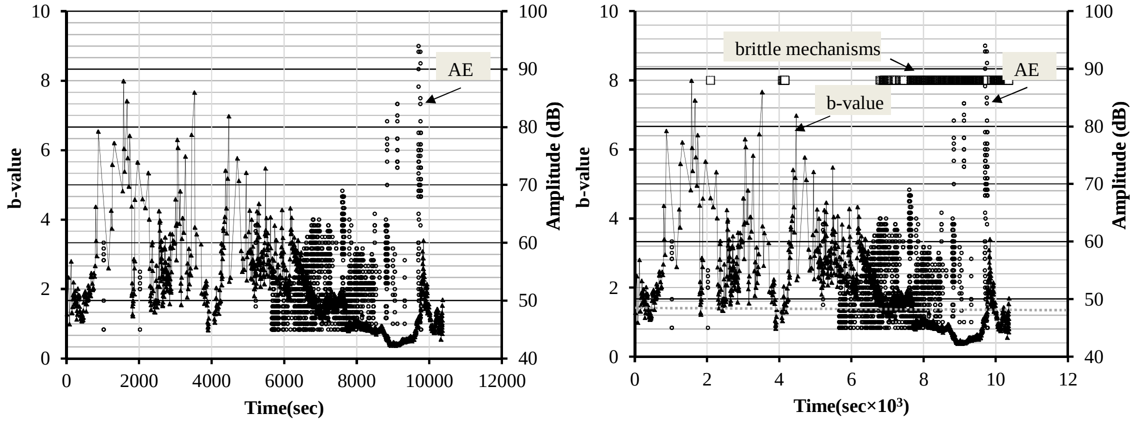

(a)

(b)

Figure 6.11. Synchronization of AE data: (a) AE data and b-value in CT specimen (CT2); (b) AE data, b-value and moment tensor analysis in CT specimen (CT2).

6.7 Part B: Probability of AE Detection

Several statistical forms including the Poisson distribution, Weibull distribution and the Gumbel distribution may be applied for Probability of Detection (POD) calculations (Pollock 2009). For the study described here, the Poisson distribution and Weibull distribution were utilized for POD calculations.

6.8 Weibull Distribution

The probability density function of a Weibull random variable is (Papoulis 1984):

$$f(x;\lambda,k)=\begin{cases}\dfrac{k}{\lambda}\left(\dfrac{x}{\lambda}\right)e^{-(x/\lambda)^k} & x\geq 0\\ 0 & x<0\end{cases} \tag{6.3}$$

where k > 0 is the shape parameter and λ > 0 is the scale parameter of the distribution. If the quantity x = the number of AE events associated with brittle failure, the Weibull distribution gives a distribution for which the brittle failure rate is proportional to a power of time. A value of k > 1 indicates that the failure rate increases with time. This happens if there is an "aging" process, or parts that are more likely to fail as time go on. Because the steel element subjected to fatigue damage will be fail after a certain period of time, and the rate of AE events increases with time, the Weibull distribution can be employed for POD calculation. The distribution function for the Weibull distribution is:

$$F(x;k,\lambda)=\begin{cases}1-e^{-(x/\lambda)^k} & x\geq 0\\ 0 & x<0\end{cases} \tag{6.4}$$

6.9 POISSON DISTRIBUTION

Moment tensor, b-value analysis of the AE events generated in the fatigue test leads directly to number of events associated with the highly emissive mechanisms. Then it will be a matter of statistics to determine the probability that at least one signal associated with brittle mechanisms that produce detectable acoustic emission. For simplicity, a Poisson distribution may be used to determine the expected number (x) of associated to brittle mechanisms, the probability of getting none associated to brittle mechanisms is e^{-x}. Consequently, the probability of getting at least one associated to brittle mechanisms is $(1 - e^{-x})$.

6.10 PROBABILITY OF CLEAVAGE FRACTURE

Beremin et al. (1983) developed the idea of cleavage fractures into a “weakest link” statistical model. According to this model a certain volume, V, of material ahead of the crack tip (usually the volume of the plastic zone) is assumed to have a distribution of microcracks of different lengths. Catastrophic failure is assumed to take place if a crack of critical length is found in this volume. This microcrack is a weakest link. It is assumed that the volume V can be divided into smaller volumes V_0, which must be big enough so that the probability of contains a microcrack of critical length is not negligible. At the same time V_0 must not be small enough for the assumption of a homogenous stress state over V_0 to be reasonable.

Thus the probability of existing microcrack:

$$\phi = 1-\exp\left[-\int_0^V \frac{1}{V_0}\int_0^\sigma g(a)da\right] \tag{6.5}$$

where g(a)da is the number of microcracks per volume V_0 with stresses required to propagate them between the crack length a and a+da. Usually a three-parameter Weibull probability distribution function (Weibull 1951) is used to express g(a)da:

$$\int_0^\sigma g(a)da = \left(\frac{\sigma_I - \sigma_{th}}{\sigma_u}\right)^m \tag{6.6}$$

where σ_I is a maximum principal stress in V_0, m is a shape parameter, σ_u is a scale parameter and σ_{th} is an offset parameter (a threshold stress) (shown in equation 6.8), required to propagate the largest feasible microcrack which can be given by equation (6.7):

$$\phi = 1-\exp[-(\sigma_w/\sigma_u)^m] \tag{6.7}$$

where,

$$\sigma_w = \left[\frac{1}{V_0}\int_0^\sigma (\sigma_I - \sigma_{th})\right]^{1/m} \tag{6.8}$$

where σ_w is called Weibull stress (Beremin et al. 1983). A progressive brittle fracture statistical model based on “chain-of-bundles” statistics (Gücer and Gurland 1962) was proposed by Ruggieri et al. (1995). In this model, several critical events are allowed before the catastrophic failure takes place. The analysis leads to Weibull statistics and effectively to the same relations as expressed by equations (6.7) and (6.8) (Ruggieri 1998). Other forms of equation can also be used. Kroon and Faleskog (2002) introduced the influence of applied strain on g(a)da and used an exponential distribution instead of Weibull (equation 6.9):

$$\int_0^{\sigma} g(a)da = c \cdot \varepsilon_{eq}^{p} \left(\exp\left[-\left(\frac{\sigma_m}{\sigma_I} \right)^2 \right] - \exp\left[-\left(\frac{\sigma_m}{\sigma_{th}} \right)^2 \right] \right) \tag{6.9}$$

where σ_m and c are material parameters and σ_m corresponds to the stress needed to propagate a mean size microcrack. In the model developed by Folch and others, the model assesses the onset of cleavage of each damage cell individually (Folch and Burdekin 1999, Folch et al. 1997). In other words the integration in equation (6.8) is performed over a volume of material within an individual cell. When the reference volume, V_0, is used as the cell volume and the threshold stress, σ_{th}, is equal to zero then the Weibull stress, σ_w, is the maximum principal stress. Therefore, equation (6.7) will have the following form:

$$\phi = 1 - \exp[-(\sigma_I / \sigma_u)^m] \tag{6.10}$$

where σ_I is a maximum principal stress, m is a shape parameter, and σ_u is a scale parameter which can be taken as three times the ultimate strength because of the tri-axiality effects at the crack tip. Hence, the probability of cleavage is based only on the ratio of the maximum principal stress to the scale parameter of a Weibull distribution.

In this approach the probability of cleavage of each cell can be calculated at the same time as its constitutive response. The cleavage initiation sites can now be identified and the brittle crack front can be obtained explicitly. Any model has to be calibrated for a particular material, so that model parameters can be considered true material properties. Instead of calibrating the model parameter, from equations (6.10) and (6.11), it can be seen that the probability of cleavage fracture increases with increasing the applied stress or strain as discussed earlier. Both equations can also be modified accordingly and employed for computing the probability of detectable AE events that may be generated during the fatigue crack growth.

The crack intensity factor is defined as:

$$K = \sigma Y \sqrt{\pi a} \tag{6.11}$$

where σ is a uniform tensile stress perpendicular to the crack plane, *Y* is a dimensionless parameter that depends on the geometry, and a is the crack length. The range of the stress intensity factor can be calculated using ASTM (2006) standard empirical equation as shown below and then stress, σ, can be evaluated at a specific crack length. A clip gage was used to record the crack mouth opening displacement (CMOD), ‘d’ (shown in Figure 6.2) and then the ASTM (2006) empirical expression was used to calculate the crack length, ‘a’ (from the center of the loading line, Figure 6.2). The empirical expression is:

$$\mathrm{a} = \mathrm{W}(1.001 - 4.6695u_x + 18.4u_x^2 - 236.82u_x^3 + 1214.9u_x^4 - 2143.6u_x^5) \tag{6.12}$$

where

$$u_x = \left[\sqrt{E \cdot t \cdot d / P_{\max}} + 1\right]^{-1} \tag{6.13}$$

where the effective width of the CT specimen (W) is 241.3 mm (9.5 inch) as shown in Figure 6.2 and the specimen thickness *t* is 12.7 mm (0.5 inch); the Young’s modulus *(E)* of ASTM A572 G50 steel is 200 GPa (29,000 ksi) and P_{max} is the peak of the cyclic load. The stress intensity range is determined by using the following equation (ASTM 2006):

$$\Delta K = \frac{\Delta P.(2+\alpha)}{tw^{1/2}(1-\alpha)^{3/2}}(0.886 + 4.64\alpha - 13.32\alpha^2 + 14.72\alpha^3 - 5.6\alpha^4) \tag{6.14}$$

where ΔP= P_{max}-P_{min} and α is equal to *a*/*W*. By using equation (6.14), the calculated critical crack length, a_c = 55.4 mm (2.18 inch) (from initial crack tip) when the maximum stress intensity at the crack tip reaches to 128 MPa√m (116.5 ksi√in).

From quantitative AE source characterization (moment tensor and b-value), AE events associated with brittle crack extension were assessed and plotted with time on the horizontal axis. For a specific time period of interest, the probability of detection of a brittle crack event can be determined as a function of the stress intensity range as shown in the following sections.

6.11 RESULTS AND DISCUSSION

From the AE data and b-values shown in Figures 6.9 through 6.11, the majority of the AE events are less energetic and the corresponding b-value is higher than 1.5. Hence, the fatigue crack growth is dominated by ductile mechanisms such as plastic deformation, inclusion disbonding, generation of microvoids, and ligament shearing between the microvoids. Therefore it can be considered that a large majority of the fractured surfaces are created by relatively quiet mechanisms such as microvoid coalescence. The total numbers of AE hits and events detected (defined as those crossing the threshold of 45) are 1,484 and 125 for CT1 and 2,241 and 334 for CT2, respectively. The amplitudes of these AE hits, AE events and corresponding moment tensor, and b-value distribution are shown in Figures 6.9 through 6.11. Therefore it is clear that only a fraction (ψ) of the total crack surfaces is associated with highly emissive mechanisms such as transgranular or intergranular cleavage. In this crack growth scenario, the fraction ψ is a key descriptor of material emissivity. At the beginning of the fatigue test, around a thousand cycles are required for receiving the first energetic AE event which may be associated with brittle mechanisms containing energetic acoustic emission. This high peak-amplitude is related to brittle crack propagation as determined through quantitative source characterization.

The detectability of AE also depends on the instrument threshold. Pollock (2010) used 50 dB as the threshold setting for similar AE monitoring to minimize noise in the data. In the experiments described here, the instrument threshold was set to 45 dB. Figures 6.9 through 6.11 show that brittle crack extension produces acoustic emission of amplitude larger than 65 dB. All sensor locations are close to the crack tip and therefore the attenuation problem is minimized even though the b-value is not significantly affected by attenuation.

The relationship between AE and brittle crack extension is screened through b-value and moment tensor analysis for both specimens and additionally through strain field monitoring with DIC in specimen CT2. At lower crack growth rates, defined as 1.9 × 10^{-3} mm/cycle (7.5 × 10^{-5} in/cycle) to 2.4 × 10^{-3} mm/cycle (9.5 × 10^{-5} in/cycle), several thousand cycles are generally required to obtain one energetic acoustic emission signal associated with brittle mechanisms associated with crack growth. At the higher crack growth rate, defined as 5.2 × 10^{-3} mm/cycle (2.1 × 10^{-4} in/cycle) to 2.9 × 10^{-2} mm/cycle (2.2 × 10^{-3} in/cycle), approximately one or two cycles are required for a valid event associated with a brittle mechanism. From a previous study (Pollock 2010), the probability of AE detection (POD) drops to 40-60% when the monitoring duration changed to 1,000 cycles instead of 2,000 cycles with the same initial flaw size. This result can be useful in developing an AE test, because it shows how the reliability of the detecting a brittle mechanism will depend on the duration of monitoring.

For the study described here, 2,000 cycles was employed as the AE monitoring duration in determining the probability of AE detection due to brittle mechanisms in this study. Once the AE events associated with highly emissive mechanisms are counted for

2,000 loading cycles, then statistical calculations give the probability of at least one AE event due to a brittle mechanism within this duration.

Figures 6.12 through 6.14 show the predicted probability of detecting a highly energetic, brittle, mechanism as a function of stress intensity range (ΔK) for 2,000 cycles of monitoring. With increasing crack severity, as determined by the cyclic stress intensity factor, *ΔK*, the rate of AE activity increased and thus the probability of AE detection associated with brittle mechanisms approaches 100% for 2,000 cycles of monitoring when the stress intensity range (*ΔK)* approaches 73 MPa√m (66.4 ksi√in) for CT1 as shown in Figure 6.12 (a) and 75 MPa√m (68.3 ksi√in) for CT2 as shown in Figure 6.12 (b) assuming a Poisson distribution. The same trend was also found for a Weibull distribution. For a Weibull distribution, the probability of AE detection associated with brittle mechanisms for 2,000 cycles of monitoring approaches 100% when the stress intensity range (*ΔK)* approaches 73 MPa√m (66.4 ksi√in) for CT1 as shown in Figure 6.13 (a) and 75 MPa√m (68.3 ksi√in) for CT2 as shown in Figure 6.13 (b).

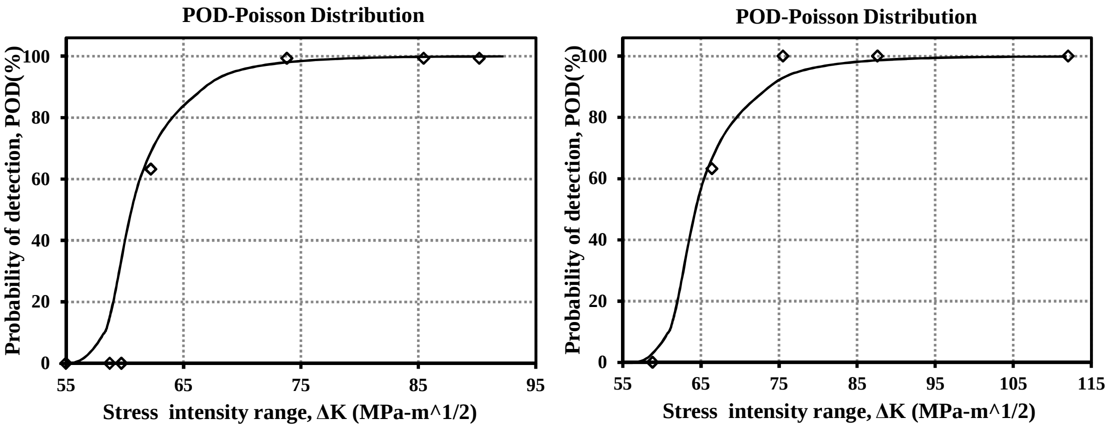

(a) (b)

Figure 6.12. Experimental results for probability of AE detection: (a) Specimen CT1; (b) Specimen CT2.

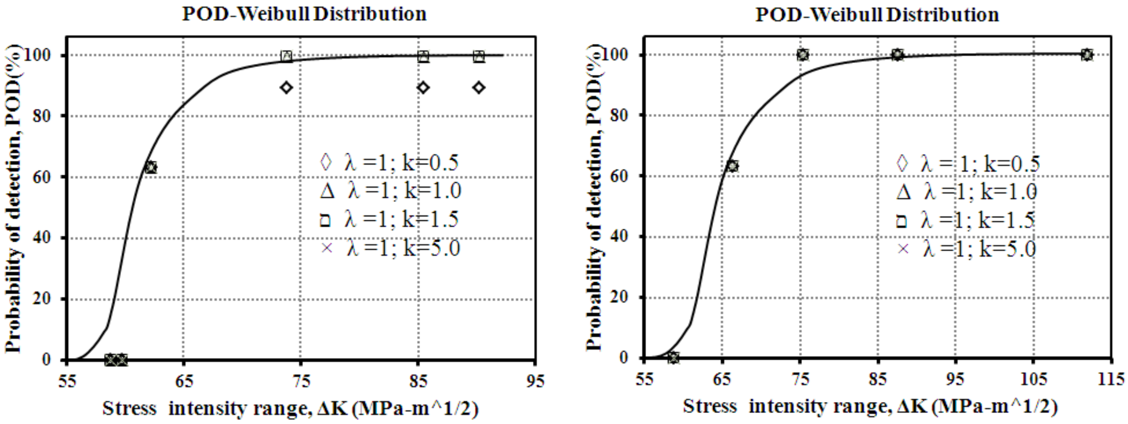

(a) (b)

Figure 6.13. Experimental results of probability of AE detection: (a) Specimen CT1; (b) Specimen CT2.

A comparison of POD between CT1 and CT2 is shown in Figure 6.14 (a). The Folch model [Figure 6.14(b)] also shows the same trend for probability of brittle crack extension. In this model, the probability of cleavage of each cell is calculated at the same time as its constitutive response. The cleavage initiation sites can now be identified and the brittle crack front can be obtained explicitly. Any statistical model has to be calibrated for a particular material, so that model parameters can be considered true material properties. Instead of calibrating the model parameter, if different m values such as 2.5, 4.0, 6.0 and 9.0 are considered and plotted (equation 6.9) with MATLAB (Matlab 2010), it can be seen that the probability of cleavage fracture increases with increasing applied stress as discussed earlier. The values of probability of detection associated with brittle cleavage fracture increases at a higher rate with the higher values of m. Both experimental plots and the plots obtained from equation 6.9 show similar trends in the probability of cleavage fracture and resulting acoustic emission.

The shape of both curves matches well. It is important to note that the x-axis of Figures 6.14 (a) and 6.14 (b) are not the same. The stress intensity range is used in Figure

6.14 (a) and the maximum principal stress is used in Figure 6.14 (b) along x-axis. However, the stress intensity range and stress at the crack tip are complementary and can be calculated by using equation (6.9). Both the experimentally obtained probability diagram and the Folch equation may also be utilized for computing the probability of detection based on AE for in-service steel bridges as the fatigue crack growth rate depends on the stress intensity range. For a particular loading condition and crack profile, stress intensity can be calculated and hence the probability of detection can be estimated even through it is limited to Mode I fatigue cracking at this time.

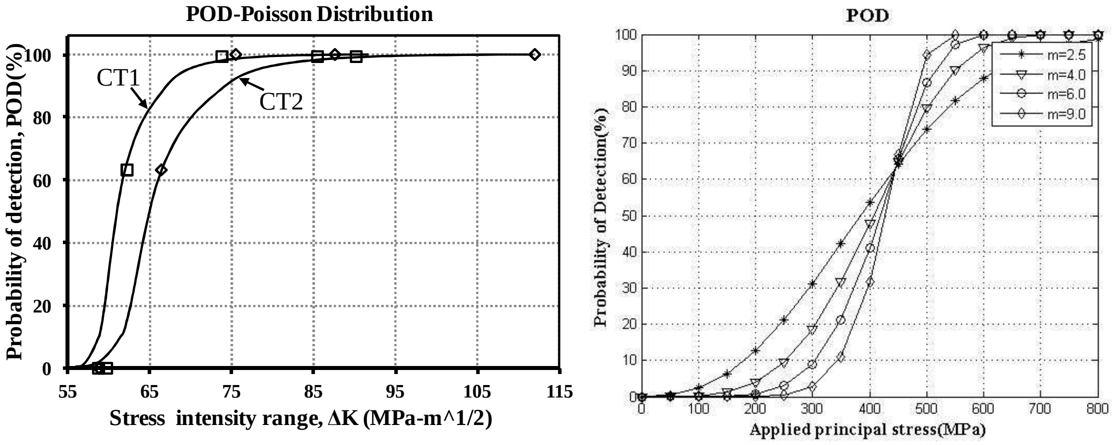

Figure 6.14. Probability of cleavage fracture based on: (a) experimental data; (b) Folch model

6.12 CONCLUSIONS

The objective of this study was to assess the probability of detection of mechanisms associated with crack growth based on AE monitoring during cyclic loading of steel bridge material (ASTM A572). Extensive source characterization of the acoustic emission was carried out using different quantitative techniques such as moment tensor and b-value to extract the highly energetic AE events related to the crack growth from other sources. Results show that ductile mechanisms such as plastic deformation and microvoid coalescence are dominant in the majority of the fatigue crack growth area and contribute to generate a large number of relatively small amplitude (around 50dB) AE signals. Only a small fraction of the total crack surface is associated with highly emissive mechanisms such as transgranular or intergranular cleavage that can be considered the key descriptor of emissivity in ASTM A572 Grade 50 steel. At higher stress levels the frequency of cleavage fracture increases which produces very energetic AE events. The following conclusions are drawn:

- Moment tensor and b-value are useful quantitative tools for extracting AE events associated with different mechanisms. However, in the case of moment tensor analysis a dense sensor array is required.
- Quantitative source characterization can provide insights to the source mechanisms and hence assist in assessing highly emissive AE events.
- Cleavage fracture (also referred to as tensile fracture) mechanisms produce highly energetic acoustic emission events. In contrast, ductile fracture mechanisms produce relatively low amplitude acoustic emission.
- Cleavage fracture occurs randomly. It increases with increasing stress intensity at the crack tip. At higher stress levels, the crack tip advances by intergranular cleavage fractures that produce relatively high amplitude acoustic emission.
- The probability of detection of acoustic emissions generated by brittle mechanisms increases with increased stress intensity and converges to 100% for duration of 2,000 loading cycles.

CHAPTER 7

SUMMARY AND CONCLUSIONS

The overall objective of this research study is to assess the probability of detection of fatigue crack extension based on acoustic emission in ATSM A572 G50 steel. This material is representative of materials widely used in the steel construction industry. The study consists of two main parts. The first part deals with assessing AE data of different failure mechanisms using fractographic analysis of scanning electronic microscope (SEM) images, synchronization of AE data with the strain field using digital image correlation (DIC), and data discrimination of AE events associated with highly emissive mechanisms. The second part is related to evaluation of the probability of detection using statistical approaches.

7.1 SUMMARY

The significant findings from the research are related to assessing AE events associated with different failure mechanisms during fatigue crack growth in A572 steel and assessing through experimental means the probability of detection associated with highly emissive mechanisms. The approach included AE data analysis, fractographic analysis of SEM images, moment tensor analysis for characterization of micro-level cracking phenomena, and characterization of corresponding AE signals.

The following conclusions can be drawn:

1. The raw AE data contains a significant portion of non-relevant AE hits from friction associated with crack closure (referred to in some instances as ‘fretting’) and mechanical noise. Therefore, it is imperative that proper data filtering be performed for structural health monitoring and assessment using the AE method.
2. Two governing mechanisms - ductile mechanisms and cleavage fracture - were present during fatigue crack growth in the ASTM A572 G50 steel used for this study.
3. Moment tensor analysis and b-value analysis can provide useful insight for assessing source mechanisms of AE events.
4. A key finding is that micro-void coalescence and plastic deformation do not generally produce high amplitude AE events for the steel bridge material investigated.
5. SEM fractographic analysis underpins the hypotheses formulated based on AE data analysis and confirms the failure mechanisms that have been reported to exist in ASTM A572 G50 steel.
6. For the duration used in this study, the probability of AE detection increases and slowly converges to 100% with increasing stress intensity range at the crack tip.

7.2 IMPLICATIONS FOR PRACTICE

The crack growth rate curve for ASTM A572 G50 steel can be divided into three main regions that are dependent on the stress intensity range. The stress intensity range is the main contributing factor that determines the cracking behavior. It encompasses all the parameters associated with fatigue crack behavior (i.e. load and geometry of the specimen). For a single cracked steel girder bridge (Mode I crack), the stress intensity range can be determined for a specific traffic load, crack length, and geometry of the structural element. Hence, the corresponding probability of detection based on AE data can be determined. Based on the probability of AE detection, bridge owners can set priorities of instrumentation (installation of AE sensors for structural health monitoring and assessment), repairs, and maintenance.

7.3 DIRECTIONS FOR FUTURE RESEARCH

1. Fatigue tests reported herein were conducted with constant amplitude cyclic loading. In real applications, however, the structure will experience varied service load cycles (due to passenger cars, trucks, and other vehicles). It is recommended that source mechanisms and the AE data from subsequent loadings be the focus of further studies.

2. A key component of this investigation was to study failure mechanisms at different stress intensity ranges. Fractographic analysis of SEM images was used to determine failure mechanisms in two CT specimens fabricated from structural A572 steel. Instead of studying a few cluster areas, a more detailed SEM observation should be conducted to more accurately identify failure mechanisms in a single point and associated AE events. Furthermore, SEM is limited to observation of failure mechanisms on the fractured surface of the specimens. Recently developed technology can perform the internal micro-structural observation. An example of such a technique is high resolution X-ray CT (computed tomography) (ASTM 1992).

3. Highly controlled experiments with specialized sensors and sensor arrays should be pursued to increase confidence related to source location of the AE events, particularly for the case of moment tensor analysis.
4. Modern statistical relationships between crack growth and AE events may be developed using AE, DIC, SEM, and other parametric data.
5. Further study of source mechanisms and associated acoustic emission when the sensors are placed near the crack tip is recommended to study the effects of the traveling medium by placing the sensor at different distances.
6. The probability of detection studied was limited to Mode-I fatigue cracking and only for the base metal. In reality fatigue cracking may initiate and grow in the weldment and further studies related to this case are recommended.

REFERENCES

Anderson, T. L. 2005. Fracture mechanics: fundamentals and applications: CRC Press.

Argon, A., and Im, J. 1975. Separation of second phase particles in spheroidized 1045 steel, Cu-0.6pct Cr alloy, and maraging steel in plastic straining. Metallurgical and Materials Transactions A, 6(4), 839-851.

Argon, A., Im, J., and Safoglu, R. 1975. Cavity formation from inclusions in ductile fracture. Metallurgical and Materials Transactions A, 6(4), 825-837.

American Society of Non Destructive Testing (ASNT). 2005. Nondestructive Testing Handbook, Third Edition: Volume 6, Acoustic Emission Testing, ed. P.O. Moore, 446.

American Society for Testing and Materials (ASTM).2006. Annual Book of ASTM Standard: section three-metals test methods and analytical procedures. ASTM International.

American Society for Testing and Materials (ASTM).1992. Standard Guide for Computed Tomography (CT) Imaging, ASTM Designation E 1441 - 92a. In: 1992 Annual Book of ASTM Standards, Section 3 Metals Test Methods and Analytical Procedures. ASTM, Philadelphia, pp. 690-713.

Bates, R.C. 1984. Fracture: interactions of microstructure, mechanisms and mechanics: Metallurgical Society of AIME.

Beachem, C. D. 1975. The effects of crack tip plastic flow directions upon microscopic dimple shapes. Metallurgical Transactions A 6, 377-383.

Beachem, C., D. 1963. An electron fractographic study of the influence of plastic strain conditions upon ductile rupture processes in metals. Transactions of the ASM, 56(3), 318-326.

Beremin, F., Pineau, A., Mudry, F., Devaux, J.-C., D'Escatha, Y., and Ledermann, P. 1983. A local criterion for cleavage fracture of a nuclear pressure vessel steel. Metallurgical and Materials Transactions A, 14(11), 2277-2287.

Bluhm, J. I., and Morrissery, R. J. 1966. Fracture in a tensile specimen. Proceedings of First International Conference on Fracture of Materials, Sendai, Japan.

Bridgman, P. W. 1952. Studies in large plastic flow and fracture with special emphasis on the effects of hydrostatic pressure: McGraw-Hill.

Carroll, J. 2011. Relating fatigue crack growth to microstructure via multiscale digital image correlation, University of Illinois at Urbana-Champaign.

Chauvot, C., and Sester, M. 2000. Fatigue crack initiation and crystallographic crack growth in an austenitic stainless steel. Computational materials science, 19(1), 87-96.

Cox, T. B., and Low, J. R. 1974. An investigation of the plastic fracture of AISI 4340 and 18 Nickel 200 grade maraging steels. Metallurgical Transactions 5, 1457-1470.

Curry, D. A., and Knott, J. F. 1978. Effects of microstructure on cleavage fracture stress in steel. Metal Science, 12(11), 511-514.

Davidson, D. L. 1984. A model for fatigue crack advance based on crack tip metallurgical and mechanics parameters. Acta Metallurgica, 32(5), 707-714.

El Bartali, A., Aubin, V., and Degallaix, S. 2008. Fatigue damage analysis in a duplex stainless steel by digital image correlation technique. Fatigue & Fracture of Engineering Materials & Structures, 31(2), 137-151.

Elbert, W. 1970. The significance of fatigue crack closure. Presented at Damage Tolerance in Aircraft Structures: A Symposium Presented at the Seventy-Third Annual Meeting American Society for Testing and Materials, Toronto, Ontario, Canada, 21-26 June 1970.

Ewing, J., and Humfrey, J. 1903. The fracture of metals under repeated alternations of stress. Philosophical Transactions of the Royal Society of London. Series A, Containing Papers of a Mathematical or Physical Character, 200, 241-250.

Folch, L. A., and Burdekin, F. M. 1999. Application of coupled brittle–ductile model to study correlation between Charpy energy and fracture toughness values. Engineering Fracture Mechanics, 63(1), 57-80.

Folch, L. C. A., and Burdekin, F. M. 1999. Application of coupled brittle–ductile model to study correlation between Charpy energy and fracture toughness values. Engineering Fracture Mechanics, 63(1), 57-80.

Folch, L. C. A.1997. Application of the Local Damage Mechanics Approach to Transition Temperature Behaviour in Steels: UMIST.

Garrison Jr, W. M., and Moody, N. R. 1987. Ductile fracture. Journal of Physics and Chemistry of Solids, 48(11), 1035-1074.

Giurgiutiu, V. 2007, Structural Health Monitoring: with Piezoelectric Active Sensors, Edition 08

Gladman, T. 1997. The physical metallurgy of microalloyed steels: Institute of Materials.

Gladman, T., Holmes, B., and McIvor, I. D. 1971. Effect of second-phase particles on the mechanical properties of steel: proceedings of a conference organized by the Corporate Laboratories of the British Steel Corporation and the Iron and Steel Institute, held at the Royal Hotel, Scarborough, on 24-25 March 1971: Iron and Steel Institute.

Gladman, T. 1997. The physical metallurgy of microalloyed steels: Institute of Materials.

Griffith, A. A. 1924. The theory of rupture. Presented at proceedings of the first international congress for applied mechanics, Delft.

Gücer, D. E., and Gurland, J. 1962. Comparison of the statistics of two fracture modes. Journal of the Mechanics and Physics of Solids, 10(4), 365-373.

Gurland, J. 1972. Observations on the fracture of cementite particles in a spheroidized 1.05% c steel deformed at room temperature. Acta Metallurgica, 20(5), 735-741.

Gurland, J., and Plateau, J. 1963. The Mechanism of Ductile Rupture of Metals Containing Inclusions.

Gurson, A. L. 1977. Continuum Theory of Ductile Rupture by Void Nucleation and Growth: Part I---Yield Criteria and Flow Rules for Porous Ductile Media. Journal of Engineering Materials and Technology, 99(1), 2-15.

Hahn, G. T., Averbach, B. L., Owen, W. S., and Cohen, M. 1959. Initiation of cleavage microcracks in polycrystalline iron and steel, in Averbach et al. 1959 City, 91-116.

Hamstad, M. A., and McColskey, J. D. 1999. Detectability of Slow Crack Growth in Bridge Steels by Acoustic Emission. Materials Evaluation, 57(11), 1165-1174.

Hoshide, T., and Socie, D. 1988. Crack nucleation and growth modeling in biaxial fatigue. Engineering fracture mechanics, 29(3), 287-299.

Hossain, M., Yu, J., Ziehl, P., Caicedo, J., Matta, F., Guo, S., and Sutton, M. 2013. Acoustic emission source mechanisms for steel bridge material. AIP Conference Proceedings, 1511(1), 1378-1384.

Hossain, M., Ziehl, P., Yu, J., Caicedo, J., and Matta, F. 2012. Source Mechanisms of Acoustic Emission during Fatigue Crack Growth in Steel Bridge Material. Proc. 5th European Conference on Structural Control (EACS 2012), June 18-20, 2012, Genoa, Italy, Paper 158, 7 p.

Huang, Y., Hutchinson, J. W., and Tvergaard, V. 1991. Cavitation instabilities in elastic-plastic solids. Journal of the Mechanics and Physics of Solids, 39(2), 223-241.

Jonnalagadda, K., Karanjgaokar, N., Chasiotis, I., Chee, J., and Peroulis, D. 2010. Strain rate sensitivity of nanocrystalline Au films at room temperature. Acta Materialia, 58(14), 4674-4684.

Kroon, M., and Faleskog, J. 2002. A probabilistic model for cleavage fracture with a length scale-influence of material parameters and constraint. International Journal of Fracture, 118(2), 99-118.

Laird, C., and Smith, G. C. 1963. Initial stages of damage in high stress fatigue in some pure metals. Philosophical Magazine, 8(95), 1945-1963.

Lambros, J., and Patel, J. 2011. Microscale digital image correlation study of irradiation induced ductile-to-brittle transition in polyethylene. The Journal of Strain Analysis for Engineering Design, 46(5), 347-360.

Lankford, J., and Davidson, D. L. 1983. Fatigue crack micromechanisms in ingot and powder metallurgy 7xxx aluminum alloys in air and vacuum. Acta Metallurgica, 31(8), 1273-1284.

Lin, T., Evans, A. G., and Ritchie, R. O. 1987. Stochastic modeling of the independent roles of particle size and grain size in transgranular cleavage fracture. Metallurgical Transactions A, 18(5), 641-651.

Liu, C. T., and Gurland, J. 1968. The fracture behaviour of spheroidized carbon steels. Transactions of the ASM, 61, 156-167.

Magnin, T., Coudreuse, L., and Lardon, J. 1985. A quantitative approach to fatigue damage evolution in FCC and BCC stainless steels. Scripta metallurgica, 19(12), 1487-1490.

Matlab, v. (2010). The MathWorks Inc. Natick, MA, USA.

McClintock, F. A. 1968. A criterion for ductile fracture by the growth of voids. Journal of Applied Mechanics, 35, 363-371.

McMahon Jr, C. J., and Cohen, M. 1965. Initiation of cleavage in polycrystalline iron. Acta Metallurgica, 13(6), 591-604.

Morris, W., James, M., and Zurek, A. 1985. The extent of crack tip plasticity for short fatigue cracks. Scripta Metallurgica, 19, 149-153.

Ochi, Y., Ishii, A., and Sasaki, S. 1985. An experimental and statistical investigation of surface fatigue crack initiation and growth. Fatigue & fracture of engineering materials & structures, 8(4), 327-339.

Ohira, T., and Pao, Y.-H. 1986. Microcrack initiation and acoustic emission during fracture toughness tests of A533B steel. Metallurgical and Materials Transactions A, 17(5), 843-852.

Papoulis, A. 1984. Probability, Random Variables, and Stochastic Processes: McGraw-Hill.

Peralta, P., Choi, S., and Gee, J. 2007. Experimental quantification of the plastic blunting process for stage II fatigue crack growth in one-phase metallic materials. International Journal of Plasticity, 23, 1763-1795.

Pollock, A. 1981. Acoustic emission amplitude distributions. International Advances in Nondestructive Testing, 7, 215-239.

Pollock, A. 2010. A POD Model for Acoustic Emission- Discussion and Status. AIP Conference Proceedings, 1211(1), 1927-1933.

Puttick, K. E. 1959. Ductile fracture in metals. Philosophical Magazine, 4(44), 964-969.

Rice, J. R. and Tracey, D. M. 1969. On the ductile enlargement of voids in triaxial stress. Journal of the Mechanics and Physics of Solids, 17, 201-217.

Ritchie, R. O., Knott, J. F., and Rice, J. R. 1973. On the relationship between critical tensile stress and fracture toughness in mild steel. Journal of the Mechanics and Physics of Solids, 21(6), 395-410.

Rogers, H. C. 1960. Tensile fracture of ductile metals. Transactions of the Metallurgical Society of AIME 218, 498-506.

Ruggieri, C. 1998. Probabilistic treatment of fracture using two failure models. Probabilistic Engineering Mechanics, 13(4), 309-319.

Ruggieri, C. 2004. Numerical investigation of constraint effects on ductile fracture in tensile specimens. Journal of the Brazilian Society of Mechanical Sciences and Engineering, 26, 190-199.

Ruggieri, C., Minami, F., and Toyoda, M. 1995. A Statistical Approach for Fracture of Brittle Materials Based on the Chain-of-Bundles Model. Journal of Applied Mechanics, 62(2), 320-328.

Scruby, C. B. 1987. An introduction to acoustic emission. Journal of Physics E: Scientific Instruments, 20(8), 946.

Shen, H. W., Finlayson, R. D., and Miller, R. K. 2001. Moment tensor study on small dimensioned concrete beam. AIP Conference Proceedings, 557(1), 1179-1185.

Smith, E. 1966. The formation of a cleavage crack in a crystalline solid-I. Acta Metallurgica, 14(8), 985-989.

Stephens, R. I., Lee, S. G., and Lee, H. W. 1982. Constant and variable amplitude fatigue behavior and fracture of A572 steel at 25°C (77°F) and −45°C (−50°F). International Journal of Fracture, 19(2), 83-98.

Sutton, M. A., Orteu, J.-J., and Schreier, H. 2009. Image Correlation for Shape, Motion and Deformation Measurements: Basic Concepts, Theory and Applications: Springer Publishing Company, Incorporated.

Sutton, M. A., Wolters, W. J., Peters, W. H., Ranson, W. F., and McNeill, S. R. 1983. Determination of displacements using an improved digital correlation method. Image and Vision Computing, 1(3), 133-139.

Sutton, M. A., Zhao, W., McNeill, S. R., Helm, J. D., Piascik, R. S., and Riddell, W. T. 1999. Local crack closure measurements: Development of a measurement system using computer vision and a far-field microscope. ASTM Special Technical Publication, 1343, 145-156.

Thomason, P. F. 1968. A theory for ductile fracture by internal necking of cavities. Journal of the Institute of Metals, 96, 360-365.

Thomason, P. F. 1981. Ductile fracture and the stability of incompressible plasticity in the presence of microvoids. Acta Metallurgica, 29(5), 763-777.

Thomason, P. F. 1990. Ductile fracture of metals: Pergamon Press.

Thomason, P. F. 1993. Ductile fracture by the growth and coalescence of microvoids of non-uniform size and spacing. Acta Metallurgica et Materialia, 41(7), 2127-2134.

Thomason, P. F. 1998. A view on ductile-fracture modeling. Fatigue & Fracture of Engineering Materials & Structures, 21(9), 1105-1122.

Thompson, A., and Knott, J. 1993. Micromechanisms of brittle fracture. Metallurgical and Materials Transactions A, 24(3), 523-534.

Tipper, C. F. 1949. The Fracture of Metals. Metallurgia, 39, 133-137.

Weertman, J. 2007. Dislocation crack tip shielding and the Paris exponent. Materials Science and Engineering: A, 468–470(0), 59-63.

Weibull, W. 1951. A statistical distribution function of wide applicability. Journal of Applied Mechanics, 18, 293-297.

Yu, J., Ziehl, P., Zárate, B., and Caicedo, J. 2011. Prediction of fatigue crack growth in steel bridge components using acoustic emission. Journal of Constructional Steel Research, 67(8), 1254-1260.

Parmar, D. S., and Sharp, S. R.2009. Acoustic Emission for Non-Destructive Testing of Bridges and other Transportation Infrastructure. A National Conference on Transportation Infrastructure & Regulatory Policy, Denver, CO

APPENDIX A – MATLAB CODE

A. MATLAB Codes

A1. MATLAB Code for DIC Filtering

```
clear all; clc; close all; format long

%*************************************
cd('F:\DIC_mozahid\civill-120min\results');
[num txt raw]=xlsread('2000-8998circleat4001.xlsx');
i=2001;% starting line number
j=2500;% Ending line number
index = i:5:6976;
%***************************************

time= num(:,5);
ctime=time;
strain=100*num(:,2);
%length(num);

x=ctime(index);
y= strain(index);
figure
plot(x, y, 'ko')
ylim([0 10])
xlabel('Time(Sec)','FontWeight','bold','FontSize',12,...
    'FontName','Times New Roman')
ylabel('Strain eyy(%)','FontWeight','bold','FontSize',12,...
    'FontName','Times New Roman')
title('Strain eyy','FontWeight','bold','FontSize',14,...
    'FontName','Times New Roman');
data=([x, y]);
grid on
index1 = i+1:5:j;
x1=ctime(index1);
y1= strain(index1);
figure
plot(x1, y1, 'ko')
ylim([0 10])
```

```
xlabel('Time(Sec)','FontWeight','bold','FontSize',12,...
   'FontName','Times New Roman')
ylabel('Strain eyy(%)','FontWeight','bold','FontSize',12,...
   'FontName','Times New Roman')
title('Strain eyy','FontWeight','bold','FontSize',14,...
   'FontName','Times New Roman');
data1=([x1, y1]);
grid on
index2 = i+2:5:j;
x2=ctime(index2);
y2= strain(index2);
figure
plot(x2, y2, 'ko')
ylim([0 10])
xlabel('Time(Sec)','FontWeight','bold','FontSize',12,...
   'FontName','Times New Roman')
ylabel('Strain eyy(%)','FontWeight','bold','FontSize',12,...
   'FontName','Times New Roman')
title('Strain eyy','FontWeight','bold','FontSize',14,...
   'FontName','Times New Roman');
data2=([x2, y2]);
grid on
index3 = i+3:5:j;
x3=ctime(index3);
y3= strain(index3);
figure
plot(x3, y3, 'ko')
ylim([0 10])
xlabel('Time(Sec)','FontWeight','bold','FontSize',12,...
   'FontName','Times New Roman')
ylabel('Strain eyy(%)','FontWeight','bold','FontSize',12,...
   'FontName','Times New Roman')
title('Strain eyy','FontWeight','bold','FontSize',14,...
   'FontName','Times New Roman');
data3=([x3, y3]);
grid on
index4 = i+4:5:j;
x4=ctime(index4);
y4= strain(index4);
figure
plot(x4, y4, 'ko')
ylim([0 10])
xlabel('Time(Sec)','FontWeight','bold','FontSize',12,...
   'FontName','Times New Roman')
ylabel('Strain eyy(%)','FontWeight','bold','FontSize',12,...
   'FontName','Times New Roman')
```

```
title('Strain eyy','FontWeight','bold','FontSize',14,...
    'FontName','Times New Roman');
data4=([x4, y4]);
grid on

datacom=([x1, y1, x2, y2, x3, y3, x4, y4]);
```

A2. MATLAB CODE FOR B-VALUE CALCULATION

```
clear;
clc;
close all
grid on
files = dir('*.mat');
if isempty(files)
%data_ae = load('fulldata.dat');
data_ae = load('fulldata80.dat');
save('savedvariables.mat');
else
load('savedvariables.mat');
end
chh = 1;
dd_1 = data_ae(data_ae(:,5)==chh,:);
A_1 = [dd_1(:,2),dd_1(:,7)];
figure(1)
plot(A_1(:,1),A_1(:,2),'.k');
xlabel('Time(sec)','FontSize',12);
ylabel('Amplitude, dB','FontSize',12)
title('Amplitude distribution: CHANNEL 1','FontSize',14)
chh = 2;
dd_2 = data_ae(data_ae(:,5)==chh,:);
A_2 = [dd_2(:,2),dd_2(:,7)];
figure(2)
plot(A_2(:,1),A_2(:,2), 'ok');
xlabel('Time(sec)','FontSize',12);
ylabel('Amplitude, dB','FontSize',12)
title('Amplitude distribution: CHANNEL 2','FontSize',14)
chh = 3;
dd_3 = data_ae(data_ae(:,5)==chh,:);
A_3 = [dd_3(:,2),dd_3(:,7)];
figure(3)
plot(A_3(:,1),A_3(:,2),'.k');
xlabel('Time(sec)','FontSize',12);
ylabel('Amplitude, dB','FontSize',12)
title('Amplitude distribution: CHANNEL 3','FontSize',14)
chh = 4;
dd_4 = data_ae(data_ae(:,5)==chh,:);
A_4 = [dd_4(:,2),dd_4(:,7)];
figure(4)
plot(A_4(:,1),A_4(:,2),'.k');
xlabel('Time(sec)','FontSize',12);
ylabel('Amplitude, dB','FontSize',12)
```

```
title('Amplitude distribution: CHANNEL 4','FontSize',14)
chh = 5;
dd_5 = data_ae(data_ae(:,5)==chh,:);
A_5 = [dd_5(:,2),dd_5(:,7)];
figure(5)
plot(A_5(:,1),A_5(:,2),'.k');
xlabel('Time(sec)','FontSize',12);
ylabel('Amplitude, dB','FontSize',12)
title('Amplitude distribution: CHANNEL 5','FontSize',14)
chh = 6;
dd_6 = data_ae(data_ae(:,5)==chh,:);
A_6 = [dd_6(:,2),dd_6(:,7)];
figure(6)
plot(A_6(:,1),A_6(:,2),'.k');
xlabel('Time(sec)','FontSize',12);
ylabel('Amplitude, dB','FontSize',12)
title('Amplitude distribution: CHANNEL 6','FontSize',14)
chh = 7;
dd_7 = data_ae(data_ae(:,5)==chh,:);
A_7 = [dd_7(:,2),dd_7(:,7)];
figure(7)
plot(A_7(:,1),A_7(:,2),'.k');
xlabel('Time(sec)','FontSize',12);
ylabel('Amplitude, dB','FontSize',12)
title('Amplitude distribution: CHANNEL 7','FontSize',14)
chh = 8;
dd_8 = data_ae(data_ae(:,5)==chh,:);
A_8 = [dd_8(:,2),dd_8(:,7)];
figure(8)
plot(A_8(:,1),A_8(:,2),'.k');
xlabel('Time(sec)','FontSize',12);
ylabel('Amplitude, dB','FontSize',12)
title('Amplitude distribution: CHANNEL 8','FontSize',14)
figure (9)
plot(A_1(:,1),A_1(:,2), 'ok');
hold on
plot(A_2(:,1),A_2(:,2), '.m');
hold on
plot(A_3(:,1),A_3(:,2), '*y');
hold on
plot(A_4(:,1),A_4(:,2), '.r');
hold on
plot(A_5(:,1),A_5(:,2), '.g');
hold on
plot(A_6(:,1),A_6(:,2), '.b');
hold on
```

```
plot(A_7(:,1),A_7(:,2), '.k');
hold on
plot(A_8(:,1),A_8(:,2), '.g')
legend('Channel 1','Channel 2','Channel 3','Channel 4','Channel 5','Channel 6','Channel 7','Channel 8')
xlabel('Time(sec)','FontSize',12)
ylabel('Amplitude, dB','FontSize',12)
title('Amplitude distribution: CHANNEL ALL','FontSize',14)
figure (10)
subplot(3,3,1); plot(A_1(:,1),A_1(:,2), '.k')
axis([0 25000 40 100])
%subplot(m,n,p: m-by-n matrix of small subplots and selects the pth subplot
xlabel('Time(sec)','FontSize',12)
ylabel('Amplitude, dB','FontSize',12)
title('Amplitude distribution: CHANNEL 1','FontSize',14)
subplot(3,3,2); plot(A_2(:,1),A_2(:,2), '.k')
axis([0 25000 40 100])
xlabel('Time(sec)','FontSize',12)
ylabel('Amplitude, dB','FontSize',12)
title('Amplitude distribution: CHANNEL 2','FontSize',14)
subplot(3,3,3); plot(A_3(:,1),A_3(:,2), '.k')
axis([0 25000 40 100])
xlabel('Time(sec)','FontSize',12)
ylabel('Amplitude, dB','FontSize',12)
title('Amplitude distribution: CHANNEL 3','FontSize',14)
subplot(3,3,4); plot(A_4(:,1),A_4(:,2), '.k')
axis([0 25000 40 100])
xlabel('Time(sec)','FontSize',12)
ylabel('Amplitude, dB','FontSize',12)
title('Amplitude distribution: CHANNEL 4','FontSize',14)
subplot(3,3,5); plot(A_5(:,1),A_5(:,2), '.k')
axis([0 25000 40 100])
xlabel('Time(sec)','FontSize',12)
ylabel('Amplitude, dB','FontSize',12)
title('Amplitude distribution: CHANNEL 5','FontSize',14)
subplot(3,3,6); plot(A_6(:,1),A_6(:,2), '.k')
axis([0 25000 40 100])
xlabel('Time(sec)','FontSize',12)
ylabel('Amplitude, dB','FontSize',12)
title('Amplitude distribution: CHANNEL 6','FontSize',14)
subplot(3,3,7); plot(A_7(:,1),A_7(:,2), '.k')
axis([0 25000 40 100])
xlabel('Time(sec)','FontSize',12)
ylabel('Amplitude, dB','FontSize',12)
title('Amplitude distribution: CHANNEL 7','FontSize',14)
subplot(3,3,8); plot(A_8(:,1),A_8(:,2), '.k')
```

```
axis([0 25000 40 100])
xlabel('Time(sec)','FontSize',12)
ylabel('Amplitude, dB','FontSize',12)
title('Amplitude distribution: CHANNEL 8','FontSize',14)
```

A3. MATLAB CODE FOR AE EVENTS DETERMINATION

```
clear all; clc;close all; format long
cd('E:\DIC_mozahid\Mozahid_CT2_April12\AE data_SM2');
[num txt raw]=xlsread('sm2fulldata.xlsx','sm2_aPRIL12_2012_fulldata');
time = num(:,2);
ch = num(:,5);
format long
dt = [0; diff(time)];
sprintf('%.20f', dt)
%fprintf('value of b is %1.10e\n',dt)
event = [];
ii=0; nx = size(num,1);
idx = true(nx,1);
maxnumsensor = 8;
maxdt = 2e-5;
while any(idx)
ii=ii+1;
tidx = find(idx,maxnumsensor,'first');
dtt = [0; diff(time(tidx))];
nev = find(~(dtt<=maxdt),1,'first');
if isempty(nev)
nev = length(dtt)+1;
end
idx2 = 1:nev-1;
event = [event; ii*ones(length(idx2),1)];
tidx = tidx(idx2);
idx(tidx)=false;
fprintf('Looking for event %i\n',ii);
end
%% Organizes events and times
numevents = max(event);
format long
kk=0; dt=[];
maxdt = 2e-5;
for ii=1:numevents
idx = event==ii;
t = nan(1,8);
tt = time(idx);
chs = ch(idx);
[chs indx] = sort(chs);
tt = tt(indx);
t(chs) = tt;
% Time difference between ch1 and ch5
dt15 = abs(t(1)-t(5));
% Time difference between ch2 and ch4
```

```
dt24 = abs(t(2)-t(4));
cond = [dt15 dt24]<maxdt;
if all(cond)
kk=kk+1;
format long
dt(kk,:) = [ii t];
end
end
```

A4. SOURCE LOCATION PLOT

```
clear all; clc; close all
cd('E:\PLB_1inchthickplate\CT_speedcal_6sensors_glue');
[num txt raw]=xlsread('errorcal.xlsx','time');
% values to change
v=200; % Row to read from excel file
sensid = [1 2 4 5 ]; % to change
refs = 1; % sensor reference from sensid-1st one:1; 2nd one:2; 3rd:3
%
time = num(v,:);
xysensor = [3.75    0; 0    3; 0    6; 0    9; 3.75 12; 4.783   6];
tt = time(sensid);
%c = 220000;
%c = 150000;
%c = 110000;
c = 9000;
x = linspace(0,11.917,121);
y = linspace(0,12,121);
[X Y]=meshgrid(x,y);
X=X(:);
Y=Y(:);
tr = time(sensid(refs));
dto = tt-tr;
dtc = [];
x2r = xysensor(sensid(refs),1);
y2r = xysensor(sensid(refs),2);
chi2 = [];
for ii=1:length(sensid)
xr = xysensor(sensid(ii),1);
yr = xysensor(sensid(ii),2);
dtc=[dtc (sqrt((X-xr).^2+(Y-yr).^2)-sqrt((X-x2r).^2+(Y-y2r).^2))/c];
end
chi2=sum((dtc-repmat(dto,size(dtc,1),1)).^2,2);
C2 = reshape(chi2,length(x),length(y));
figure1 = figure('Color',[1 1 1]);
contourf(x,y,C2, 100);
minf=10;for i=1:size(C2,1)*size(C2,2);minf=min(C2(i),minf);end
[x1,y1,minf1]=find(C2==minf);
text(x(y1),y(x1),'*\leftarrow PLB','FontSize',22,'Color', 'g')
colorbar('location','eastoutside')
xlabel('X Position(inch)','FontWeight','bold','FontSize',12,...
'FontName','Times New Roman')
ylabel('Y Position(inch)','FontWeight','bold','FontSize',12,...
'FontName','Times New Roman')
title('Error in Surce Location for Gr2:Ch1,2,4,5','FontWeight','bold','FontSize',14,...
```

```
'FontName','Times New Roman');
figure1 = figure('Color',[1 1 1]);
surf(x,y,C2,'edgecolor','none');
text(x(y1),y(x1),'*\leftarrow PLB','FontSize',22,'Color', 'g')
%surf(x,y,C2);
colorbar('location','eastoutside')
xlabel('X Position(inch)','FontWeight','bold','FontSize',12,...
'FontName','Times New Roman')
ylabel('Y Position(inch)','FontWeight','bold','FontSize',12,...
'FontName','Times New Roman')
title('Error in Surce Location for Gr2:Ch1,2,4,5','FontWeight','bold','FontSize',14,...
'FontName','Times New Roman');
```

A5. DIC PLOT

```
clear all; clc;close all;
cd('F:\DIC_mozahid\civill-60min\Results');
[num txt raw]=xlsread('60alldata1stpoint.xlsx');
for i=1:1800-1
    t(i)=i;
    st(i)=max(num(5*(i-1)+1:5*i,9));
    stm(i)=min(num(5*(i-1)+1:5*i,9));

end
strain=st';
time =t';
figure1 = figure('Color',[1 1 1]);
plot (t, st,'ko', t,stm,'k.')
%ylim([4 15])
xlabel('Time(Sec)','FontWeight','bold','FontSize',12,...
    'FontName','Times New Roman')
ylabel('Strain eyy(%)','FontWeight','bold','FontSize',12,...
    'FontName','Times New Roman')
title('Strain eyy','FontWeight','bold','FontSize',14,...
    'FontName','Times New Roman');
data=([time, strain]);
grid on
```

A6. SOURCE LOCATION BASED FILTER OF AE DATA

```
clear all; clc;close all; format long
cd('F:\DIC_mozahid\Mozahid_CT2_April12');
[num txt raw]=xlsread('sm2_aPRIL12_2012_fulldata.xlsx');
%[num txt raw]=xlsread('plb25flt25.xlsx','plb25');
%[num txt raw]=xlsread('sm2fulldata25.xlsx','sm2_aPRIL12_fulldata');
time = num(:,2);
ch = num(:,5);
format long
dt = [0; diff(time)];
sprintf('%.20f', dt)
%fprintf('value of b is %1.10e\n',dt)
event = [];
ii=0; nx = size(num,1);
idx = true(nx,1);
maxnumsensor = 8;
maxdt = 2e-2;
while any(idx)
  ii=ii+1;
  tidx = find(idx,maxnumsensor,'first');
  dtt = [0; diff(time(tidx))];
  nev = find(~(dtt<=maxdt),1,'first');
  if isempty(nev)
     nev = length(dtt)+1;
  end
  idx2 = 1:nev-1;
  event = [event; ii*ones(length(idx2),1)];
  tidx = tidx(idx2);
  idx(tidx)=false;
  fprintf('Looking for event %i\n',ii);
end

%%
%%filter based on channel sequences(3,1,2,4,5)

numevents = max(event);
format long
kk=0; dt=[];
for ii=1:numevents
  idx = event==ii;
  t = nan(1,8);
  tt = time(idx);
  chs = ch(idx);
  [chs indx] = sort(chs);
  tt = tt(indx);
```

```
    t(chs) = tt;
    % Time difference between ch1 and ch5
    dt31 = t(3)-t(1);
      % Time difference between ch2 and ch4
    dt32 = t(3)-t(2);
    dt34 = t(3)-t(4);
    dt35 = t(3)-t(5);
      cond = [dt31 dt32 dt34 dt35]<0;
    if all(cond)
        kk=kk+1;
        format long
        dt(kk,:) = [ii t];
        dtb(kk,:)=[t];
    end
end
X = dt(: , 2:9);
B = X( : );
b= B';
%%
dramin=nan(size(dt));
dramin(:,1)=dt(:,1);
for j=2:9
    for i=1:size(dt,1)
        [row,col,v]=find(num==dt(i,j));
        if size(row,1)~=0
            dramin(i,j)=num(row(1),7);
        else
            dramin(i,j)=nan;
        end
    end
end

%plot(dt(:,3),dramin(:,3),'ko')
%plot(dt(:,2),dramin(:,2),'ko')
%plot(dt(:,2),dramin(:),'ko')

figure1 = figure('Color',[1 1 1]);
hold on
for iii = 2:9
 plot(dt(:,iii),dramin(:,iii),'ko')
 %xydat = [dt(:,iii),dramin(:,iii)];
end
xlabel('Time(Sec)','FontWeight','bold','FontSize',12,...
    'FontName','Times New Roman')
ylabel('Amplitude (dB)','FontWeight','bold','FontSize',12,...
    'FontName','Times New Roman')
```

```
title('Amplitude vs Time','FontWeight','bold','FontSize',14,...
   'FontName','Times New Roman');
grid on
dtx2=dt(: , 2:9);
dty2=dramin(: , 2:9);
x2=dtx2(:);
y2=dty2(:);
xydat = [x2, y2];
%% Organizes events and times
numevents = max(event);
format long
kk=0; dt=[];
%maxdt = 7.72727273e-6;
%maxdt = 8.63636364e-6;
%maxdt = 9.54545455e-6;
maxdt = 20.45454545e-6;

for ii=1:numevents
  idx = event==ii;
  t = nan(1,8);
  tt = time(idx);
  chs = ch(idx);
  [chs indx] = sort(chs);
  tt = tt(indx);
  t(chs) = tt;
  % Time difference between ch1 and ch5
  %dt51 = abs(t(1)-t(5));
  % Time difference between ch3 and ch2
  dt23 = abs(t(3)-t(2));
  % Time difference between ch3 and ch4
  dt43 = abs(t(3)-t(4));
  % Time difference between ch2 and ch4
  dt24 = abs(t(2)-t(4));
    cond = [dt23 dt43 dt24]<maxdt;
  if all(cond)
     kk=kk+1;
     format long
     dt(kk,:) = [ii t];
  end
end
```

A7. SOURCE LOCATION BASED FILTER-II CHANNEL SEQUENCE

```
clear all; clc;close all; format long
cd('F:\DIC_mozahid\Mozahid_CT2_April12');
%[num txt raw]=xlsread('sm2_aPRIL12_2012_fulldata.xlsx');
[num txt raw]=xlsread('sm2_aPRIL12_2012_fulldata_80%&swansong II.xlsx');
%[num txt raw]=xlsread('plb25flt25.xlsx','plb25');
%[num txt raw]=xlsread('sm2fulldata25.xlsx','sm2_aPRIL12_fulldata');
time = num(:,2);
ch = num(:,5);
format long
dt = [0; diff(time)];
sprintf('%.20f', dt)
%fprintf('value of b is %1.10e\n',dt)
event = [];
ii=0; nx = size(num,1);
idx = true(nx,1);
maxnumsensor = 8;
maxdt = 2e-2;
while any(idx)
  ii=ii+1;
  tidx = find(idx,maxnumsensor,'first');
  dtt = [0; diff(time(tidx))];
  nev = find(~(dtt<=maxdt),1,'first');
  if isempty(nev)
      nev = length(dtt)+1;
  end
  idx2 = 1:nev-1;
  event = [event; ii*ones(length(idx2),1)];
  tidx = tidx(idx2);
  idx(tidx)=false;
  fprintf('Looking for event %i\n',ii);
end

%%
%%filter based on channel sequences(3,1,2,4,5)

numevents = max(event);
format long
kk=0; dt=[];
for ii=1:numevents
  idx = event==ii;
  t = nan(1,8);
  tt = time(idx);
  chs = ch(idx);
  [chs indx] = sort(chs);
```

```
  tt = tt(indx);
  t(chs) = tt;
  % Time difference between ch1 and ch5
  dt31 = t(3)-t(1);
    % Time difference between ch2 and ch4
  dt32 = t(3)-t(2);
  dt34 = t(3)-t(4);
  dt35 = t(3)-t(5);
    cond = [dt31 dt32 dt34 dt35]<0;
  if all(cond)
     kk=kk+1;
     format long
     dt(kk,:) = [ii t];
     dtb(kk,:)=[t];
  end
end
X = dt(: , 2:9);
B = X( : );
b= B';
%%
dramin=nan(size(dt));
dramin(:,1)=dt(:,1);
for j=2:9
   for i=1:size(dt,1)
      [row,col,v]=find(num==dt(i,j));
      if size(row,1)~=0
         dramin(i,j)=num(row(1),7);
      else
         dramin(i,j)=nan;
      end
   end
end

%plot(dt(:,3),dramin(:,3),'ko')
%plot(dt(:,2),dramin(:,2),'ko')
%plot(dt(:,2),dramin(:),'ko')

figure1 = figure('Color',[1 1 1]);
hold on
for iii = 2:9
 plot(dt(:,iii),dramin(:,iii),'ko')
 %xydat = [dt(:,iii),dramin(:,iii)];
end
xlabel('Time(Sec)','FontWeight','bold','FontSize',12,...
   'FontName','Times New Roman')
ylabel('Amplitude (dB)','FontWeight','bold','FontSize',12,...
```

```
   'FontName','Times New Roman')
title('Amplitude vs Time','FontWeight','bold','FontSize',14,...
   'FontName','Times New Roman');
grid on
dtx2=dt(: , 2:9);
dty2=dramin(: , 2:9);
x2=dtx2(:);
y2=dty2(:);
xydat = [x2, y2];
xydat(any(isnan(xydat),2),:)=[];
%% Organizes events and times
numevents = max(event);
format long
kk=0; dt=[];
%maxdt = 7.72727273e-6;
%maxdt = 8.63636364e-6;
%maxdt = 9.54545455e-6;
maxdt = 20.45454545e-6;

for ii=1:numevents
  idx = event==ii;
  t = nan(1,8);
  tt = time(idx);
  chs = ch(idx);
  [chs indx] = sort(chs);
  tt = tt(indx);
  t(chs) = tt;
  % Time difference between ch1 and ch5
  %dt51 = abs(t(1)-t(5));
  % Time difference between ch3 and ch2
  dt23 = abs(t(3)-t(2));
  % Time difference between ch3 and ch4
  dt43 = abs(t(3)-t(4));
  % Time difference between ch2 and ch4
  dt24 = abs(t(2)-t(4));
    cond = [dt23 dt43 dt24]<maxdt;
  if all(cond)
     kk=kk+1;
     format long
     dt(kk,:) = [ii t];
  end
end
```

A8. FRACTURE ENERGY RELEASE CALCULATION

```
close all
clear all
syms x
%w =input('Inter Width(mm), w = ');
%t =input('Inter thickness (mm), t = ');
%Pmax =input('Inter maximum load (kN), Pmax = ');
%Pmin =input('Inter minimum load (kN), Pmin = ');
%Kic =input('Inter Fracture toughness (MPa-m^1/2), KiC = ');
w = 241.3;
t = 12.7;
Pmax = 65;
Pmin = 6.5;
Kic = 128*sqrt(1000);
delp = Pmax-Pmin;
a = solve((sqrt(1000)*Pmax*(2+x/w)*((0.886+4.64*x/w-13.32*(x/w)^2+14.72*(x/w)^3-
5.6*(x/w)^4))/(t*w^0.5*(1-x/w)^1.5))-Kic, x);
min=sort(a);
a_critical= min(2);
a_critical_from_crack_trip = a_critical-85.05;
x = 0:1:a_critical;
delk = delp.*(2+x/w).*((0.886+4.64.*x/w-13.32.*(x/w).^2+14.72.*(x/w).^3-
5.6.*(x/w).^4))./(t*w^0.5*(1-(x/w).^1.5));
N = (delk/31.6227766).^4;
y = 100*(1-exp(-N));
plot(delk,y,'-ro',x,delk,'-bo')
title('POD')
xlabel('Stress intensity range, delta K (MPa-m^1/2)')
ylabel('Probability of Detection(%)')
gtext('Detectable crack length')

%%
close all
clear all
%w =input('Inter Width(mm), w = ');
%t =input('Inter thickness (mm), t = ');
%Pmax =input('Inter maximum load (kN), Pmax = ');
%Pmin =input('Inter minimum load (kN), Pmin = ');
%Kic =input('Inter Fracture toughness (MPa-m^1/2), KiC = ');
w = 241.3;
t = 12.7;
Pmax = 65;
Pmin = 6.5;
Kic = 128*sqrt(1000);
delp = Pmax-Pmin;
```

```
figure
x = 0:1:150;
delk =31.6227766*delp.*(2+x/w).*((0.886+4.64.*x/w-13.32.*(x/w).^2+14.72.*(x/w).^3-
5.6.*(x/w).^4))./((t*w^0.5*(1-x/w).^1.5));
N = (delk/31.6227766).^2;
y = 100*(1-exp(-N));
%plot(delk,y,'-ro',delk,x,'-bo')
%plot(delk,y,'-ro')
%plotyy(delk,x)
[AX,H1,H2] = plotyy(delk,y,delk,x,'plot');
%plotyy(delk,y,delk,x,'plot')
set(get(AX(1),'Ylabel'),'String','Probability of Detection(%)')
set(get(AX(2),'Ylabel'),'String','Crack length,a (mm)')
title('Probability of AE Detection')
%xlabel('Time (\musec)')
xlabel('Stress intensity range, delK (MPa-m^1/2)')
set(H1,'LineStyle','*')
set(H2,'LineStyle',':')
%axes(h(1))
%ylabel('Probability of Detection(%)')
%axes(h(2))
%ylabel('Crack length, mm'); hold on;
%y2label= get(h2axes(2),'ylabel')
gtext('Detectable crack length')
%%
%Final one 12/16/2011
close all
clear all
syms x
%w =input('Inter Width(mm), w = ');
%t =input('Inter thickness (mm), t = ');
%Pmax =input('Inter maximum load (kN), Pmax = ');
%Pmin =input('Inter minimum load (kN), Pmin = ');
%Kic =input('Inter Fracture toughness (MPa-m^1/2), KiC = ');
w = 241.3;
t = 12.7;
Pmax = 65;
Pmin = 6.5;
Kic = 128;
delp = Pmax-Pmin;
a = solve((128-(Pmax*(2+x/w)*((0.886+4.64*x/w-13.32*(x/w)^2+14.72*(x/w)^3-
5.6*(x/w)^4)))/(t*w^0.5*(1-x/w)^1.5)), x);
min=sort(a);
a_critical= min(2);
figure
x = 83.5:1:a_critical-83.05;
```

```
delk =31.6227766.*delp.*(2+x/w).*((0.886+4.64.*x/w-13.32.*(x/w).^2+14.72.*(x/w).^3-
5.6.*(x/w).^4))./((t*w^0.5*(1-x/w).^1.5));
N = (delk/100).^7;
y = 100*(1-exp(-N));
%plot(delk,y,'-ro',delk,x,'-bo')
%plot(delk,y,'-ro')
%plotyy(delk,x)
[AX,H1,H2] = plotyy(delk,y,delk,x,'stem','plot');
%plotyy(delk,y,delk,x,'plot')
set(get(AX(1),'Ylabel'),'String','Probability of Detection(%)')
set(get(AX(2),'Ylabel'),'String','Crack length,a (mm)')
title('Probability of AE Detection')
%xlabel('Time (\musec)')
xlabel('Stress intensity range, delK (MPa-m^1/2)')
set(H1,'LineStyle','-')
set(H2,'LineStyle',':')
%axes(h(1))
%ylabel('Probability of Detection(%)')
%axes(h(2))
%ylabel('Crack length, mm'); hold on;
%y2label= get(h2axes(2),'ylabel')
%gtext('Detectable crack length')
%%
%Final one 01/04/2012
close all
clear all
%w =input('Inter Width(mm), w = ');
%t =input('Inter thickness (mm), t = ');
%Pmax =input('Inter maximum load (kN), Pmax = ');
%Pmin =input('Inter minimum load (kN), Pmin = ');
%Kic =input('Inter Fracture toughness (MPa-m^1/2), KiC = ');
w = 241.3;
t = 12.7;
Pmax = 65;
Pmin = 6.5;
Kic = 128;
E = 200000;
delp = Pmax-Pmin;
figure
x = 82.55:1:145;
delk =31.6227766.*delp.*(2+x/w).*((0.886+4.64.*x/w-13.32.*(x/w).^2+14.72.*(x/w).^3-
5.6.*(x/w).^4))./((t*w^0.5*(1-x/w).^1.5));
N = (delk/100).^7;
y = 100*(1-exp(-N));
[AX,H1,H2] = plotyy(delk,y,delk,x,'stem','plot');
set(get(AX(1),'Ylabel'),'String','Probability of Detection(%)')
```

```
set(get(AX(2),'Ylabel'),'String','Crack length,a (mm)')
title('Probability of AE Detection')
xlabel('Stress intensity range, delK (MPa-m^1/2)')
set(H1,'LineStyle','-')
set(H2,'LineStyle',':')
figure
x = 82.55:0.01:145;
delk =31.6227766.*delp.*(2+x/w).*((0.886+4.64.*x/w-13.32.*(x/w).^2+14.72.*(x/w).^3-
5.6.*(x/w).^4))./((t*w^0.5*(1-x/w).^1.5));
da =(1.93)*10^-9*(delk).^3.2989;
delJ = delk.^2/E*t.*da;
plot(x,delJ);
ylabel('Energy release rate, delJ(J/cycle)')% aJ: attojoule = 10^-18 joule
xlabel('Crack length, a(mm)')
figure
x = 82.55:0.01:145;
delk =31.6227766.*delp.*(2+x/w).*((0.886+4.64.*x/w-13.32.*(x/w).^2+14.72.*(x/w).^3-
5.6.*(x/w).^4))./((t*w^0.5*(1-x/w).^1.5));
da =(1.93)*10^-9*(delk).^3.2989;
delJ = delk.^2/E*t.*da;
plot(delk,delJ);
ylabel('Energy release rate, delJ(J/cycle)')% aJ: attojoule = 10^-18 joule
xlabel('Stress intensity range, delK (MPa-m^1/2)')
figure
x = 82.55:0.01:145;
delk =31.6227766.*delp.*(2+x/w).*((0.886+4.64.*x/w-13.32.*(x/w).^2+14.72.*(x/w).^3-
5.6.*(x/w).^4))./((t*w^0.5*(1-x/w).^1.5));
da =(1.93)*10^-9.*(delk).^3.2989;
plot(da,delk);
ylabel('Stress intensity range, delK (MPa-m^1/2)')
xlabel('Crack growth rate, da/dN(mm/cycle)')
```

A9. B-VALUE CALCULATION

```
clear;
clc;
close all
cd('C:\Users\Saima\Dropbox\Mathlab code');
%Load AE data from ASCII TEXT
% Eraase Header from text file and save with extension .dat (all files
% option must be selected at this point)
%Input file name below
%load the AE data from ASCII file
files = dir('*.mat');
if isempty(files)
    data_ae = load('fulldata.dat');
    %data_ae = load('fulldata80.dat');
        save('savedvariables.mat');
else
    load('savedvariables.mat');
end

%%
% This is the calaculation of the B value (Now all Channels)
run = 100;
%%%%%%%%%%%%%%%%%%%%%%%%%%%%
%Organization in groups
%%%%%%%%%%%%%%%%%%%%%%%%%%%%
dd = data_ae;
A = [dd(:,2),dd(:,4)];
nev = 100; %number of events in each set (must be less than half the total number of data points)
tam = size(A); %A: matrix containing amplitude and time data in columns [time, amp]
tam2 = tam(1);
int = tam2/nev; int2 = floor(int); %number of data packages
dint = int2 - int;
ind = 1:1:nev;
N=zeros(nev,1); Asp = N;
N_A = zeros(tam);
tmark=zeros(int2,1);
packages{1,int2}=[];
b_value=zeros(int2,1);
for i=1:int2
    As=A(ind,:);
    As=sort(As);
       for j=1:nev
           Asj=As(j,2);
           dat=find(As(:,2)>=Asj);
```

```
      N(j) = length(dat); Asp(j)=Asj;
    end
  N_A(ind,:)=[N,Asp];
  packages{i}=[log10(N),Asp];
  tmark(i)=max(A(ind,1));
  ind(:)=ind(:)+nev;
    if (dint<0) && (i==int2-1)
    ind=[ind,tam2]; nev=nev+1;
    end
  dset=packages{i};
  fit=polyfit(dset(:,2),dset(:,1),1);
  b_value(i)=20*abs(fit(1));

end
ampl47 = size(dd((dd(dd(:,4)>=45 & dd(:,4)<=49)),:));
ampl_47=ampl47(1,1);
ampl52 = size(dd((dd(dd(:,4)>=50 & dd(:,4)<=54)),:));
ampl_52=ampl52(1,1);
ampl57 = size(dd((dd(dd(:,4)>=55 & dd(:,4)<=59)),:));
ampl_57=ampl57(1,1);
ampl62 = size(dd((dd(dd(:,4)>=60 & dd(:,4)<=64)),:));
ampl_62=ampl62(1,1);
ampl67 = size(dd((dd(dd(:,4)>=65 & dd(:,4)<=69)),:));
ampl_67=ampl67(1,1);
ampl72 = size(dd((dd(dd(:,4)>=70 & dd(:,4)<=74)),:));
ampl_72=ampl72(1,1);
ampl77 = size(dd((dd(dd(:,4)>=75 & dd(:,4)<=79)),:));
ampl_77=ampl77(1,1);
ampl82 = size(dd((dd(dd(:,4)>=80 & dd(:,4)<=84)),:));
ampl_82=ampl82(1,1);
ampl87 = size(dd((dd(dd(:,4)>=85 & dd(:,4)<=89)),:));
ampl_87=ampl87(1,1);
ampl92 = size(dd((dd(dd(:,4)>=90 & dd(:,4)<=94)),:));
ampl_92=ampl92(1,1);
ampl97 = size(dd((dd(dd(:,4)>=95 & dd(:,4)<100)),:));
ampl_97=ampl97(1,1);
s=[ampl_47,ampl_52,ampl_57,ampl_62,ampl_67,ampl_72,ampl_77,ampl_82,ampl_87,a
mpl_92,ampl_97];
n=[47,52,57,62,67,72,77,82,87,92,97];
amp=data_ae(:,4);

figure(1)
plot(tmark,b_value,'k')
xlabel('Time(sec)','FontSize',12)
ylabel('b-value','FontSize',12)
title('Trend of b-value CHANNEL All','FontSize',14)
```

```
figure(2)
semilogy(n,s,'k.')
n(s==0) = [];
s(s==0) = [];
shat = log(s);
A = [ones(length(s),1) n'];
X = inv(A'*A)*A'*shat';
hold on
nn = [n(1):(n(end)-n(1))/10000:n(end)];
ss = exp(X(1)+nn*X(2));
semilogy(nn,ss,'k');
legend('Experimental data',sprintf('Best fit- b: %0.10g',X(2)));
xlabel('Amplitude range(dB)','FontSize',12)
ylabel('Frequency, N','FontSize',12)
title('Frequency vs Amplitude CHANNEL All','FontSize',14)

%% b-value for individual channel
chh = 8;
dd = data_ae(data_ae(:,3)==chh,:);
A = [dd(:,2),dd(:,4)];
nev = 100; %number of events in each set (must be less than half the total number of data points)
tam = size(A); %A: matrix containing amplitude and time data in columns [time, amp]
tam2 = tam(1);
int = tam2/nev; int2 = floor(int); %number of data packages
dint = int2 - int;
ind = 1:1:nev;
N=zeros(nev,1); Asp = N;
N_A = zeros(tam);
tmark=zeros(int2,1);
packages{1,int2}=[];
b_value=zeros(int2,1);
for i=1:int2
    As=A(ind,:);
    As=sort(As);
       for j=1:nev
           Asj=As(j,2);
           dat=find(As(:,2)>=Asj);
           N(j) = length(dat); Asp(j)=Asj;
       end
    N_A(ind,:)=[N,Asp];
    packages{i}=[log10(N),Asp];
    tmark(i)=max(A(ind,1));
    ind(:)=ind(:)+nev;
        if (dint<0) && (i==int2-1)
```

```
        ind=[ind,tam2]; nev=nev+1;
        end
    dset=packages{i};
    fit=polyfit(dset(:,2),dset(:,1),1);
    b_value(i)=20*abs(fit(1));

end
ampl47 = size(dd((dd(dd(:,4)>=45 & dd(:,4)<=49)),:));
ampl_47=ampl47(1,1);
ampl52 = size(dd((dd(dd(:,4)>=50 & dd(:,4)<=54)),:));
ampl_52=ampl52(1,1);
ampl57 = size(dd((dd(dd(:,4)>=55 & dd(:,4)<=59)),:));
ampl_57=ampl57(1,1);
ampl62 = size(dd((dd(dd(:,4)>=60 & dd(:,4)<=64)),:));
ampl_62=ampl62(1,1);
ampl67 = size(dd((dd(dd(:,4)>=65 & dd(:,4)<=69)),:));
ampl_67=ampl67(1,1);
ampl72 = size(dd((dd(dd(:,4)>=70 & dd(:,4)<=74)),:));
ampl_72=ampl72(1,1);
ampl77 = size(dd((dd(dd(:,4)>=75 & dd(:,4)<=79)),:));
ampl_77=ampl77(1,1);
ampl82 = size(dd((dd(dd(:,4)>=80 & dd(:,4)<=84)),:));
ampl_82=ampl82(1,1);
ampl87 = size(dd((dd(dd(:,4)>=85 & dd(:,4)<=89)),:));
ampl_87=ampl87(1,1);
ampl92 = size(dd((dd(dd(:,4)>=90 & dd(:,4)<=94)),:));
ampl_92=ampl92(1,1);
ampl97 = size(dd((dd(dd(:,4)>=95 & dd(:,4)<100)),:));
ampl_97=ampl97(1,1);
s=[ampl_47,ampl_52,ampl_57,ampl_62,ampl_67,ampl_72,ampl_77,ampl_82,ampl_87,a
mpl_92,ampl_97];
n=[47,52,57,62,67,72,77,82,87,92,97];
amp=data_ae(:,4);

figure(3)
plot(tmark,b_value, 'k');
xlabel('Time(sec)','FontSize',12);
ylabel('b-value','FontSize',12)
title('Trend of b-value CHANNEL 8','FontSize',14)
figure(4)
semilogy(n,s,'k.')
n(s==0) = [];
s(s==0) = [];
shat = log(s);
A = [ones(length(s),1) n'];
X = inv(A'*A)*A'*shat';
```

```
hold on
nn = [n(1):(n(end)-n(1))/1000000:n(end)];
ss = exp(X(1)+nn*X(2));
semilogy(nn,ss,'k');
legend('Experimental data',sprintf('Best fit- b: %0.10g',X(2)));
xlabel('Amplitude range(dB)','FontSize',12)
ylabel('Frequency, N','FontSize',12)
title('Frequency vs Amplitude CHANNEL 8','FontSize',14)
```

A10. B_VALUE_AMPLITUDE RANGE

```
%b_value_amplitude range.m

clear;
clc;
close all
cd('C:\Users\Saima\Dropbox\Mathlab code');
%Load AE data from ASCII TEXT
% Eraase Header from text file and save with extension .dat (all files
% option must be selected at this point)
%Input file name below
%load the AE data from ASCII file
files = dir('*.mat');
if isempty(files)
    data_ae = load('fulldata.dat');
    %data_ae = load('fulldata80.dat');
        save('savedvariables.mat');
else
    load('savedvariables.mat');
end

%%
% This is the calaculation of the B value (Now all Channels)
run = 100;
%%%%%%%%%%%%%%%%%%%%%%%%%%%%%
%Organization in groups
%%%%%%%%%%%%%%%%%%%%%%%%%%%%%
dd = data_ae;
A = [dd(:,2),dd(:,4)];
nev = 100; %number of events in each set (must be less than half the total number of data
points)
tam = size(A); %A: matrix containing amplitude and time data in columns [time, amp]
tam2 = tam(1);
int = tam2/nev; int2 = floor(int); %number of data packages
dint = int2 - int;
ind = 1:1:nev;
N=zeros(nev,1); Asp = N;
N_A = zeros(tam);
tmark=zeros(int2,1);
packages{1,int2}=[];
b_value=zeros(int2,1);
for i=1:int2
    As=A(ind,:);
    As=sort(As);
       for j=1:nev
```

```
          Asj=As(j,2);
          dat=find(As(:,2)>=Asj);
          N(j) = length(dat); Asp(j)=Asj;
       end
    N_A(ind,:)=[N,Asp];
    packages{i}=[log10(N),Asp];
    tmark(i)=max(A(ind,1));
    ind(:)=ind(:)+nev;
       if (dint<0) && (i==int2-1)
       ind=[ind,tam2]; nev=nev+1;
       end
    dset=packages{i};
    fit=polyfit(dset(:,2),dset(:,1),1);
    b_value(i)=20*abs(fit(1));

end
ampl47 = size(dd((dd(dd(:,4)>=45 & dd(:,4)<=49)),:));
ampl_47=ampl47(1,1);
ampl52 = size(dd((dd(dd(:,4)>=50 & dd(:,4)<=54)),:));
ampl_52=ampl52(1,1);
ampl57 = size(dd((dd(dd(:,4)>=55 & dd(:,4)<=59)),:));
ampl_57=ampl57(1,1);
ampl62 = size(dd((dd(dd(:,4)>=60 & dd(:,4)<=64)),:));
ampl_62=ampl62(1,1);
ampl67 = size(dd((dd(dd(:,4)>=65 & dd(:,4)<=69)),:));
ampl_67=ampl67(1,1);
ampl72 = size(dd((dd(dd(:,4)>=70 & dd(:,4)<=74)),:));
ampl_72=ampl72(1,1);
ampl77 = size(dd((dd(dd(:,4)>=75 & dd(:,4)<=79)),:));
ampl_77=ampl77(1,1);
ampl82 = size(dd((dd(dd(:,4)>=80 & dd(:,4)<=84)),:));
ampl_82=ampl82(1,1);
ampl87 = size(dd((dd(dd(:,4)>=85 & dd(:,4)<=89)),:));
ampl_87=ampl87(1,1);
ampl92 = size(dd((dd(dd(:,4)>=90 & dd(:,4)<=94)),:));
ampl_92=ampl92(1,1);
ampl97 = size(dd((dd(dd(:,4)>=95 & dd(:,4)<100)),:));
ampl_97=ampl97(1,1);
s=[ampl_47,ampl_52,ampl_57,ampl_62,ampl_67,ampl_72,ampl_77,ampl_82,ampl_87,a
mpl_92,ampl_97];
n=[47,52,57,62,67,72,77,82,87,92,97];
amp=data_ae(:,4);

figure(1)
plot(tmark,b_value,'k')
xlabel('Time(sec)','FontSize',12)
```

```
ylabel('b-value','FontSize',12)
title('Trend of b-value CHANNEL All','FontSize',14)

figure(2)
semilogy(n,s,'k.')
n(s==0) = [];
s(s==0) = [];
shat = log(s);
A = [ones(length(s),1) n'];
X = inv(A'*A)*A'*shat';
hold on
nn = [n(1):(n(end)-n(1))/10000:n(end)];
ss = exp(X(1)+nn*X(2));
semilogy(nn,ss,'k');
legend('Experimental data',sprintf('Best fit- b: %0.10g',X(2)));
xlabel('Amplitude range(dB)','FontSize',12)
ylabel('Frequency, N','FontSize',12)
title('Frequency vs Amplitude CHANNEL All','FontSize',14)

%% b-value for individual channel
chh = 8;
dd = data_ae(data_ae(:,3)==chh,:);
A = [dd(:,2),dd(:,4)];
nev = 100; %number of events in each set (must be less than half the total number of data
points)
tam = size(A); %A: matrix containing amplitude and time data in columns [time, amp]
tam2 = tam(1);
int = tam2/nev; int2 = floor(int); %number of data packages
dint = int2 - int;
ind = 1:1:nev;
N=zeros(nev,1); Asp = N;
N_A = zeros(tam);
tmark=zeros(int2,1);
packages{1,int2}=[];
b_value=zeros(int2,1);
for i=1:int2
    As=A(ind,:);
    As=sort(As);
       for j=1:nev
           Asj=As(j,2);
           dat=find(As(:,2)>=Asj);
           N(j) = length(dat); Asp(j)=Asj;
       end
    N_A(ind,:)=[N,Asp];
    packages{i}=[log10(N),Asp];
    tmark(i)=max(A(ind,1));
```

```
    ind(:)=ind(:)+nev;
        if (dint<0) && (i==int2-1)
        ind=[ind,tam2]; nev=nev+1;
        end
    dset=packages{i};
    fit=polyfit(dset(:,2),dset(:,1),1);
    b_value(i)=20*abs(fit(1));

end
ampl47 = size(dd((dd(dd(:,4)>=45 & dd(:,4)<=49)),:));
ampl_47=ampl47(1,1);
ampl52 = size(dd((dd(dd(:,4)>=50 & dd(:,4)<=54)),:));
ampl_52=ampl52(1,1);
ampl57 = size(dd((dd(dd(:,4)>=55 & dd(:,4)<=59)),:));
ampl_57=ampl57(1,1);
ampl62 = size(dd((dd(dd(:,4)>=60 & dd(:,4)<=64)),:));
ampl_62=ampl62(1,1);
ampl67 = size(dd((dd(dd(:,4)>=65 & dd(:,4)<=69)),:));
ampl_67=ampl67(1,1);
ampl72 = size(dd((dd(dd(:,4)>=70 & dd(:,4)<=74)),:));
ampl_72=ampl72(1,1);
ampl77 = size(dd((dd(dd(:,4)>=75 & dd(:,4)<=79)),:));
ampl_77=ampl77(1,1);
ampl82 = size(dd((dd(dd(:,4)>=80 & dd(:,4)<=84)),:));
ampl_82=ampl82(1,1);
ampl87 = size(dd((dd(dd(:,4)>=85 & dd(:,4)<=89)),:));
ampl_87=ampl87(1,1);
ampl92 = size(dd((dd(dd(:,4)>=90 & dd(:,4)<=94)),:));
ampl_92=ampl92(1,1);
ampl97 = size(dd((dd(dd(:,4)>=95 & dd(:,4)<100)),:));
ampl_97=ampl97(1,1);
s=[ampl_47,ampl_52,ampl_57,ampl_62,ampl_67,ampl_72,ampl_77,ampl_82,ampl_87,a
mpl_92,ampl_97];
n=[47,52,57,62,67,72,77,82,87,92,97];
amp=data_ae(:,4);

figure(3)
plot(tmark,b_value, 'k');
xlabel('Time(sec)','FontSize',12);
ylabel('b-value','FontSize',12)
title('Trend of b-value CHANNEL 8','FontSize',14)
figure(4)
semilogy(n,s,'k.')
n(s==0) = [];
s(s==0) = [];
shat = log(s);
```

```
A = [ones(length(s),1) n'];
X = inv(A'*A)*A'*shat';
hold on
nn = [n(1):(n(end)-n(1))/1000000:n(end)];
ss = exp(X(1)+nn*X(2));
semilogy(nn,ss,'k');
legend('Experimental data',sprintf('Best fit- b: %0.10g',X(2)));
xlabel('Amplitude range(dB)','FontSize',12)
ylabel('Frequency, N','FontSize',12)
title('Frequency vs Amplitude CHANNEL 8','FontSize',14)
```

A11. B-VALUE ANALYSIS

```
%b_value_analysis.m
clear;
clc;
close all
%Load AE data from ASCII TEXT
% Eraase Header from text file and save with extension .dat (all files
% option must be selected at this point)
%Input file name below
%load the AE data from ASCII file
files = dir('*.mat');
if isempty(files)
   %data_ae = load('fulldata.dat');
   data_ae = load('fulldata80.dat');
      save('savedvariables.mat');
else
   load('savedvariables.mat');
end

%%
% This is the calaculation of the B value (Now all Channels)
run = 10000000000000000000;
%%%%%%%%%%%%%%%%%%%%%%%%%%
%Organization in groups
%%%%%%%%%%%%%%%%%%%%%%%%%%
dd = data_ae;
A = [dd(:,2),dd(:,4)];
nev = 100; %number of events in each set (must be less than half the total number of data
points)
tam = size(A); %A: matrix containing amplitude and time data in columns [time, amp]
tam2 = tam(1);
int = tam2/nev; int2 = floor(int); %number of data packages
dint = int2 - int;
ind = 1:1:nev;
N=zeros(nev,1); Asp = N;
N_A = zeros(tam);
tmark=zeros(int2,1);
packages{1,int2}=[];
b_value=zeros(int2,1);
for i=1:int2
   As=A(ind,:);
   As=sort(As);
     for j=1:nev
        Asj=As(j,2);
        dat=find(As(:,2)>=Asj);
```

```
        N(j) = length(dat); Asp(j)=Asj;
     end
   N_A(ind,:)=[N,Asp];
   packages{i}=[log10(N),Asp];
   tmark(i)=max(A(ind,1));
   ind(:)=ind(:)+nev;
      if (dint<0) && (i==int2-1)
      ind=[ind,tam2]; nev=nev+1;
      end
   dset=packages{i};
   fit=polyfit(dset(:,2),dset(:,1),1);
   b_value(i)=20*abs(fit(1));

end
amp45 = size(data_ae((data_ae(data_ae(:,4)>=45 & data_ae(:,4)<=45.5)),:));
amp_45=amp45(1,1);
amp46 = size(data_ae((data_ae(data_ae(:,4)>=45.5 & data_ae(:,4)<=46.5)),:));
amp_46=amp46(1,1);
amp47 = size(data_ae((data_ae(data_ae(:,4)>=46.5 & data_ae(:,4)<=47.5)),:));
amp_47=amp47(1,1);
amp48 = size(data_ae((data_ae(data_ae(:,4)>=47.5 & data_ae(:,4)<48.5)),:));
amp_48=amp48(1,1);
amp49 = size(data_ae((data_ae(data_ae(:,4)>=48.5 & data_ae(:,4)<49.5)),:));
amp_49=amp49(1,1);
amp50 = size(data_ae((data_ae(data_ae(:,4)>=49.5 & data_ae(:,4)<50.5)),:));
amp_50=amp50(1,1);
amp51 = size(data_ae((data_ae(data_ae(:,4)>=50.5 & data_ae(:,4)<51.5)),:));
amp_51=amp51(1,1);
amp52 = size(data_ae((data_ae(data_ae(:,4)>=51.5 & data_ae(:,4)<52.5)),:));
amp_52=amp52(1,1);
amp53 = size(data_ae((data_ae(data_ae(:,4)>=52.5 & data_ae(:,4)<53.5)),:));
amp_53=amp53(1,1);
amp54 = size(data_ae((data_ae(data_ae(:,4)>=53.5 & data_ae(:,4)<54.5)),:));
amp_54=amp54(1,1);
amp55 = size(data_ae((data_ae(data_ae(:,4)>=54.5 & data_ae(:,4)<55.5)),:));
amp_55=amp55(1,1);
amp56 = size(data_ae((data_ae(data_ae(:,4)>=55.5 & data_ae(:,4)<56.5)),:));
amp_56=amp56(1,1);
amp57 = size(data_ae((data_ae(data_ae(:,4)>=56.5 & data_ae(:,4)<57.5)),:));
amp_57=amp57(1,1);
amp58 = size(data_ae((data_ae(data_ae(:,4)>=57.5 & data_ae(:,4)<58.5)),:));
amp_58=amp58(1,1);
amp59 = size(data_ae((data_ae(data_ae(:,4)>=58.5 & data_ae(:,4)<59.5)),:));
amp_59=amp59(1,1);
amp60 = size(data_ae((data_ae(data_ae(:,4)>=59.5 & data_ae(:,4)<60.5)),:));
amp_60=amp60(1,1);
```

```
amp61 = size(data_ae((data_ae(data_ae(:,4)>=60.5 & data_ae(:,4)<61.5)),:));
amp_61=amp61(1,1);
amp62 = size(data_ae((data_ae(data_ae(:,4)>=61.5 & data_ae(:,4)<62.5)),:));
amp_62=amp62(1,1);
amp63 = size(data_ae((data_ae(data_ae(:,4)>=62.5 & data_ae(:,4)<63.5)),:));
amp_63=amp63(1,1);
amp64 = size(data_ae((data_ae(data_ae(:,4)>=63.5 & data_ae(:,4)<64.5)),:));
amp_64=amp64(1,1);
amp65 = size(data_ae((data_ae(data_ae(:,4)>=64.5 & data_ae(:,4)<65.5)),:));
amp_65=amp65(1,1);
amp66 = size(data_ae((data_ae(data_ae(:,4)>=65.5 & data_ae(:,4)<66.5)),:));
amp_66=amp66(1,1);
amp67 = size(data_ae((data_ae(data_ae(:,4)>=66.5 & data_ae(:,4)<67.5)),:));
amp_67=amp67(1,1);
amp68 = size(data_ae((data_ae(data_ae(:,4)>=67.5 & data_ae(:,4)<68.5)),:));
amp_68=amp68(1,1);
amp69 = size(data_ae((data_ae(data_ae(:,4)>=68.5 & data_ae(:,4)<69.5)),:));
amp_69=amp69(1,1);
amp70 = size(data_ae((data_ae(data_ae(:,4)>=69.5 & data_ae(:,4)<70.5)),:));
amp_70=amp70(1,1);
amp71 = size(data_ae((data_ae(data_ae(:,4)>=70.5 & data_ae(:,4)<71.5)),:));
amp_71=amp71(1,1);
amp72 = size(data_ae((data_ae(data_ae(:,4)>=71.5 & data_ae(:,4)<72.5)),:));
amp_72=amp72(1,1);
amp73 = size(data_ae((data_ae(data_ae(:,4)>=72.5 & data_ae(:,4)<73.5)),:));
amp_73=amp73(1,1);
amp74 = size(data_ae((data_ae(data_ae(:,4)>=73.5 & data_ae(:,4)<74.5)),:));
amp_74=amp74(1,1);
amp75 = size(data_ae((data_ae(data_ae(:,4)>=74.5 & data_ae(:,4)<75.5)),:));
amp_75=amp75(1,1);
amp76 = size(data_ae((data_ae(data_ae(:,4)>=75.5 & data_ae(:,4)<76.5)),:));
amp_76=amp76(1,1);
amp77 = size(data_ae((data_ae(data_ae(:,4)>=76.5 & data_ae(:,4)<77.5)),:));
amp_77=amp77(1,1);
amp78 = size(data_ae((data_ae(data_ae(:,4)>=77.5 & data_ae(:,4)<78.5)),:));
amp_78=amp78(1,1);
amp79 = size(data_ae((data_ae(data_ae(:,4)>=78.5 & data_ae(:,4)<79.5)),:));
amp_79=amp79(1,1);
amp80 = size(data_ae((data_ae(data_ae(:,4)>=79.5 & data_ae(:,4)<80.5)),:));
amp_80=amp80(1,1);
amp81 = size(data_ae((data_ae(data_ae(:,4)>=80.5 & data_ae(:,4)<81.5)),:));
amp_81=amp81(1,1);
amp82 = size(data_ae((data_ae(data_ae(:,4)>=81.5 & data_ae(:,4)<82.5)),:));
amp_82=amp82(1,1);
amp83 = size(data_ae((data_ae(data_ae(:,4)>=82.5 & data_ae(:,4)<83.5)),:));
amp_83=amp83(1,1);
```

```
amp84 = size(data_ae((data_ae(data_ae(:,4)>=83.5 & data_ae(:,3)<84.5)),:));
amp_84=amp84(1,1);
amp85 = size(data_ae((data_ae(data_ae(:,4)>=84.5 & data_ae(:,4)<85.5)),:));
amp_85=amp85(1,1);
amp86 = size(data_ae((data_ae(data_ae(:,4)>=85.5 & data_ae(:,4)<86.5)),:));
amp_86=amp86(1,1);
amp87 = size(data_ae((data_ae(data_ae(:,4)>=86.5 & data_ae(:,4)<87.5)),:));
amp_87=amp87(1,1);
amp88 = size(data_ae((data_ae(data_ae(:,4)>=87.5 & data_ae(:,4)<88.5)),:));
amp_88=amp88(1,1);
amp89 = size(data_ae((data_ae(data_ae(:,4)>=88.5 & data_ae(:,4)<89.5)),:));
amp_89=amp89(1,1);
amp90 = size(data_ae((data_ae(data_ae(:,4)>=89.5 & data_ae(:,4)<90.5)),:));
amp_90=amp90(1,1);
amp91 = size(data_ae((data_ae(data_ae(:,4)>=90.5 & data_ae(:,4)<91.5)),:));
amp_91=amp91(1,1);
amp92 = size(data_ae((data_ae(data_ae(:,4)>=91.5 & data_ae(:,4)<92.5)),:));
amp_92=amp92(1,1);
amp93 = size(data_ae((data_ae(data_ae(:,4)>=92.5 & data_ae(:,4)<93.5)),:));
amp_93=amp93(1,1);
amp94 = size(data_ae((data_ae(data_ae(:,4)>=93.5 & data_ae(:,4)<94.5)),:));
amp_94=amp94(1,1);
amp95 = size(data_ae((data_ae(data_ae(:,4)>=94.5 & data_ae(:,4)<95.5)),:));
amp_95=amp95(1,1);
amp96 = size(data_ae((data_ae(data_ae(:,4)>=95.5 & data_ae(:,4)<96.5)),:));
amp_96=amp96(1,1);
amp97 = size(data_ae((data_ae(data_ae(:,4)>=96.5 & data_ae(:,4)<97.5)),:));
amp_97=amp97(1,1);
amp98 = size(data_ae((data_ae(data_ae(:,4)>=97.5 & data_ae(:,4)<98.5)),:));
amp_98=amp98(1,1);
amp99 = size(data_ae((data_ae(data_ae(:,4)>=98.5 & data_ae(:,4)<99.5)),:));
amp_99=amp99(1,1);
amp100 = size(data_ae((data_ae(data_ae(:,4)>=99.5 & data_ae(:,4)<=100)),:));
amp_100=amp100(1,1);
s=[amp_45,amp_46,amp_47,amp_48,amp_49,amp_50,amp_51,amp_52,amp_53,amp_54,amp_55,amp_56,amp_57,amp_58,amp_59,amp_60,amp_61,amp_62,amp_63,amp_64,amp_65,amp_66,amp_67,amp_68,amp_69,amp_70,amp_71,amp_72,amp_73,amp_74,amp_75,amp_76,amp_77,amp_78,amp_79,amp_80,amp_81,amp_82,amp_83,amp_84,amp_85,amp_86,amp_87,amp_88,amp_89,amp_90,amp_91,amp_92,amp_93,amp_94,amp_95,amp_96,amp_97,amp_98,amp_99,amp_100];
n=[45,46,47,48,49,50,51,52,53,54,55,56,57,58,59,60,61,62,63,64,65,66,67,68,69,70,71,72,73,74,75,76,77,78,79,80,81,82,83,84,85,86,87,88,89,90,91,92,93,94,95,96,97,98,99,100];
amp=data_ae(:,4);

figure(1)
```

```
plot(tmark,b_value,'k')
xlabel('Time(sec)')
ylabel('B-Value')
title('B-Value vs. Time')

figure(2)
semilogy(n,s,'k.')
n(s==0) = [];
s(s==0) = [];
shat = log(s);
A = [ones(length(s),1) n'];
X = inv(A'*A)*A'*shat';
hold on
nn = [n(1):(n(end)-n(1))/10000:n(end)];
ss = exp(X(1)+nn*X(2));
semilogy(nn,ss,'k');
legend('Experimental Data',sprintf('Best fit- b: %0.10g',X(2)));
xlabel('Amplitude(dB)')
ylabel('Frequency, N')

%% b-value for individual channel
chh = 7;
dd = data_ae(data_ae(:,3)==chh,:);
A = [dd(:,2),dd(:,4)];
nev = 100; %number of events in each set (must be less than half the total number of data
points)
tam = size(A); %A: matrix containing amplitude and time data in columns [time, amp]
tam2 = tam(1);
int = tam2/nev; int2 = floor(int); %number of data packages
dint = int2 - int;
ind = 1:1:nev;
N=zeros(nev,1); Asp = N;
N_A = zeros(tam);
tmark=zeros(int2,1);
packages{1,int2}=[];
b_value=zeros(int2,1);
for i=1:int2
   As=A(ind,:);
   As=sort(As);
      for j=1:nev
         Asj=As(j,2);
         dat=find(As(:,2)>=Asj);
         N(j) = length(dat); Asp(j)=Asj;
      end
   N_A(ind,:)=[N,Asp];
   packages{i}=[log10(N),Asp];
```

```
   tmark(i)=max(A(ind,1));
   ind(:)=ind(:)+nev;
      if (dint<0) && (i==int2-1)
      ind=[ind,tam2]; nev=nev+1;
      end
   dset=packages{i};
   fit=polyfit(dset(:,2),dset(:,1),1);
   b_value(i)=20*abs(fit(1));

end
ampl45 = size(dd((dd(dd(:,4)>=45 & dd(:,4)<=45.5)),:));
ampl_45=ampl45(1,1);
ampl46 = size(dd((dd(dd(:,4)>=45.5 & dd(:,4)<=46.5)),:));
ampl_46=ampl46(1,1);
ampl47 = size(dd((dd(dd(:,4)>=46.5 & dd(:,4)<=47.5)),:));
ampl_47=ampl47(1,1);
ampl48 = size(dd((dd(dd(:,4)>=47.5 & dd(:,4)<48.5)),:));
ampl_48=ampl48(1,1);
ampl49 = size(dd((dd(dd(:,4)>=48.5 & dd(:,4)<49.5)),:));
ampl_49=ampl49(1,1);
ampl50 = size(dd((dd(dd(:,4)>=49.5 & dd(:,4)<50.5)),:));
ampl_50=ampl50(1,1);
ampl51 = size(dd((dd(dd(:,4)>=50.5 & dd(:,4)<51.5)),:));
ampl_51=ampl51(1,1);
ampl52 = size(dd((dd(dd(:,4)>=51.5 & dd(:,4)<52.5)),:));
ampl_52=ampl52(1,1);
ampl53 = size(dd((dd(dd(:,4)>=52.5 & dd(:,4)<53.5)),:));
ampl_53=ampl53(1,1);
ampl54 = size(dd((dd(dd(:,4)>=53.5 & dd(:,4)<54.5)),:));
ampl_54=ampl54(1,1);
ampl55 = size(dd((dd(dd(:,4)>=54.5 & dd(:,4)<55.5)),:));
ampl_55=ampl55(1,1);
ampl56 = size(dd((dd(dd(:,4)>=55.5 & dd(:,4)<56.5)),:));
ampl_56=ampl56(1,1);
ampl57 = size(dd((dd(dd(:,4)>=56.5 & dd(:,4)<57.5)),:));
ampl_57=ampl57(1,1);
ampl58 = size(dd((dd(dd(:,4)>=57.5 & dd(:,4)<58.5)),:));
ampl_58=ampl58(1,1);
ampl59 = size(dd((dd(dd(:,4)>=58.5 & dd(:,4)<59.5)),:));
ampl_59=ampl59(1,1);
ampl60 = size(dd((dd(dd(:,4)>=59.5 & dd(:,4)<60.5)),:));
ampl_60=ampl60(1,1);
ampl61 = size(dd((dd(dd(:,4)>=60.5 & dd(:,4)<61.5)),:));
ampl_61=ampl61(1,1);
ampl62 = size(dd((dd(dd(:,4)>=61.5 & dd(:,4)<62.5)),:));
ampl_62=ampl62(1,1);
```

```
ampl63 = size(dd((dd(dd(:,4)>=62.5 & dd(:,4)<63.5)),:));
ampl_63=ampl63(1,1);
ampl64 = size(dd((dd(dd(:,4)>=63.5 & dd(:,4)<64.5)),:));
ampl_64=ampl64(1,1);
ampl65 = size(data_ae((dd(dd(:,4)>=64.5 & dd(:,4)<65.5)),:));
ampl_65=ampl65(1,1);
ampl66 = size(dd((dd(dd(:,4)>=65.5 & dd(:,4)<66.5)),:));
ampl_66=ampl66(1,1);
ampl67 = size(dd((dd(dd(:,4)>=66.5 & dd(:,4)<67.5)),:));
ampl_67=ampl67(1,1);
ampl68 = size(dd((dd(dd(:,4)>=67.5 & dd(:,4)<68.5)),:));
ampl_68=ampl68(1,1);
ampl69 = size(dd((dd(dd(:,4)>=68.5 & dd(:,4)<69.5)),:));
ampl_69=ampl69(1,1);
ampl70 = size(dd((dd(dd(:,4)>=69.5 & dd(:,4)<70.5)),:));
ampl_70=ampl70(1,1);
ampl71 = size(dd((dd(dd(:,4)>=70.5 & dd(:,4)<71.5)),:));
ampl_71=ampl71(1,1);
ampl72 = size(dd((dd(dd(:,4)>=71.5 & dd(:,4)<72.5)),:));
ampl_72=ampl72(1,1);
ampl73 = size(dd((dd(dd(:,4)>=72.5 & dd(:,4)<73.5)),:));
ampl_73=ampl73(1,1);
ampl74 = size(dd((dd(dd(:,4)>=73.5 & dd(:,4)<74.5)),:));
ampl_74=ampl74(1,1);
ampl75 = size(dd((dd(dd(:,4)>=74.5 & dd(:,4)<75.5)),:));
ampl_75=ampl75(1,1);
ampl76 = size(dd((dd(dd(:,4)>=75.5 & dd(:,4)<76.5)),:));
ampl_76=ampl76(1,1);
ampl77 = size(dd((dd(dd(:,4)>=76.5 & dd(:,4)<77.5)),:));
ampl_77=ampl77(1,1);
ampl78 = size(dd((dd(dd(:,4)>=77.5 & dd(:,4)<78.5)),:));
ampl_78=ampl78(1,1);
ampl79 = size(dd((dd(dd(:,4)>=78.5 & dd(:,4)<79.5)),:));
ampl_79=ampl79(1,1);
ampl80 = size(dd((dd(dd(:,4)>=79.5 & dd(:,4)<80.5)),:));
ampl_80=ampl80(1,1);
ampl81 = size(dd((dd(dd(:,4)>=80.5 & dd(:,4)<81.5)),:));
ampl_81=ampl81(1,1);
ampl82 = size(dd((dd(dd(:,4)>=81.5 & dd(:,4)<82.5)),:));
ampl_82=ampl82(1,1);
ampl83 = size(dd((dd(dd(:,4)>=82.5 & dd(:,4)<83.5)),:));
ampl_83=ampl83(1,1);
ampl84 = size(dd((dd(dd(:,4)>=83.5 & dd(:,3)<84.5)),:));
ampl_84=ampl84(1,1);
ampl85 = size(dd((dd(dd(:,4)>=84.5 & dd(:,4)<85.5)),:));
ampl_85=ampl85(1,1);
```

```
ampl86 = size(dd((dd(dd(:,4)>=85.5 & dd(:,4)<86.5)),:));
ampl_86=ampl86(1,1);
ampl87 = size(dd((dd(dd(:,4)>=86.5 & dd(:,4)<87.5)),:));
ampl_87=ampl87(1,1);
ampl88 = size(dd((dd(dd(:,4)>=87.5 & dd(:,4)<88.5)),:));
ampl_88=ampl88(1,1);
ampl89 = size(dd((dd(dd(:,4)>=88.5 & dd(:,4)<89.5)),:));
ampl_89=ampl89(1,1);
ampl90 = size(dd((dd(dd(:,4)>=89.5 & dd(:,4)<90.5)),:));
ampl_90=ampl90(1,1);
ampl91 = size(dd((dd(dd(:,4)>=90.5 & dd(:,4)<91.5)),:));
ampl_91=ampl91(1,1);
ampl92 = size(dd((dd(dd(:,4)>=91.5 & dd(:,4)<92.5)),:));
ampl_92=ampl92(1,1);
ampl93 = size(dd((dd(dd(:,4)>=92.5 & dd(:,4)<93.5)),:));
ampl_93=ampl93(1,1);
ampl94 = size(dd((dd(dd(:,4)>=93.5 & dd(:,4)<94.5)),:));
ampl_94=ampl94(1,1);
ampl95 = size(dd((dd(dd(:,4)>=94.5 & dd(:,4)<95.5)),:));
ampl_95=ampl95(1,1);
ampl96 = size(dd((dd(dd(:,4)>=95.5 & dd(:,4)<96.5)),:));
ampl_96=ampl96(1,1);
ampl97 = size(dd((dd(dd(:,4)>=96.5 & dd(:,4)<97.5)),:));
ampl_97=ampl97(1,1);
ampl98 = size(dd((dd(dd(:,4)>=97.5 & dd(:,4)<98.5)),:));
ampl_98=ampl98(1,1);
ampl99 = size(dd((dd(dd(:,4)>=98.5 & dd(:,4)<99.5)),:));
ampl_99=ampl99(1,1);
ampl100 = size(dd((dd(dd(:,4)>=99.5 & dd(:,4)<=100)),:));
ampl_100=ampl100(1,1);
s=[ampl_45,ampl_46,ampl_47,ampl_48,ampl_49,ampl_50,ampl_51,ampl_52,ampl_53,a
mpl_54,ampl_55,ampl_56,ampl_57,ampl_58,ampl_59,ampl_60,ampl_61,ampl_62,ampl_
63,ampl_64,ampl_65,ampl_66,ampl_67,ampl_68,ampl_69,ampl_70,ampl_71,ampl_72,a
mpl_73,ampl_74,ampl_75,ampl_76,ampl_77,ampl_78,ampl_79,ampl_80,ampl_81,ampl_
82,ampl_83,ampl_84,ampl_85,ampl_86,ampl_87,ampl_88,ampl_89,ampl_90,ampl_91,a
mpl_92,ampl_93,ampl_94,ampl_95,ampl_96,ampl_97,ampl_98,ampl_99,ampl_100];
n=[45,46,47,48,49,50,51,52,53,54,55,56,57,58,59,60,61,62,63,64,65,66,67,68,69,70,71,7
2,73,74,75,76,77,78,79,80,81,82,83,84,85,86,87,88,89,90,91,92,93,94,95,96,97,98,99,100
];
amp=data_ae(:,4);

figure(3)
plot(tmark,b_value, 'k');
xlabel('Time');
ylabel('b-value')
title('b-Value vs. Time')
```

```
figure(4)
semilogy(n,s,'k.')
n(s==0) = [];
s(s==0) = [];
shat = log(s);
A = [ones(length(s),1) n'];
X = inv(A'*A)*A'*shat';
hold on
nn = [n(1):(n(end)-n(1))/10000:n(end)];
ss = exp(X(1)+nn*X(2));
semilogy(nn,ss,'k');
legend('Experimental Data',sprintf('Best fit- b: %0.10g',X(2)));
xlabel('Amplitude range(dB)')
ylabel('Frequency, N')
title('Frequency vs Time: Channel')
```

A12. B-VALUE ANALSYS

```
%b-value analysis.m
clear;
clc;
close all
%Load AE data from ASCII TEXT
% Eraase Header from text file and save with extension .dat (all files
% option must be selected at this point)
%Input file name below

%load the AE data from ASCII file
files = dir('*.mat');
if isempty(files)
   data_ae = load('fulldata.dat');
   %data_ae = load('fulldata80.dat');
      save('savedvariables.mat');
else
   load('savedvariables.mat');
end

%Data_ae columns coorsepond to the following data as the program is written
%now

%  1      2     3    4      5     6       7         8    9      10     11
% ID, Time(s), CH, RISE, COUN, ENER, DURATION, AMP, A-FRQ, RMS, PCNTS,

%   12           13        14     15
%SIG STRNGTH, ABS-ENERGY, C-FRQ, P-FRQ

%%
% This is the calaculation of the B value (Now all Channels)
run = 10000000000000000000;
%%%%%%%%%%%%%%%%%%%%%%%%%%%
%Organization in groups
%%%%%%%%%%%%%%%%%%%%%%%%%%%
dd = data_ae;
A = [dd(:,2),dd(:,3)];
nev = 100; %number of events in each set (must be less than half the total number of data
points)
tam = size(A); %A: matrix containing amplitude and time data in columns [time, amp]
tam2 = tam(1);
int = tam2/nev; int2 = floor(int); %number of data packages
dint = int2 - int;
ind = 1:1:nev;
N=zeros(nev,1); Asp = N;
```

```
N_A = zeros(tam);
tmark=zeros(int2,1);
packages{1,int2}=[];
b_value=zeros(int2,1);
for i=1:int2
    As=A(ind,:);
    As=sort(As);
       for j=1:nev
           Asj=As(j,2);
           dat=find(As(:,2)>=Asj);
           N(j) = length(dat); Asp(j)=Asj;
       end
    N_A(ind,:)=[N,Asp];
    packages{i}=[log10(N),Asp];
    tmark(i)=max(A(ind,1));
    ind(:)=ind(:)+nev;
        if (dint<0) && (i==int2-1)
        ind=[ind,tam2]; nev=nev+1;
        end
    dset=packages{i};
    fit=polyfit(dset(:,2),dset(:,1),1);
    b_value(i)=20*abs(fit(1));

end

amp45 = size(data_ae((data_ae(data_ae(:,3)>=45 & data_ae(:,3)<=45.5)),:));
amp_45=amp45(1,1);
amp46 = size(data_ae((data_ae(data_ae(:,3)>=45.5 & data_ae(:,3)<=46.5)),:));
amp_46=amp46(1,1);
amp47 = size(data_ae((data_ae(data_ae(:,3)>=46.5 & data_ae(:,3)<=47.5)),:));
amp_47=amp47(1,1);
amp48 = size(data_ae((data_ae(data_ae(:,3)>=47.5 & data_ae(:,3)<48.5)),:));
amp_48=amp48(1,1);
amp49 = size(data_ae((data_ae(data_ae(:,3)>=48.5 & data_ae(:,3)<49.5)),:));
amp_49=amp49(1,1);
amp50 = size(data_ae((data_ae(data_ae(:,3)>=49.5 & data_ae(:,3)<50.5)),:));
amp_50=amp50(1,1);
amp51 = size(data_ae((data_ae(data_ae(:,3)>=50.5 & data_ae(:,3)<51.5)),:));
amp_51=amp51(1,1);
amp52 = size(data_ae((data_ae(data_ae(:,3)>=51.5 & data_ae(:,3)<52.5)),:));
amp_52=amp52(1,1);
amp53 = size(data_ae((data_ae(data_ae(:,3)>=52.5 & data_ae(:,3)<53.5)),:));
amp_53=amp53(1,1);
amp54 = size(data_ae((data_ae(data_ae(:,3)>=53.5 & data_ae(:,3)<54.5)),:));
amp_54=amp54(1,1);
amp55 = size(data_ae((data_ae(data_ae(:,3)>=54.5 & data_ae(:,3)<55.5)),:));
```

```
amp_55=amp55(1,1);
amp56 = size(data_ae((data_ae(data_ae(:,3)>=55.5 & data_ae(:,3)<56.5)),:));
amp_56=amp56(1,1);
amp57 = size(data_ae((data_ae(data_ae(:,3)>=56.5 & data_ae(:,3)<57.5)),:));
amp_57=amp57(1,1);
amp58 = size(data_ae((data_ae(data_ae(:,3)>=57.5 & data_ae(:,3)<58.5)),:));
amp_58=amp58(1,1);
amp59 = size(data_ae((data_ae(data_ae(:,3)>=58.5 & data_ae(:,3)<59.5)),:));
amp_59=amp59(1,1);
amp60 = size(data_ae((data_ae(data_ae(:,3)>=59.5 & data_ae(:,3)<60.5)),:));
amp_60=amp60(1,1);
amp61 = size(data_ae((data_ae(data_ae(:,3)>=60.5 & data_ae(:,3)<61.5)),:));
amp_61=amp61(1,1);
amp62 = size(data_ae((data_ae(data_ae(:,3)>=61.5 & data_ae(:,3)<62.5)),:));
amp_62=amp62(1,1);
amp63 = size(data_ae((data_ae(data_ae(:,3)>=62.5 & data_ae(:,3)<63.5)),:));
amp_63=amp63(1,1);
amp64 = size(data_ae((data_ae(data_ae(:,3)>=63.5 & data_ae(:,3)<64.5)),:));
amp_64=amp64(1,1);
amp65 = size(data_ae((data_ae(data_ae(:,3)>=64.5 & data_ae(:,3)<65.5)),:));
amp_65=amp65(1,1);
amp66 = size(data_ae((data_ae(data_ae(:,3)>=65.5 & data_ae(:,3)<66.5)),:));
amp_66=amp66(1,1);
amp67 = size(data_ae((data_ae(data_ae(:,3)>=66.5 & data_ae(:,3)<67.5)),:));
amp_67=amp67(1,1);
amp68 = size(data_ae((data_ae(data_ae(:,3)>=67.5 & data_ae(:,3)<68.5)),:));
amp_68=amp68(1,1);
amp69 = size(data_ae((data_ae(data_ae(:,3)>=68.5 & data_ae(:,3)<69.5)),:));
amp_69=amp69(1,1);
amp70 = size(data_ae((data_ae(data_ae(:,3)>=69.5 & data_ae(:,3)<70.5)),:));
amp_70=amp70(1,1);
amp71 = size(data_ae((data_ae(data_ae(:,3)>=70.5 & data_ae(:,3)<71.5)),:));
amp_71=amp71(1,1);
amp72 = size(data_ae((data_ae(data_ae(:,3)>=71.5 & data_ae(:,3)<72.5)),:));
amp_72=amp72(1,1);
amp73 = size(data_ae((data_ae(data_ae(:,3)>=72.5 & data_ae(:,3)<73.5)),:));
amp_73=amp73(1,1);
amp74 = size(data_ae((data_ae(data_ae(:,3)>=73.5 & data_ae(:,3)<74.5)),:));
amp_74=amp74(1,1);
amp75 = size(data_ae((data_ae(data_ae(:,3)>=74.5 & data_ae(:,3)<75.5)),:));
amp_75=amp75(1,1);
amp76 = size(data_ae((data_ae(data_ae(:,3)>=75.5 & data_ae(:,3)<76.5)),:));
amp_76=amp76(1,1);
amp77 = size(data_ae((data_ae(data_ae(:,3)>=76.5 & data_ae(:,3)<77.5)),:));
amp_77=amp77(1,1);
amp78 = size(data_ae((data_ae(data_ae(:,3)>=77.5 & data_ae(:,3)<78.5)),:));
```

```
amp_78=amp78(1,1);
amp79 = size(data_ae((data_ae(data_ae(:,3)>=78.5 & data_ae(:,3)<79.5)),:));
amp_79=amp79(1,1);
amp80 = size(data_ae((data_ae(data_ae(:,3)>=79.5 & data_ae(:,3)<80.5)),:));
amp_80=amp80(1,1);
amp81 = size(data_ae((data_ae(data_ae(:,3)>=80.5 & data_ae(:,3)<81.5)),:));
amp_81=amp81(1,1);
amp82 = size(data_ae((data_ae(data_ae(:,3)>=81.5 & data_ae(:,3)<82.5)),:));
amp_82=amp82(1,1);
amp83 = size(data_ae((data_ae(data_ae(:,3)>=82.5 & data_ae(:,3)<83.5)),:));
amp_83=amp83(1,1);
amp84 = size(data_ae((data_ae(data_ae(:,3)>=83.5 & data_ae(:,3)<84.5)),:));
amp_84=amp84(1,1);
amp85 = size(data_ae((data_ae(data_ae(:,3)>=84.5 & data_ae(:,3)<85.5)),:));
amp_85=amp85(1,1);
amp86 = size(data_ae((data_ae(data_ae(:,3)>=85.5 & data_ae(:,3)<86.5)),:));
amp_86=amp86(1,1);
amp87 = size(data_ae((data_ae(data_ae(:,3)>=86.5 & data_ae(:,3)<87.5)),:));
amp_87=amp87(1,1);
amp88 = size(data_ae((data_ae(data_ae(:,3)>=87.5 & data_ae(:,3)<88.5)),:));
amp_88=amp88(1,1);
amp89 = size(data_ae((data_ae(data_ae(:,3)>=88.5 & data_ae(:,3)<89.5)),:));
amp_89=amp89(1,1);
amp90 = size(data_ae((data_ae(data_ae(:,3)>=89.5 & data_ae(:,3)<90.5)),:));
amp_90=amp90(1,1);
amp91 = size(data_ae((data_ae(data_ae(:,3)>=90.5 & data_ae(:,3)<91.5)),:));
amp_91=amp91(1,1);
amp92 = size(data_ae((data_ae(data_ae(:,3)>=91.5 & data_ae(:,3)<92.5)),:));
amp_92=amp92(1,1);
amp93 = size(data_ae((data_ae(data_ae(:,3)>=92.5 & data_ae(:,3)<93.5)),:));
amp_93=amp93(1,1);
amp94 = size(data_ae((data_ae(data_ae(:,3)>=93.5 & data_ae(:,3)<94.5)),:));
amp_94=amp94(1,1);
amp95 = size(data_ae((data_ae(data_ae(:,3)>=94.5 & data_ae(:,3)<95.5)),:));
amp_95=amp95(1,1);
amp96 = size(data_ae((data_ae(data_ae(:,3)>=95.5 & data_ae(:,3)<96.5)),:));
amp_96=amp96(1,1);
amp97 = size(data_ae((data_ae(data_ae(:,3)>=96.5 & data_ae(:,3)<97.5)),:));
amp_97=amp97(1,1);
amp98 = size(data_ae((data_ae(data_ae(:,3)>=97.5 & data_ae(:,3)<98.5)),:));
amp_98=amp98(1,1);
amp99 = size(data_ae((data_ae(data_ae(:,3)>=98.5 & data_ae(:,3)<99.5)),:));
amp_99=amp99(1,1);
amp100 = size(data_ae((data_ae(data_ae(:,3)>=99.5 & data_ae(:,3)<=100)),:));
amp_100=amp100(1,1);
```

```
s=[amp_45,amp_46,amp_47,amp_48,amp_49,amp_50,amp_51,amp_52,amp_53,amp_54,amp_55,amp_56,amp_57,amp_58,amp_59,amp_60,amp_61,amp_62,amp_63,amp_64,amp_65,amp_66,amp_67,amp_68,amp_69,amp_70,amp_71,amp_72,amp_73,amp_74,amp_75,amp_76,amp_77,amp_78,amp_79,amp_80,amp_81,amp_82,amp_83,amp_84,amp_85,amp_86,amp_87,amp_88,amp_89,amp_90,amp_91,amp_92,amp_93,amp_94,amp_95,amp_96,amp_97,amp_98,amp_99,amp_100];
n=[45,46,47,48,49,50,51,52,53,54,55,56,57,58,59,60,61,62,63,64,65,66,67,68,69,70,71,72,73,74,75,76,77,78,79,80,81,82,83,84,85,86,87,88,89,90,91,92,93,94,95,96,97,98,99,100];
amp=data_ae(:,3);
figure(12)
plot(tmark,b_value,'k')
xlabel('Time(sec)')
ylabel('B-Value')

title('B-Value vs. Time')

figure(13)
semilogy(n,s,'.')
s(s==0) = 1e-15;
shat = log(s);
A = [ones(length(s),1) n'];
X = inv(A'*A)*A'*shat';
hold on
nn = [n(1):(n(end)-n(1))/200:n(end)];
ss = exp(X(1)+nn*X(2));
semilogy(nn,ss,'k');
% xlabel('Amplitude')
% ylabel('B-Value')
```

A13. CLIP GAGE READING PLOT

```
%Clip gage reading.m
close all
clear all
syms x
w = 241.3;
t = 12.7;
Pmax = 65000;
E=200000000000;
%a=82.55;%final crack length =82.55+63.476=146.026
a=solve(81.2363-w*(1.001-4.6695*x+18.44*x^2-236.82*x^3+1214.9*x^4-
2143.6*x^5),x);
ii=0;
c(5)=0;
for i=1:5;
    if imag(a(i)) == '0.0'
        imag(a(i))
        ii=ii+1
        c(ii) = a(i)
    else

    end
end

dx1=a(1);
d1=(1/dx1-1)^2*Pmax/(E*t*10^-6);

solve(81.2364-w*(1.001-4.6695*x+18.46*x^2-236.82*x^3+1214.9*x^4-
2143.6*x^5),real (x))
dx2=0.15895707329469231379047052677717;
d2=(1/dx2-1)^2*Pmax/(E*t*10^-6);
del_d=d2-d1;
del_d
%Check
%dxc={(E*d1*t/Pmax)^0.5+1}^(-1);
%a1= w*(1.001-4.6695*dxc+18.64*dxc^2-236.82*dxc^3+1214.9*dxc^4-2143.6*dxc^5);

%%
close all
clear all
format long
w = 241.3;
t = 12.7;
Pmax = 65000;
E=200000000000;
```

```
d=0.7164;
ux=1/((E*t*d*10^-6/Pmax)^0.5+1);
a=w*(1.001-4.6695*ux+18.46*ux^2-236.82*ux^3+1214.9*ux^4-2143.6*ux^5);
%80.13884
ux,a
E2=ux;
a1=241.3*(1.001-4.6695*E2+18.46*E2^2-236.82*E2^3+1214.9*E2^4-2143.6*E2^5);
E2, a1
%%
clear all
x=0:100:22800;
%y=10^(-23).*x.^6-6*10^(-19).*x.^5+10^(-14).*x.^4-2*10^(-10).*x.^3+8*10^(-
7).*x.^2+0.0005.*x+80.735;
y=1*10^(-23).*x.^6-6*10^(-19).*x.^5+1*10^(-14).*x.^4-2*10^(-10).*x.^3+8*10^(-
07).*x.^2 + 0.0005.*x + 80.735;
plot(x,y)
```

A14. CLIP GAGE READING

```
%CLIPG.m

close all
clear all
syms x
format long
cd('C:\Users\Saima\Dropbox\Mathlab code\Mozahid_Source mechanisms');
A=xlsread('CLIPGAGE.xls');
w = 241.3;
t = 12.7;
Pmax = 65000;
E=200000000000;
%a=82.55;%final crack length =82.55+63.476=146.026
for k=1:109;
A(k,5);A(k+1,5);
   a=solve(A(k,5)-w*(1.001-4.6695*x+18.46*x^2-236.82*x^3+1214.9*x^4-
2143.6*x^5),x);
ii=0;
c(5)=0;
 for i=1:5;
    if imag(a(i)) == '0.0';
        imag(a(i));
        ii=ii+1;
        c(ii)= a(i);
    else

    end
end
dx1=max(c,[],2);
d1=(1/dx1-1)^2*Pmax/(E*t*10^-6);
dx1; d1;

b=solve(A(k+1,5)-w*(1.001-4.6695*x+18.46*x^2-236.82*x^3+1214.9*x^4-
2143.6*x^5),x);
jj=0;
e(5)=0;
for j=1:5;
    if imag(a(j)) == '0.0';
        imag(a(j));
        jj=jj+1;
        e(jj)= b(j);
    else

    end
```

```
end
dx2=max(e,[],2);
d2=(1/dx2-1)^2*Pmax/(E*t*10^-6);
sen(k+1)=0.5*(d2-d1)/(A(k+1,1)-A(k,1));
dx2; d2; sen;
end

figure
plot(A(:,5),sen)
title ('Clip gage sensitivity','FontSize',12)
ylabel('Opening, mm/cycle','FontSize',12)
xlabel('Crack length, mm','FontSize',12)
```

A15. CRACK GROWTH RATE

```
%CLIPG_txt.m

close all
clear all
cd('C:\Users\Saima\Dropbox\Mathlab code');
A=textread('CLIP.txt');
w = 241.3;
t = 12.7;
Pmax = 65000;
E=200000000000;
%a=82.55;%final crack length =82.55+63.476=146.026
figure
%plot(A(:,5),A(:,4))
title ('Clip gage sensitivity','FontSize',12)
ylabel('Opening, mm/cycle','FontSize',12)
xlabel('Crack length, mm','FontSize',12)
```

A16. MOMENT TENSOR ANLYSIS

```
% Moment Tensor Anlysis
clear all;

cd('C:\Users\User\Dropbox\SM1-POD');
a=xlsread('Source mechanisms and POD.xlsx','Moment tensor');
Cs=-25; % sensor semsitivity -25 for WDI

nr = size(a,2);

tr = [];
for i=9:65

Rf1=-.71791;Rf2=-.71791;Rf3=-.71791;Rf4=-.71791;Rf5=-.71791;
Rf6=-.9864;

 A=
[a(i,24)*a(i,24),2*a(i,24)*a(i,25),2*a(i,24)*a(i,26),a(i,25)*a(i,25),2*a(i,25)*a(i,26),a(i,26
)*a(i,26);

a(i,28)*a(i,28),2*a(i,28)*a(i,29),2*a(i,28)*a(i,30),a(i,29)*a(i,29),2*a(i,29)*a(i,30),a(i,30)
*a(i,30);

a(i,32)*a(i,32),2*a(i,32)*a(i,33),2*a(i,32)*a(i,34),a(i,33)*a(i,33),2*a(i,33)*a(i,34),a(i,34)
*a(i,34);

a(i,36)*a(i,36),2*a(i,36)*a(i,37),2*a(i,36)*a(i,38),a(i,37)*a(i,37),2*a(i,37)*a(i,38),a(i,38)
*a(i,38);

a(i,40)*a(i,40),2*a(i,40)*a(i,41),2*a(i,40)*a(i,42),a(i,41)*a(i,41),2*a(i,41)*a(i,42),a(i,42)
*a(i,42);

a(i,44)*a(i,44),2*a(i,44)*a(i,46),2*a(i,44)*a(i,46),a(i,46)*a(i,46),2*a(i,46)*a(i,46),a(i,46)
*a(i,46)];


B=[a(i,3)*a(i,27)/(Cs*Rf1);a(i,6)*a(i,31)/(Cs*Rf2);a(i,9)*a(i,35)/(Cs*Rf3);a(i,12)*a(i,39)
/(Cs*Rf4);
       a(i,15)*a(i,43)/(Cs*Rf5);a(i,18)*a(i,47)/(Cs*Rf6)];

m=(A\B)*0.0254*10^-3;
       Mt=[m(1,1),m(2,1),m(3,1);m(2,1),m(4,1),m(5,1);m(3,1),m(5,1),m(6,1)];

   [v,e]=eig(Mt);
```

```
    AA=[1,1,1;0,-.5,1;-1,-.5,1];

    en=sort(diag(e/norm(e)),'descend');
    '***Moment tensor***', Mt,'Eigen value',en,'Eigen vector',v
    sprintf( 'Shear, X(percentage) = %.2f "****** compensated linear vector dipole,CLVD (percentage) = %.2f "*****Mean(Percentage) = %.2f ' ,100*inv(AA)*en)
    X= 100*inv(AA)*en;
    if X(1,1)<40
        fprintf('Line: %i: Type of crack:*****Tensile Crack*****\n',i);
        tr = [tr; [a(i,2) 1]];
    else
         fprintf('Line: %i: Type of crack:*****shear Crack*****\n',i)
        tr = [tr; [a(i,2) 2]];
    end
end

**************************************************************************
```